Integrated multi-scale method to predict cross-ventilation effects on inhalation exposure risk through NWP?CFD and network modeling

アリシア マリア ムルガ アキノ

出版情報：Kyushu University, 2018, 博士（工学），課程博士
バージョン：
権利関係：

Integrated multi-scale method to predict cross-ventilation effects on inhalation exposure risk through NWP–CFD and network modeling

Alicia María Murga Aquino

A thesis for the degree of

Doctor of Engineering

Department of Energy and Environmental Engineering

Interdisciplinary Graduate School of Engineering Sciences

Kyushu University

Japan

August 2018

THESIS SUMMARY

Air pollution, frequently typified by $PM_{2.5}$ particulate matter, generates many issues on various exposure levels. A most crucial level is human airways exposure through human breathing because particles and gases absorbed have serious health effects. Therefore, development of accurate prediction technology and exposure countermeasures is required.

Air pollutants are cross-border issues because they include transport mechanisms on global, urban, indoor and even smaller scales. This can be exemplified by local outdoor sources such as diesel cars or indoor gas stoves. Thus, this complex air pollution ranges from a global climate scale (from several thousand, to hundred, to several tens of kilometers), to a city-urban, to a building scale (of up to some meters). Even smaller, complex scales like the human body and human cell scales (~micro meters) need to be considered due to the transport of various environmental conditions and pollutants.

Since these widespread environmental scales are continuous air–carriers, an aerial viewpoint analysis, which can be potentially performed by numerical modeling, is required to continuously integrate and analyze all multi-levels – multi-scales – of environmental scales for a precise health impact prediction in terms of indoor air quality and inhalation exposure risk. Moreover, considering that residents spend approximately 80% of the day in an architectural space such as an office or home – particularly white collars and industrial workers –, it is logical to assume exposure to pollutants also occurs in the indoor environment when discussing air pollution effects on the human respiratory tract.

In this regard, the development of a model that precisely predicts and evaluates indoor air quality based on introduced outdoor flow field through natural ventilation – cross-ventilation – even when dealing with multi-scale environmental factors becomes crucial. Additionally, non-uniform flow and contaminant concentration fields are formed around the human body, product of ventilation type, building design, and meteorological and urban-built factors.

Hence, in order to accurately predict the concentration of pollutants breathed by the human body, various physiological and numerical mechanisms need to be added – such as a human body geometry model – to reproduce and rationally model the interaction of these multi-scale environments. Based on this scenario, this research aims to the develop a wide environmental analysis from the global scale to the mucosal epithelial cell scale on the human respiratory system through a numerical analysis method that continuously analyzes air pollutant transport. This method can potentially be used in cases where field measurement data is limited and within regions where weather data is scarce, making it a cost-effective option.

From the global scale point of view, global climate has been analyzed through numerical weather prediction (NWP). Subsequently, computational fluid dynamics (CFD) and multizone network modeling (MNM) have been used to analyze the urban-built environment scale. Both of these scales are considered responsible of pollutant transport through the wind environment. This research has focused on high-precision prediction of human airways exposure to air pollutants through numerical modeling and geometries that reproduce the human body and respiratory tract to construct an accurate simulation model of inhalation exposure risk.

The main objective of this research is to analyze how global climate and urban-built scale flow field affect the transport of air flow and pollutants to the indoor environment in order to analyze indoor air quality and inhalation exposure risk through three approaches:

i) NWP–CFD steady-state dynamic downscaling approach, ii) full NWP–CFD transient and iii) hybrid CFD–NWP–MNM transient approach.

This paper consists of six chapters, summarized below.

Chapter 1 prepares an extensive literature review in order to construct the principles, basis and objective of the integrated analysis. Specifically, previous research of global scale environment, air flow transport through building openings in cases of cross-ventilation (windows surfaces) set as boundary surfaces for outdoor-indoor analysis, wind pressure coefficient and other aspects have been discussed.

Chapter 2 outlines the background and principle of numerical modeling of global scale through NWP. The principles of detailed city, urban-built, building-indoor and human body scale analysis conducted through CFD are hereby explained. To diminish computational time and resources, average airflow and contaminant have been modeled through MNM, also explained in this chapter.

Chapter 3 discusses the steady-state NWP–CFD dynamic downscaling approach at four different times of the day. Methodology of quasi-coupling between the global and city is explained as well as air flow transport from the outdoor to the indoor environment by way of wind pressure coefficient concept. Pollutant transport from the indoor to the human body, respiratory tract and epithelial concentration through a one-way coupling is also defined. The human body model – computer simulated person, CSP – is also outlined.

Chapter 4 describes the full NWP–CFD transient approach. Analysis from the global scale to the human body scale in terms of time-dependent pollutant transport is explained. Wind pressure coefficient at the wall surfaces of the building has been predicted to transport urban-built scale factors to the indoor environment for a coupling that diminished computational load. Additionally, an integration of the human model to the indoor building environment has been performed and results of spatial mean contaminant concentration and inhalation exposure risk, which vary greatly, are presented.

Chapter 5 summarizes the hybrid CFD–NWP–MNM transient approach. Using wind pressure coefficient coupling, flow and contaminant field analysis below the building scale has been conducted using MNM instead of CFD to lower computational resources. Accuracy of flow and contaminant concentration field at certain zones – spaces – of the building is discussed as well as the merits and demerits of MNM for long-term analysis over restricted spatial resolution.

Finally, Chapter 6 summarizes the methods, results and conclusions yielded by the present study. It also provides recommendations for future work.

ACKNOWLEDGEMENTS

The present research, completed in 3 years at the Interdisciplinary Graduate School of Engineering Sciences, Kyushu University, would not have been possible without the assistance of many important people, to whom I wish to convey my sincere esteem and recognition.

First and foremost, I would like to express my deepest gratitude to my supervisor Professor Kazuhide Ito for his continuous support during my research with patience, enthusiasm and immense knowledge. Because of his guidance and encouragement I could not have asked for a better mentor.

I also would like to thank the rest of the committee members: Professor Aya Hagishima and Professor Yuji Sugihara for their encouragement and insightful comments, which have enriched my research and experience. I want to extend my most sincere thank you to Dr. Sung-Jun Yoo for his help and advice during this investigation. His deep understanding of Computational Fluid Dynamics has provided fruitful discussions.

I would also like to state my appreciation for my colleague Mr. Yusuke Sano for his accurate contributions to this research and also my appreciation for all former and current members of Ito Laboratory in the department of Energy and Environmental Engineering, IGSES, Kyushu University, especially Dr. Nguyen Lu Phuong, Dr. Juyeon Chung and Mr. Ji-Woong Kim with whom I share many memories of these past years.

I dedicate my thesis to my beloved parents and brother, light of my life and reason for my self-improvement. They have supported me throughout my life with love and wisdom. I also thank my friends from all over the world for making my life a happier occurrence. Above all, I humbly thank God for all the opportunities given and achievements accomplished.

CONTENTS

CHAPTER 1: INTRODUCTION

1.1 BACKGROUND 1

1.2 INNOVATION TO PREVIOUS RESEARCH 5

1.3 OBJECTIVES 6

References 7

CHAPTER 2: NUMERICAL MODELING METHODS

2.1 FOREWORD 11

2.2 SCALES OF MOTION AND DOMAINS 12

2.3 DISTINCTION BETWEEN NWP AND CFD 13

2.4 NUMERICAL WEATHER PREDICTION (NWP) 14

2.4.1 Vertical Coordinate and Variables 14

2.4.2 Governing Equations 15

2.4.3 Model Discretization 16

2.5 COMPUTATIONAL FLUID DYNAMICS (CFD) 18

2.5.1 Basic Equations of Fluid Flow 18

2.5.2 Averaging the Equation System 19

2.5.3 Model Discretization 20

2.5.4 Turbulence Models 21

2.5.5 Radiation Model 24

2.5.6 Passive Scalar Transport 26

2.6 MULTIZONE NETWORK MODELLING (MNM) 27

2.6.1 Airflow Analysis..27

2.6.2 Contaminant Analysis..30

CHAPTER 3: NWP-CFD DYNAMIC DOWNSCALING STEADY-STATE APPROACH

3.1 FOREWORD..35

3.2 METHODOLOGY OF DYNAMIC DOWNSCALING 36

3.2.1 NWP Dynamic Downscaling..38

3.2.2 NWP–CFD Quasi-Coupling..41

3.2.3 CFD Dynamic Downscaling..46

3.3 RESULTS AND DISCUSSION..63

3.3.1 NWP Dynamic Downscaling Results..63

3.3.2 CFD Dynamic Downscaling Results..64

3.4 CONCLUSION 72

References 73

CHAPTER 4: FULL NWP-CFD TRANSIENT APPROACH

4.1 FOREWORD..81

4.2 METHODOLOGY OF FULL NWP-CFD TRANSIENT APPROACH 82

4.2.1 NWP Dynamic Downscaling..83

4.2.2 NWP–CFD Data Treatment..85

4.2.3 Variability analysis of diurnal wind pressure coefficient (steady-state) 87

4.2.4 Transient indoor air quality analysis 91

4.3 RESULTS AND DISCUSSION..95

4.3.1 NWP Dynamic Downscaling Results 96
4.3.2 Wind pressure coefficient variability results 97
4.3.3 Transient indoor air quality results 101
4.4 CONCLUSION 103
References 104
CHAPTER 5: HYBRID NWP-CFD-MNM TRANSIENT APPROACH
5.1 FOREWORD 107
5.2 METHODOLOGY OF HYBRID NWP–CFD–MNM TRANSIENT APPROACH 108
5.2.1 NWP Dynamic Downscaling 109
5.2.2 NWP–CFD Data Treatment 111
5.2.3 Variability analysis of diurnal wind pressure coefficient (steady-state) 113
5.2.4 Transient indoor air quality analysis through multizone network modeling 116
5.3 RESULTS AND DISCUSSION 124
5.3.1 NWP Dynamic Downscaling Results 124
5.3.2 Wind pressure coefficient variability results 125
5.3.3 Transient indoor air quality results through MNM 128
5.4 CONCLUSION 132
References 133
CHAPTER 6: SUMMARY AND FUTURE WORK
6.1 SUMMARY 137
6.2 FUTURE WORK 141
SUPPLEMENTAL INFORMATION 143

CHAPTER 1

INTRODUCTION

1.1 BACKGROUND

Annually, global air pollution is responsible for 7 million deaths, according to the latest report of the world health organization (WHO), being above physical inactivity and alcohol abuse. Air pollution also affects people's health, causing respiratory infections, chronic respiratory diseases and even cancer due to breathing[1-1~1-2].

Although usually $PM_{2.5}$ particulate matter and ozone levels, primarily outdoor issues, are typically the focus of research, indoor air pollution has also become crucial for health assessment and improvement because people spend 80% of the day indoors[1-3~1-5]. From this point of view, air pollution becomes a cross-border issue because it includes transport mechanisms on geographic regions of various scales from the global, city urban-built to the indoor microenvironment and even smaller scales.

Therefore, the precise health assessment prediction of determined microenvironments in terms of indoor air quality (IAQ) and inhalation exposure risk becomes an integrated analysis of widespread environmental scales ranging from the global climate, to the city urban-built, to the building scale, to finally the human body environment. IAQ ensures comfortable conditions and health preservation of the micro environment dwellers[1-6~1-7].

Different microenvironments generate different inhalation exposure levels, becoming particularly high in case of industrial activity. Although industrial workers are widely exposed to airborne cumulative pollutants, only a small percentage works under acceptable conditions according to global standard requirements[1-8~1-9]. This results in growing inhalation exposure problems that affect the health and productivity of workers that can be potentially avoidable.

Several indoor air pollutants have been frequently studied due to their high level of impact on human health and carcinogenic aspects[1-10] – e.g. formaldehyde, tobacco smoke, carbon monoxide, radon, particulate matter and others –.

However, in the case of the industrial microenvironment, there are several pollutants in the form of airborne chemicals that have not yet been sufficiently analyzed. For instance, the widely used, acetone, pear-scented chemical cyclohexanone – $(CH_2)_5CO$ – is an effective solvent in cases of manufacturing processes but has presented adverse effects to human health, such as neuro and genotoxicity issues as well as sleep disruption[1-11~1-13].

For an accurate analysis of this specific microenvironment with its particular pollutants, all environmental scales where air flow and contaminant concentration fields are continuously transported need to be analyzed from an aerial viewpoint. This can be performed by numerical modeling. In this regard, the development of a method to evaluate IAQ on a multi-scale level in which air flow is transported from the outdoor to the indoor environment – natural ventilation – becomes crucial.

Furthermore, due to ventilation type, building design, global climate and urban-built factors, non-uniform flow field and contaminant concentration field occur around the human body. Therefore, in order to accurately predict the concentration of pollutants breathed by the human body, several physiological and numerical mechanisms need to be integrated to the analysis, such as a human body model and a human airways model.

Against this background, the purpose of the present research is the development of a multi-scale environmental method from the global climate scale to the mucosal epithelial cell scale on the human respiratory system for an inhalation exposure risk assessment. This is achieved by an integrated numerical modeling method that continuously transfers flow field and pollutant through different scales.

For the global scale analysis, climate has been analyzed through numerical weather prediction (NWP), a particular approach of computational fluid dynamics (CFD) used to determine mesoscale wind flow and geophysical fluctuations in the atmosphere[1-14~1-15].

Subsequently, CFD, used to proficiently analyze building ventilation – natural or mechanical – under micro-scale wind flow, has been applied[1-16]. City urban-built scale flow field has been transferred to the indoor environment – a factory building – by wind-driven cross-ventilation, which greatly influences flow field and pollutant transport due to direct paths interaction. Wind pressure coefficient concept has been applied to relate outdoor-indoor pressure differences.

This ventilation type has been carefully selected because of its popularity in recent years due to its low energy requirements and its minimization of sick building syndrome. Consequently, indoor air flow field, turbulence kinetic energy and specific dissipation rate, temperature and contaminant concentration were transferred to the human body through a computer simulated person (CSP) and human respiratory system in detailed dynamic downscaling.

Albeit a CFD–NWP dynamic downscaling method can be applied for an integrated analysis from a steady-state point of view, it can become computationally heavy when applied to a long-term, occupational exposure analysis. For this reason, multizone network modelling (MNM) has been introduced to analyze average features of flow and contaminant concentration fields below the building scale. This method diminished computational load for long-term exposure cases[1-17~1-19].

This study, therefore, demonstrates a detailed multi-scale environmental method from the global meteorological scale to the human body and human respiratory system scale to analyze air pollutant transport, IAQ and inhalation exposure risk through three approaches:

i) NWP–CFD dynamic downscaling steady-state approach; ii) full NWP–CFD transient approach and iii) hybrid NWP–CFD–MNM transient approach.

Figure 1-1 shows the flow of the present study.

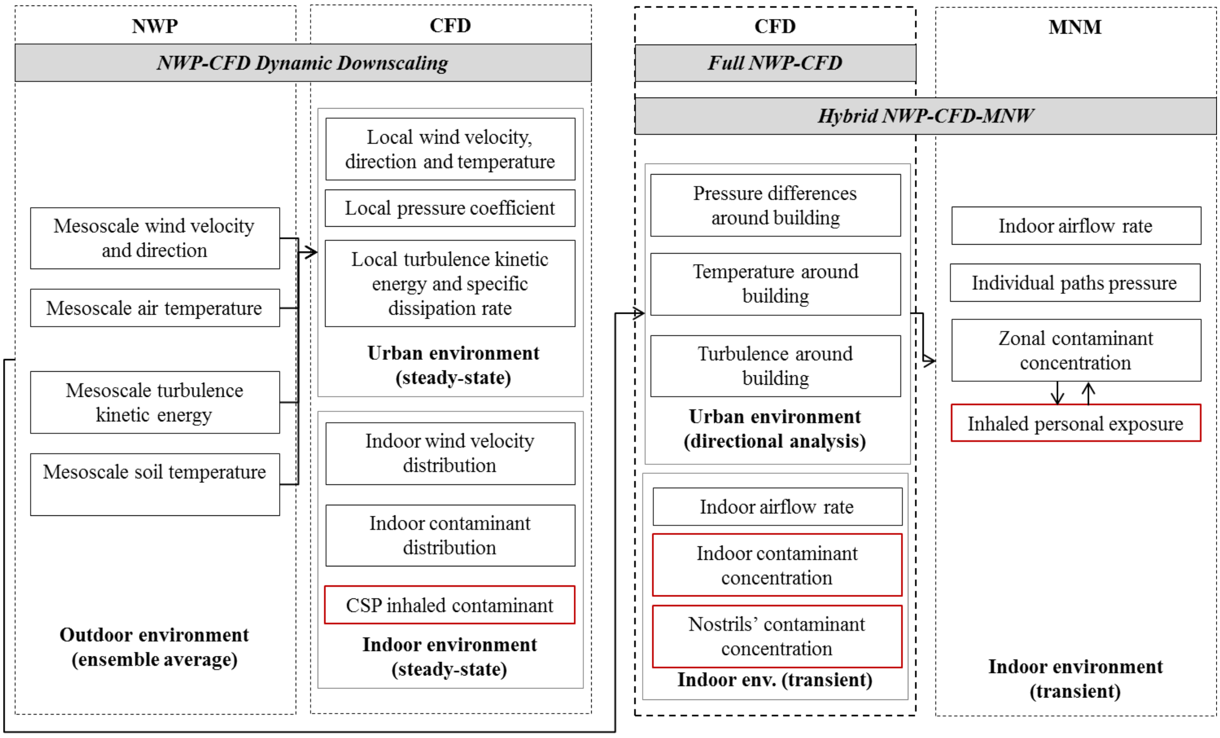

Figure 1-1. Platform schematic of the present study

1.2 INNOVATION TO PREVIOUS RESEARCH

Dynamic downscaling has been historically used to provide regional climate information based on large-scale winds, temperature, water vapor and sea surface temperature from global models[1-20~1-22]. While most research has focused on eco-resources, recent studies have focused on assessing outdoor air quality through regional downscaling, like urban heat island[1-23~1-25].

Several models have overlapped global models analyzed through NWP and microscale models analyzed through CFD using dynamic downscaling techniques. One of these techniques is the use of nested boundary conditions[1-26~1-30]. Although there are several tactics to overcome the gap between NWP and CFD, there is not yet a straightforward procedure. From this point of view, the present research presents an innovative quasi-coupling technique to breach the gap between a mesoscale and a microscale environment while at the same time minimizing computational resources and time.

However, none of the previous research has connected mesoscale models to microscale ones for an IAQ analysis that includes the effects of global and urban climate on the human body and the human respiratory system, as the present research proposes.

Furthermore, by applying the present technique of dynamic downscaling and numerical modeling (NWP and CFD), far-reaching analysis can be performed on regions where measured weather data is unavailable as is the case of this study. In this regard, a comprehensive IAQ and inhalation exposure risk analysis method has been developed under minimum requirements of available weather data and computational resources. In this way, a sustainable cost-effective method for IAQ prediction has been proposed.

1.3 OBJECTIVES

The main objective of this research is to develop an integrated multi-scale environmental method to analyze inhalation exposure risk from the global climate scale to the human body and respiratory system scale. Realistic continuous flow and pollutant transport from the macro to the micro scale have been analyzed by NWP–CFD–MNM numerical modeling. The following specific objectives can also be derived:

(i) Prediction of urban air flow field around a target building through NWP–CFD numerical modeling for areas with limited field measurement data,

(ii) Integration of NWP and CFD to analyze wind pressure coefficient distributions along outside wall surfaces of a building in order to connect the city urban-built environment to the indoor scale in the case of cross-ventilation,

(iii) Prediction of inhalation exposure risk of a worker in a factory at four different times of the day by using a computer simulated person (CSP) and respiratory system model for short-term exposure (steady-state),

(iv) Use of MNM to supply average features of flow field and pollutant transport at building and below-building scale between interconnected zones and the outdoor environment to diminish computational load in long-term exposure,

(v) Application of a full NWP–CFD transient approach based on time-dependent fluctuations of wind pressure coefficient for an accurate transport of city urban-built air flow to the indoor environment for a long-term exposure prediction.

References

1-1) Health Effects Institute, WHO. "State of Global Air 2018." *Special Report.* Boston, MA: Health Effects Institute, 2018.

1-2) IARC (International Agency for Research on Cancer). "Air Pollution and Cancer." *IARC Scientific Publication No. 161.* Lyon, France: World Health Organization, 2013.

1-3) Shaddick, G, Thomas ML, Green A, Brauer M, Donkelaar A, Burnett R, Chang HH, Cohen A, Dingenen RV, Dora C, Gumy S, Liu Y, Martin R, Waller LA, West J, Zidek JV, and Prüss-Ustün, A. "Data integration model for air quality: a hierarchical approach to the global estimation of exposures to ambient air pollution." *J. R. Stat. Soc. C*, vol. 67, pp. 231–253, 2018.

1-4) U.S. EPA (United States Environmental Protection Agency). "Final Report: Integrated Science Assessment (ISA) for Ozone and Related Photochemical Oxidants" *Final Report, Feb. 2013. EPA/600/R-10/076.*Washington, DC: U.S. Environmental Protection Agency, 2013.

1-5) Daniels ME Jr, Donilon TE, Bollyky TJ. "The Emerging Global Health Crisis: Non-communicable Diseases in Low- and Middle-Income Countries." *Independent Task Force Report No. 72.* New York, NY: Council on Foreign Relations, 2014.

1-6) Sundell J. "On the history of indoor air quality and health." *Indoor Air*, vol. 14 Suppl 7, no. Suppl 7, pp. 51–58, 2004.

1-7) Steinemann A, Wargocki P, and Rismanchi B. "Ten questions concerning green buildings and indoor air quality." *Build. Environ.*, vol. 112, pp. 351–358, 2017.

1-8) Pattinson W, Targino AC, Gibson MD, Krecl P, Cipoli Y, and Sá V. "Quantifying variation in occupational air pollution exposure within a small metropolitan region of Brazil." *Atmos. Environ.*, vol. 182, pp. 138–154, 2018.

1-9) Dao A, and Bernstein DI. "Occupational exposure and asthma." *Ann. Allergy, Asthma Immunol.*, 2018 *(In Press).*

1-10) LaDou J. “International occupational health,” *Int. J. Hyg. Environ. Health*, vol. 206, no. 4–5, pp. 303–313, 2003.

1-11) Spiru P, and Simona PL. “A review on interactions between energy performance of the buildings, outdoor air pollution and the indoor air quality.” *Energy Procedia*, vol. 128, pp. 179–186, 2017.

1-12) Gupta PK, Lawrence WH, Turner JE, and Autian J. “Toxicological aspects of cyclohexanone,” *Toxicol. Appl. Pharmacol.*, vol. 49, no. 3, pp. 525–533, 1979.

1-13) Höllbacher E, Ters T, Rieder-Gradinger C, and Srebotnik E. “Emissions of indoor air pollutants from six user scenarios in a model room.” *Atmos. Environ.*, vol. 150, pp. 389–394, 2017.

1-14) Deng X, Stull R. “A mesoscale analysis method for surface potential temperature in mountainous and coastal terrain.” *Mon. Weather Rev*. vol. 133, pp. 389–408, 2005.

1-15) US Department of Energy. “Workshop Report: Research Needs for Wind Resource Characterization.” *NREL/TP-500–43521*, 2008.

1-16) Tham KW. “Indoor air quality and its effects on humans—A review of challenges and developments in the last 30 years.” *Energy Build.*, vol. 130, pp. 637–650, 2016.

1-17) Carpenter SC. “Energy and IAQ impact of CO2-based demand-controlled ventilation.” *ASHRAE Tran*, vol. 102 (2), pp. 80–88, 1996.

1-18) Persily AK, Musser A, Emmerich SJ, and Taylor AW. “Simulations of indoor air quality and ventilation impacts of demand controlled ventilation in commercial and institutional buildings.” *NISTIR 7042*. Gaithersburg: National Institute of Standards and Technology, 2003.

1-19) Ng L, Musser A, Persily A, and Emmerich S. “Indoor air quality analyses of commercial reference buildings.” *Build. Environ*. vol. 58, pp. 179–187, 2012.

1-20) Gustafson WI, and Leung LR. “Regional Downscaling for Air Quality Assessment: A Reasonable Proposition?” *Bulletin of the American Meteorological Society*, vol. 88, pp. 1215–1227, 2007.

1-21) Dickinson RE, Errico RM, Giorgi F, and Bates GT. “A regional climate model for the western United States”. *Climatic Change*, vol. 15, pp. 383–422, 1989.

1-22) Giorgi F, and Mearns LO, 1999 “Introduction to special section: Regional climate modeling revisited” *Geophys. Res*., vol. 104, pp. 6335-6352, 1999.

1-23) Hogrefe C, Lynn B, Civerolo K, Ku JY, Rosenthal J, Rosenzweig C, Goldberg R, Gaffin S, Knowlton K, and Kinney PL. “Simulating changes in regional air pollution over the eastern United States due to changes in global and regional climate and emissions” *Geophys. Res.*, vol. 109, D22301, 2004.

1-24) Steiner AL, Tonse S, Cohen RC, Goldstein AH, and Harley RA. “Influence of future climate and emissions on regional air quality in California” *Geophys. Res.*, vol. 111, D18303, 2006.

1-25) Jiang GF, and Fast JD. “Modeling the effects of VOC and NOX emission sources on ozone formation in Houston during the TexAQS 2000 field campaign”. *Atmos. Environ.*, vol. 38, pp. 5071-5085, 2004.

1-26) Kinbara K, Iizuka S, Kuroki M, Kondo A. “Merging WRF and LES models for the analysis of a wind environment in an urban area.” In: *Proceedings of the Fifth International Symposium on Computational Wind Engineering*. Chapel Hill, NC, May 23–27, 2010.

1-27) Lundquist JK, Mirocha JP, Kosovic B. “Nesting large–eddy simulations within mesoscale simulations in WRF for wind energy applications.” *In: Proceedings of the Fifth International Symposium on Computational Wind Engineering*. Chapel Hill, NC, May 23–27, 2010.

1-28) Ito K. “Integrated numerical approach of computational fluid dynamics and epidemiological model for multi-scale transmission analysis in indoor spaces.” *Indoor Built Environ.*, vol. 23, no. 7, pp. 1029–1049, 2014.

1-29) Murga A, Yoo S-J, Ito K. “Multi stage downscaling procedure to analyse the impact of exposure concentration in a factory on a specific worker through computational fluid dynamics modelling.” *Indoor Built Environ*., vol. 27, no. 4, pp. 486–498, 2018.

1-30) Murga A, Yoo S-J, Ito K. “A multi-scale exposure concentration analysis in a large factory space using a computational fluid dynamics technique”. In: Proceedings of Healthy Buildings America 2015, USA, July 19-22, pp. 543–546, 2015.

[Previously published documents related to this chapter]

[1] Murga A, Yoo S-J, Ito K. “Multi stage downscaling procedure to analyse the impact of exposure concentration in a factory on a specific worker through computational fluid dynamics modelling.” *Indoor Built Environ*., vol. 27, no. 4, pp. 486–498, 2018.

[2] Murga A, Yoo S-J, Ito K. “A multi-scale exposure concentration analysis in a large factory space using a computational fluid dynamics technique”. In: Proceedings of Healthy Buildings America 2015, USA, July 19-22, pp. 543–546, 2015.

NUMERICAL MODELING METHODS

2.1 FOREWORD

This research aims to develop an accurate multi-scale numerical modeling method that transfers air flow and pollutant from the global climate scale to the human body and respiratory system scale. From this viewpoint, each scale must be analyzed through suitable mathematical models to describe the physical properties of each environment. In this study, the following scales and models have been used:

For the global climate scale analysis, four mesoscale domains have been implemented from *NWP1* to *NWP4*. The equations of motion in the atmosphere have been discretized through numerical weather prediction (NWP), although it has been typically used for real-time forecasting purposes. NWP has been applied as part of the dynamic downscaling technique for mesoscale air flow, turbulence and temperature prediction.

For the city urban-built scale, building-indoor environment, human body and respiratory system scale, domains *CFD1* to *CFD4* have been implemented and analyzed through computational fluid dynamics (CFD) to model fluid flow movement.

For the below-building scale, multizone network modeling (MNM) has been applied to domains *MNM1–MNM4* for prediction of average features of flow field and contaminant transport through well-mixing approximation and conjunction points.

Governing equations of momentum, energy and scalar transport of each mathematical model are hereby described.

2.2 SCALES OF MOTION AND DOMAINS

The present study refers to the analysis of mesoscale domains through NWP and microscales through CFD. However, there are several clarifications in regards to the terms used that need to be made to fully understand the scope of the present research.

The term "mesoscale" refers to a broad hierarchy of meteorological divisions that correspond to several spatial/temporal scales. As the properties of atmospheric motions vary across scales, the corresponding computational modeling needs to be properly divided to analyze each of these scales[2-1~2-3]. Figure 2-1 explains the domains and exact spatial scales of atmospheric motion that comprehend the wide term "mesoscale analysis" used in the present study[2-4~2-5]. Domain *NWP1* corresponds to the global-climate scale, domain *NWP2* relates to the level of synoptic scale while domains *NWP3* and *NWP4* conform to a typical mesoscale level.

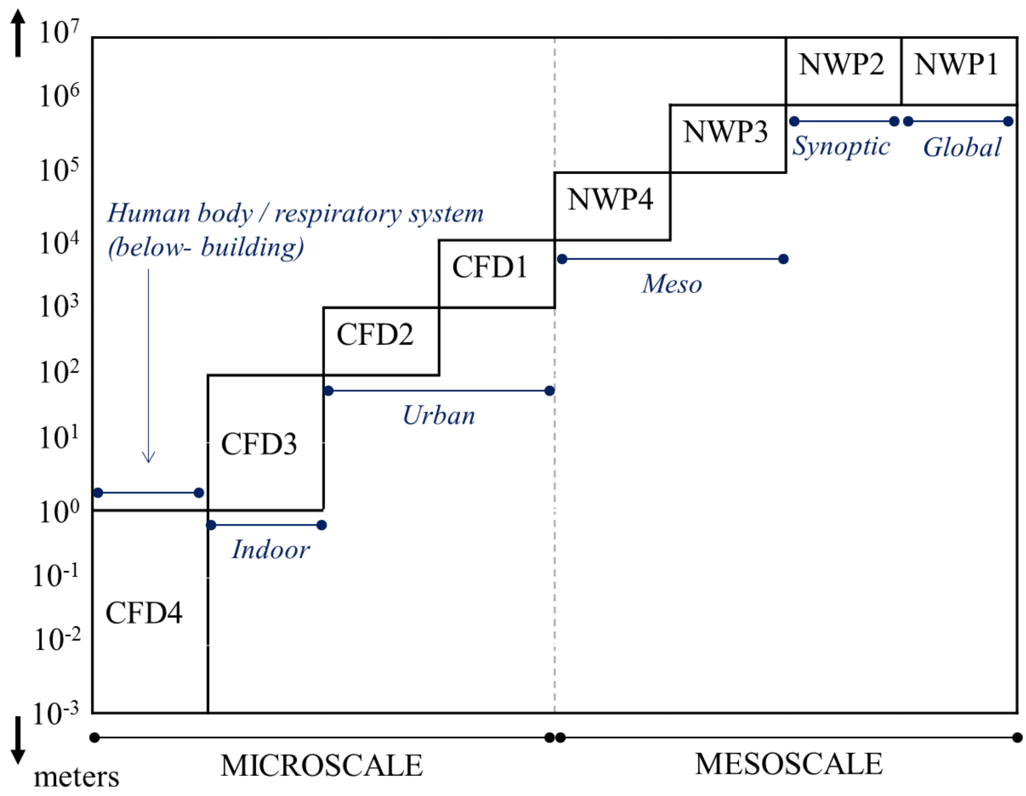

Figure 2-1. Spatial differentiation of mesoscale and microscale analysis used in this study

On the other hand, the term “microscale” used here refers to the smaller scales that have been analyzed below the 10^4 order (as explained in Figure 2-1). Domains *CFD1* and *CFD2* conform the urban micro domains, domain *CFD3* corresponds to the building level and domain *CFD4* analyses the scales below the building level (below-building): the human body and respiratory tract system.

2.3 DISTINCTION BETWEEN NWP AND CFD

Although this study has made the distinction between NWP and CFD, it is important to explain that NWP is a particular form of CFD. NWP specifically studies the motions of the atmosphere as a fluid and therefore uses the equations of fluid dynamics and thermodynamics to predict respective weather results[2-6~2-7]. The present research makes the distinction between NWP, applied to the mesoscale domains and CFD, applied to the microscale domains, based on the above.

2.4 NUMERICAL WEATHER PREDICTION (NWP)

NWP refers to the use of mathematical models of both the atmosphere and oceans to predict weather based on current circumstances. Atmospheric modeling solves the differential equations used to approximate atmospheric flow: continuity equation, conservation of momentum and thermal energy equations. This study uses WRF model version 3.6.1 to analyze domains *NWP1* to *NWP4.*

The weather research and forecasting model (WRF)[2-8] is a system developed by multiple agencies that serves atmospheric research and forecasting purposes. Equation solving follows Ooyama's findings, which use variables that have conservation properties[2-9]. Following Laprise[2-10], equations are formulated using a terrain-following mass vertical coordinate system, further explained in the following sections.

2.4.1 Vertical Coordinate and Variables

η denotes the terrain-following hydrostatic-pressure vertical coordinate explained in equation (2.1):

$$\eta = \frac{\left(p_h - p_{ht}\right)}{\mu} \qquad (2.1)$$

Where $\mu = p_{hs} - p_{ht}$. p_h is the pressure hydrostatic component, and p_{hs} and p_{ht} refer to values along the surface and top boundaries, respectively. This coordinate definition is used in many hydrostatic atmospheric models. η varies from 1 at the surface to 0 at the upper boundary of the domain. This is called a mass vertical coordinate (Figure 2-2).

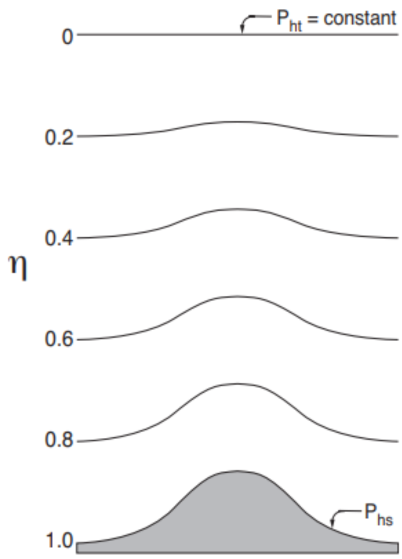

Figure 2-2. Exemplification of the η coordinate

Since $\mu = (x, y)$ is the mass per unit area within the column of the domain at (*x*, *y*), the appropriate flux-form variables are:

$$\mathrm{V} = \mu v = (U, V, W)\,, \qquad \Omega = \mu\dot{\eta}\,, \qquad \Theta = \mu\theta\,, \qquad (2.2)$$

Where $v = (u, v, w)$ are the covariant velocities in the two horizontal and vertical directions, respectively, $\omega = \dot{\eta}$ is the contravariant vertical velocity and θ is the potential temperature. The following non-conserved variables – i.e. not constant – also appear in the governing equations: $\phi = gz$,which represents the geopotential height; p , for pressure; and $\alpha = 1/\rho$, which expresses the inverse density.

2.4.2 Governing Equations

Governing equations of motion for atmospheric applications are numerically integrated in this NWP analysis. The governing Euler equations presented in conservative (flux) form, which are the prognostic equations, are described below[2-11].

$$\partial_t U + (\nabla.Vu) - \partial_x(p\phi_n) + \partial_x(p\phi_x) = \mathrm{F}_u \qquad (2.3)$$

$$\partial_t V + (\nabla.Vv) - \partial_y(p\phi_n) + \partial_y(p\phi_y) = \mathrm{F}_v \qquad (2.4)$$

$$\partial_t W + (\nabla.Vw) - g(\partial_n \text{p} - \mu) = \text{F}_w \quad (2.5)$$

$$\partial_t \Theta + (\nabla.V\theta) = \text{F}_\Theta \quad (2.6)$$

$$\partial_t \phi + (\nabla.V) = 0 \quad (2.7)$$

$$\partial_t \phi - \mu^{-1}\left[(\text{V}.\nabla_\phi) - gW\right] = 0 \quad (2.8)$$

The diagnostic relation for the inverse density is:

$$\partial_n \phi = -\alpha\mu \quad (2.9)$$

An the equation of state is:

$$p = p_0 (R_d \theta / p_0 \alpha)^\gamma \quad (2.10)$$

In the previous equations, *x*, *y* and *n* denote differentiation,

$$\nabla.V_a = \partial_x (U_a) + \partial_y (V_a) + \partial_n (\Omega_a) \quad (2.11)$$

And

$$V.\nabla_a = U\partial_x a + V\partial_x + V\partial_y a + \Omega\partial_n a \quad (2.12)$$

Where *a* is a generic variable, $\gamma = C_p / C_v = 1.4$ is the ratio of the heat capacities for dry air, R_d is the gas constant for dry air and p_0 is a reference pressure of 10^5 Pascals. The terms F_u, F_v, F_w and F_Θ are the forcing terms arising from model physics, turbulent mixing, spherical projections and earth's rotation. The prognostic variables are the velocity components zonal and meridional in Cartesian coordinate, vertical velocity w, perturbation potential temperature, perturbation geo-potential, and perturbation surface pressure of dry air.

2.4.3 Model Discretization

In terms of temporal discretization, the model is integrated using a third-order Runge-Kutta time integration scheme (*RK3*) for a time-split integration[2-12]. Defining the variables as $\phi = (U, V, W, \Theta, \phi', \mu', Q_m)$ with the model equation $\phi_t = R(\phi)$ the solution advances from $\phi(t)$ to $\phi(t + \Delta t)$:

$$\phi^* = \phi^t + \frac{\Delta t}{3} R(\phi^t) \tag{2.13}$$

$$\phi^{**} = \phi^t + \frac{\Delta t}{2} R(\phi^*) \tag{2.14}$$

$$\phi^{t+\Delta t} = \phi^t + \Delta t R(\phi^{**}) \tag{2.15}$$

Where Δt is the model time step and the superscripts denote time levels.

In terms of spatial discretization, a C grid staggering for the variables is used (Figure 2-3). In this situation, normal velocities are staggered one-half grid length from the thermodynamic variables and variables indices $(i, \mathrm{j}, \mathrm{k})$ indicate variable locations $(\mathrm{x}, \mathrm{y}, \eta) = (\mathrm{i}\,\Delta x, \mathrm{i}\,\Delta y, \mathrm{i}\,\Delta\eta)$. Θ is located at mass points and *u*, *v*, and *w* denote *u* points, *v* points and *w* points.

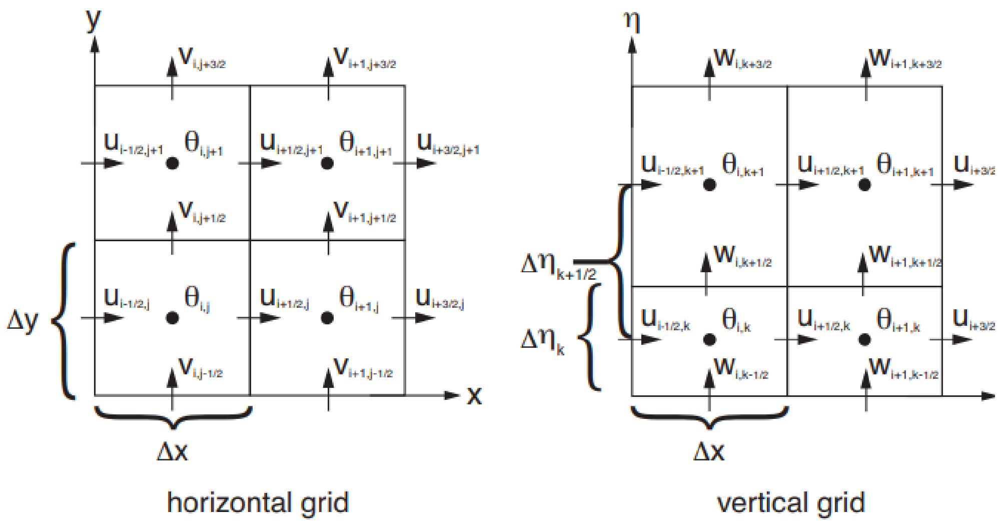

Figure 2-3. Horizontal and vertical grids exemplification

2.5 COMPUTATIONAL FLUID DYNAMICS (CFD)

CFD refers to the use of numerical methods and algorithms to solve fluid flow problems that use partial differential equations of mass, momentum and energy by replacing them for a set of algebraic equations solved by a computer. This research uses ANSYS Fluent to provide comprehensive modeling capabilities for incompressible, compressible, laminar and turbulent flows in a steady-state or transient situation by solving the previously mentioned equations[2-13].

2.5.1 Basic Equations of Fluid Flow

Fluid motion phenomena are defined by the Navier-Stokes equations expressed in (2.16) and (2.17) for incompressible fluids:

$$\frac{\partial U_i}{\partial x_i} = 0 \qquad (2.16)$$

$$\frac{\partial U_i}{\partial t} + U_j . \frac{\partial U_i}{\partial x_j} = -\frac{1}{\rho} . \frac{\partial P}{\partial x_i} + v \frac{\partial}{\partial x_j}\left(\frac{\partial U_i}{\partial x_j} + \frac{\partial U_j}{\partial x_i} \right) - g_i \beta \theta \qquad (2.17)$$

Where U_i represents wind speed (*u*, *v*, *w* components), ρ is the density, v is the kinematic viscosity coefficient, θ is the temperature (or the temperature difference from absolute zero, $\theta - \theta_0$), g_i is the gravity component of the acceleration vector in *i* direction and β is the expansion coefficient.

Equation (2.16) signifies the mass conservation law assuming constant density. Equation (2.17) is the momentum law derived from Newton's second law and explains the effect of buoyancy. In case of non-isothermal flow field, equation (2.17) can by expressed by the thermal energy transport equation (2.18) with respect to the temperature field.

$$\frac{\partial \theta}{\partial t} + \frac{\partial U_j \theta}{\partial x_j} = \frac{\partial}{\partial x_j}\left(\alpha \frac{\partial \theta}{\partial x_j} \right) + S \qquad (2.18)$$

Where α $(=\lambda/C_p{\cdot}\rho)$ is the thermal diffusion coefficient and S is the heat generation term (source term).

Furthermore, similar to equation (2.18), transport phenomena (e.g. moisture and pollutants) can be defined by the scalar transport equation (2.19):

$$\frac{\partial \phi}{\partial t}+\frac{\partial U_j \phi}{\partial x_j}=\frac{\partial}{\partial x_j}\left(D\frac{\partial \phi}{\partial x_j}\right)+S' \qquad (2.19)$$

Where ϕ is the scalar quantity and D is the diffusion coefficient of the target substance. Coupled analysis of equations (2.16) and (2.19) make it possible to grasp scalar transport phenomena of incompressible fluids.

2.5.2 Averaging the Equation System

Equations (2.16) to (2.19) are instantaneous physical quantities and include terms expressed in those instantaneous values. Due to the complexity of this equation system, it is impossible to solve them by direct computation. However, an approximation of temporally and spatially consecutive physical quantities into finite ones for an analytical solution can be achieved by discretization. Nonetheless, it is impossible to suppress the fluctuation of the physical quantity below the difference interval. In this situation, it is necessary to apply a method for an approximate solution.

The ensemble average used to achieve this purpose is expressed in equation (2.20):

$$\overline{f_k(x_i,t)}_E=\lim_{N\to\infty}\left(\frac{1}{N}\sum_{k=1}^{N} f_i(x,t)\right) \qquad (2.20)$$

$$\overline{f(x_i)}_F=\iiint_{\infty}^{\infty}\left(\prod_{i=1}^{3} G\left(x_i-x_i^{'}\right)\right).f\left(x_i^{'}\right)dx_i^{'} \qquad (2.21)$$

Where subscript E represents ensemble average and subscript F represents spatial averaging. In equation (2.21), the one-dimensional filter function $G(x_i)$ is imposed in three dimensions.

In equations (2.16) to (2.19), instantaneous values are separated into averages and fluctuations. After ensemble average application, the previous equations become:

$$\frac{\partial \overline{U_i}}{\partial x_i} = 0 \quad (2.22)$$

$$\frac{\partial \overline{U_i}}{\partial t} + \overline{U_j}.\frac{\partial \overline{U_i}}{\partial x_j} = -\frac{1}{\rho}.\frac{\partial \overline{P}}{\partial x_i} + v\frac{\partial}{\partial x_j}\left(\frac{\partial \overline{U_i}}{\partial x_j} + \frac{\partial \overline{U_j}}{\partial x_i}\right) - \frac{\partial}{\partial x_j}\overline{u_i^{'}u_j^{'}} - g_i\beta\overline{\theta} \quad (2.23)$$

$$\frac{\partial \overline{\theta}}{\partial t} + \frac{\partial \overline{U_j}\overline{\theta}}{\partial x_j} = \frac{\partial}{\partial x_j}\left(\alpha\frac{\partial \overline{\theta}}{\partial x_j}\right) + \frac{\partial}{\partial x_j}\overline{u_j^{'}\theta^{'}} \quad (2.24)$$

Where U_i, P and θ are average values, $u_i^{'}$ and $\theta^{'}$ are variable and the overbar represents ensemble average values. Equation (2.23) is called the Reynolds equation. Furthermore, the term $\overline{u_i^{'}u_j^{'}}$ in equation (2.23) represents the Reynolds stress and the term $\overline{u_j^{'}\theta^{'}}$ in equation (2.24) is the temperature flux. Originally, the definition of Reynolds stress is approximately the product of density ρ and $\overline{u_i^{'}u_j^{'}}$; however, it has been simplified as only $\overline{u_i^{'}u_j^{'}}$.

2.5.3 Model Discretization

The finite volume method (FVM) is one of the most popular discretization methods to represent partial differential equations in their algebraic counterparts[2-14~2-15].

FVM denotes the volume that encloses a node point in a mesh. Volume integrals containing divergence are transformed into surface integrals and then calculated as fluxes at the surfaces of each volume, denoted by the following equation:

$$\int_A \rho\phi\vec{u}\cdot d\vec{A} = \int_A \Gamma_\phi \nabla\phi d\vec{A} + \int_{CV} S_\phi dV \quad (2.25)$$

Where ρ is the airflow density, ϕ represents the discretization of the velocity components, kinetic energy, dissipation rate and fluid enthalpy. $\nabla\phi$ denotes the scalar gradient and Γ_ϕ is the diffusion coefficient. In cases of second order accuracy with the Taylor's expansion approach, the value ϕ_f can be explained by the following equation:

$$\phi_{f,SOU} = \phi + \nabla\phi\times\vec{r} \quad (2.26)$$

Where ϕ and $\nabla\phi$ are the cell-centered value and its gradient and $\vec{r}$ is the displacement vector from the upstream cell centroid to the face.

2.5.4 Turbulence Models

2.5.4.1 Shear stress transport (SST) k-ω model

In terms of turbulence for the CFD analysis of this study, the RANS Shear Stress Transport (SST) *k-ω* model – which is based on the standard *k-ω* model – introduced by Menter has been applied. It has been focused on city urban-built and building-indoor modeling[2-16~2-17], as explained in Figure 2-1. This model combines the k-omega and k-epsilon turbulence models, applying the k-omega to the inner region of the boundary layer and the k-epsilon to the free shear flow through blending functions. It also incorporates a damped cross-diffusion derivative term in the omega equation. Furthermore, the turbulent viscosity modeling constants have been modified.

This model is defined by the following equations:

$$\frac{\partial}{\partial t}(\rho k)+\frac{\partial}{\partial x_i}(\rho k u_i)=\frac{\partial}{\partial x_j}\left(\Gamma_k \frac{\partial k}{\partial x_j}\right)+G_k-Y_k+S_k \tag{2.27}$$

$$\frac{\partial}{\partial t}(\rho \omega)+\frac{\partial}{\partial x_i}(\rho \omega u_i)=\frac{\partial}{\partial x_j}\left(\Gamma_\omega \frac{\partial \omega}{\partial x_j}\right)+G_\omega-Y_\omega+S_\omega \tag{2.28}$$

Where G_k is the generation of turbulence kinetic energy, G_ω is the generation of ω and Γ_k and Γ_ω represent the effective diffusivity k and ω. Y_k and Y_ω represent the dissipation of k and ω due to turbulence, D_ω is the cross-diffusion term and ρ is density. S_k and S_ω are source terms.

Effective diffusivities Γ_k and Γ_ω and turbulent viscosity μ_t are modelled through equations (2.29), (2.30) and (2.31), respectively:

$$\Gamma_k=\mu+\frac{\mu_t}{\sigma_k} \tag{2.29}$$

$$\Gamma_\omega = \mu + \frac{\mu_t}{\sigma_\omega} \tag{2.30}$$

$$\mu_t = \frac{\rho k}{\omega} \frac{1}{\max\left[\frac{1}{\alpha *}, \frac{\Omega F_2}{\alpha_1 \omega}\right]} \tag{2.31}$$

Where

$$\Omega \equiv \sqrt{2\Omega_{ij}\Omega ij} \tag{2.32}$$

$$\sigma_k = \frac{1}{F_1 / \sigma_{k,1} + \left(1 - F_1 / \sigma_{k,2}\right)} \tag{2.33}$$

$$\sigma_\omega = \frac{1}{F_1 / \sigma_{\omega,1} + \left(1 - F_1 / \sigma_{\omega,2}\right)} \tag{2.34}$$

The previously mentioned blending functions are described below:

$$F_1 = \tanh\left(\phi_1^4\right) \tag{2.35}$$

$$\phi_1 = \min\left[\max\left(\frac{\sqrt{k}}{0.09\omega y}, \frac{500\mu}{\rho y^2 \omega}\right), \frac{4\rho k}{\sigma_{\omega_1 2} D_\omega^+ y^2}\right] \tag{2.36}$$

$$D_\omega^+ = \max\left[2\rho \frac{1}{\sigma_{\omega,2}} \frac{1}{\omega} \frac{\partial k}{\partial x_j} \frac{\partial \omega}{\partial x_j}, 10^{-20}\right] \tag{2.37}$$

$$F_2 = \tanh\left(\phi_2^2\right) \tag{2.38}$$

$$\phi_2 = \max\left[2\frac{\sqrt{k}}{0.09\omega y}, \frac{500\mu}{\rho y^2 \omega}\right] \tag{2.39}$$

Where y is distance to surface and D_ω^+ is the positive portion of the cross-diffusion term. Turbulence production is calculated by the expressions (2.40) and (2.41). S is the stress tensor.

$$G_k = \mu_t S^2 \tag{2.40}$$

$$G_w = \frac{\alpha}{v_t} G_k \tag{2.41}$$

Turbulence dissipation of k and ω is represented by equations (2.42) and (2.43):

$$Y_k = \rho \beta^* k \omega \tag{2.42}$$

$$Y_w = \rho \beta \omega^2 \tag{2.43}$$

The SST model includes the term D_ω to blend together the standard *k-ω* and *k-ε* model, which can be described by equation (2.44):

$$D_\omega = 2(1-F_1)\rho\sigma_{\omega,2}\frac{1}{\omega}\frac{\partial k}{\partial x_j}\frac{\partial \omega}{\partial x_j} \tag{2.44}$$

Model constants are presented below:

$\sigma_{k,1} = 1.176$; $\sigma_{\omega,1} = 2.0$; $\sigma_{k,2} = 1.0$; $\sigma_{\omega,2} = 1.168$; $\alpha_1 = 0.31$; $\beta_{i,1} = 0.075$; $\beta_{i,2} = 0.0828$

2.5.4.2 Low Reynolds k-ε model

In general, the standard *k-ε* analyzes turbulence in cases of high Reynolds number; however, in order to solve turbulence for low Reynold number cases, the low Reynolds number type *k-ε* has been developed[2-18]. In this study, this model has been applied in the human body and respiratory tract system domain.

This model includes an attenuation function that takes into consideration the wall coordinate y^+ and the Reynolds number when obtaining the viscosity coefficient V_t and in the region near the wall surface. A non-slip boundary condition is applied after dividing the wall into sufficient meshes. The model functions f_1 and f_2 are introduced in the production and dissipation term of turbulence near wall surface.

The following equations embody the low Reynolds k-ε model:

$$\frac{\partial \overline{U_i}}{\partial t} + \overline{U_j}.\frac{\partial \overline{U_i}}{\partial x_j} = -\frac{1}{\rho}.\frac{\partial \overline{P}}{\partial x_i} + v\frac{\partial}{\partial x_j}\left(\frac{\partial \overline{U_i}}{\partial x_j} + \frac{\partial \overline{U_j}}{\partial x_i}\right) - \frac{\partial}{\partial x_j}\overline{u_i^{'}u_j^{'}} \tag{2.45}$$

$$-\overline{u_i^{'}u_j^{'}} = v_t\left(\frac{\partial \overline{U_i}}{\partial x_j} + \frac{\partial \overline{U_j}}{\partial x_i}\right) - \frac{2}{3}k\delta_{ij} \tag{2.46}$$

$$v_t = C_\mu \cdot f_\mu \cdot \frac{k^2}{\varepsilon} \tag{2.47}$$

$$\frac{\partial k}{\partial t}+\bar{U}_j\frac{\partial k}{\partial x_j}=D_k+P_k-(\bar{\varepsilon}+D) \quad (2.48)$$

$$\frac{\partial\bar{\varepsilon}}{\partial t}+\bar{U}_j\frac{\partial\bar{\varepsilon}}{\partial x_j}=D_\varepsilon+\frac{\bar{\varepsilon}}{k}\cdot(C_{\varepsilon 1}\cdot f_1\cdot P_k-C_{\varepsilon 2}\cdot f_2\cdot\bar{\varepsilon})+E \quad (2.49)$$

$$P_k=-\overline{u_i'u_j'}\cdot\frac{\partial\overline{U_i}}{\partial x_j} \quad (2.50)$$

$$D_k=\frac{\partial}{\partial x_j}\cdot\left(\left(\nu+\frac{\nu_t}{\sigma_k}\right)\frac{\partial k}{\partial x_j}\right) \quad (2.51)$$

$$D_\varepsilon=\frac{\partial}{\partial x_j}\cdot\left(\left(\nu+\frac{\nu_t}{\sigma_\varepsilon}\right)\frac{\partial\bar{\varepsilon}}{\partial x_j}\right) \quad (2.52)$$

$$\bar{\varepsilon}=\varepsilon-2\nu\left(\frac{\partial\sqrt{k}}{\partial x_k}\right)^2 \quad (2.53)$$

Where f_μ and f_1, f_2 represent model functions; D and E have been introduced when $\bar{\varepsilon}$ is used. In the previous equations $f_\mu=f_1=f_2=0; D=E=0$ and $\bar{\varepsilon}=\varepsilon$.

2.5.5 Radiation Model

This study has considered radiation in the heat transfer simulation. The model introduced, surface-to-surface (S2S), accounts for the radiation exchange in an enclosure of gray-diffuse surfaces. In this model, the energy exchange between two surfaces depends in part of their size, separation distance and orientation.

The main assumption of this model is that any absorption, emission or scattering of radiation can be disregarded, therefore, only "surface-to-surface" radiation need to be considered for analysis. It also accounts for the radiation exchange where gray-diffuse surfaces are located, depending on view factors[2-19].

The S2S model uses very low computational resources, making it applicable for building and indoor ventilation analysis[2-20].

The energy flux that leaves a surface k is composed of directly emitted and reflected energy and can be expressed as:

$$q_{out,k} = \varepsilon_k \sigma T_k^4 + \rho_k q_{in,k} \qquad (2.54)$$

Where $q_{out,k}$ is the energy flux leaving the surface, ε_k is the emissivity (in this case equal to the absorptivity, $\varepsilon = \alpha$), σ is the Stefan-Boltzmann constant, ρ_k is the density and $q_{in,k}$ is incident flux on surface k from the surroundings.

Incident energy upon a surface can be described by the view factor F_{jk}, which is the energy leaving surface j and incident on surface k. The incident energy flux $q_{in,k}$ can be expressed as the energy flux leaving surfaces by the following equation:

$$A_k q_{in,k} = \sum_{j=1}^{N} A_j q_{out,j} F_{jk} \qquad (2.55)$$

Where A_k is the area. The view factor reciprocity relationship can be written as:

$$A_j F_{jk} = A_k F_{kj} \, (j = 1, 2, 3, etc.) \qquad (2.56)$$

Finally, the equation can be expressed as:

$$\mathrm{J}_k = E_k + \rho_k \sum_{j=1}^{N} F_{kj} J_j \qquad (2.57)$$

Where J_k is the radiosity (energy given off) and E_k is the emissive power. This equation can be recast into matrix form, with K representing a $N \times M$ matrix, J is the radiosity vector and E is the emissive power vector, as follows:

$$KJ = E \qquad (2.58)$$

The above is the radiosity matrix equation. Surface cluster temperature can be calculated by area averaging by using equation (2.58):

$$T_{SC} = \left(\frac{\sum_f A_f T_f^4}{\sum A_f} \right)^{1/4} \qquad (2.60)$$

Where T_{SC} is the temperature and A_f and A_f are the area and temperature of the face, respectively.

2.5.6 Passive Scalar Transport

In this study, pollutants are assumed to be passive scalars, calculated through the transport equation (2.61) explained below:

$$\frac{\partial \bar{\phi}}{\partial t} + \frac{\partial \overline{U_i} \bar{\phi}}{\partial x_i} = \frac{\partial}{\partial x_i} \left\{ \left(D + \frac{\nu_t}{\mathrm{Pr}} \right) \frac{\partial \bar{\phi}}{\partial x_i} \right\} \tag{2.61}$$

"Passive scalar" is the assumption that the target substance is the same as air (gas phase). That is, the Schmit number (Sc=v/D); where v is molecular diffusion coefficient and D is the diffusion coefficient of the target substance in air) is 1. Assuming the Prandtl number as Pr=1 in the transport equation, the diffusion term can be solved through $v+v_t$ if flow field analysis is performed and concentration distribution can be analyzed based on flow field.

2.6 MULTIZONE NETWORK MODELLING (MNM)

MNM supplies average features of airflow and contaminant transport through interconnected zones in which a building has been divided or in connection with the outdoor environment through pressure differences.

A CFD-only, transient analysis is not practical when analyzing a building with multiple infiltration points because it requires many resources; however, the need for long-term analyses is increasing[2-21~2-22]. From this point of view, this study proposes a coupling between CFD and MNM that analyzes macroscopic behavior of flow and pollutant transport at a below-building scale[2-23]. In this study, below-building scale refers to the separate analysis of multiple zones, in which the building has been divided. CONTAM 3.0 has been used for the MNM analysis.

2.6.1 Airflow Analysis

Airflow calculations in CONTAM follow the algorithms developed by AIRNET[2-24].

The airflow rate from one zone to another F_{ij} is a function of the pressure difference along the flow path $Pj - P_i$ and can be described by the following equation:

$$F_{ij} = f(P_j - P_i) \tag{2.62}$$

The principle of conservation of mass for a transient solution is:

$$\frac{\partial m_i}{\partial t} = \rho_i \frac{\partial V_i}{\partial t} + V_i \frac{\partial \rho_i}{\partial t} = \sum_j F_{ji} + F_i \tag{2.63}$$

$$\frac{\partial m_i}{\partial t} \approx \frac{1}{\Delta t}\left[\left(\frac{P_i V_i}{R T_i}\right)_t - \left(m_i\right)_{t-\Delta t}\right] \tag{2.64}$$

$$\sum_j F_{ji} = 0 \tag{2.65}$$

Where m_i is the mass of air inside a zone and F_i is equal or more than the non-flow processes that could add or remove air from the zone. A non-flow process is a closed system in which mass transfer is not possible.

For non-flow processes, density varies during time steps in transient simulations.

To solve equation (2.65), the Newton-Raphson method that solves this nonlinear problem by iterating the solutions of linear equations can be applied. From this, the vector $\{P\}*$ is calculated by:

$$\{P\}* = \{P\} - \{C\} \qquad (2.66)$$

Where the correction vector $\{C\}$ is obtained from this matrix relationship:

$$[J]\{C\} = \{B\} \qquad (2.67)$$

Where $\{B\}$ is a column vector with the elements given by the following equation:

$$B_i = \sum_j F_{ji} \qquad (2.68)$$

And $[J]$ is the square Jacobian matrix. Its elements are expressed by equation (2.69):

$$J_{ij} = \sum_i \frac{\partial F_{ji}}{\partial P_j} \qquad (2.69)$$

To allow for a faster calculation, the method proposed by Dhatt is applied. This method solves symmetric and asymmetric matrices:

$$|J_{ij}| = \sum_{j+i} |J_{ij}| \qquad (2.70)$$

Global convergence value is computed through the following equation:

$$\gamma = \frac{\sum_i \left|\sum_j F_{ji}\right|}{\sum_i \sum_j |F_{ji}|} \qquad (2.71)$$

A linear approximation relating the flow to the pressure drop that allows for an initial set of zone pressures can be expressed as follows:

$$F_{ji} = c_{ji} + b_{ji}(P_j - P_i) \qquad (2.72)$$

2.6.1.1 Infiltration Airflow

Infiltration is the result of air flowing through openings in the building envelope, large or small, intentional or accidental. Flow within each airflow element is assumed to be governed by Bernoulli's equation:

$$\Delta \mathrm{P} = \left(P_1 + \frac{\rho V_1^2}{2} \right) - \left(P_2 + \frac{\rho V_2^2}{2} \right) + \rho g (z_1 - z_2) \qquad (2.73)$$

Where $\Delta \mathrm{P}$ is the total pressure drop, P_1, P_2, V_1, and V_2 are the entry and exit static pressures and velocities, respectively, ρ is the air density, g is gravitational acceleration and z_1 and z_2 are the entry and exit elevations.

Pressure, temperature and elevation are necessary values to compute airflow. Elevation is important to determine stack effects pressures. Pressures terms can be rearranged and pressure for the building envelope is described by:

$$\Delta \mathrm{P} = \mathrm{P}_j - P_i + P_s + P_w \qquad (2.74)$$

Where $\mathrm{P}_j - P_i$ is the pressure drop between zones, P_s is pressure difference due to density and elevation and P_w is pressure difference due to wind.

2.6.1.2 Power law Flow Infiltration

The following empirical power law equations, based on the relationship between the flow and pressure difference, are applied in most infiltration cases:

$$Q = C(\Delta P)^n \qquad (2.75)$$

$$F = C(\Delta P)^n \qquad (2.76)$$

Where Q is the volumetric flow rate and F is the mass flow rate. A variation of this equation in relation to orifices can be expressed as:

$$Q = C_d A \sqrt{\frac{2\Delta P}{\rho}} \qquad (2.77)$$

Where C_d is the discharge coefficient and A is the area of the orifice. Although the previous equation is used in cases of turbulent flows, laminar ones can be analyzed through the following equation:

$$F = \frac{C_k \rho \Delta P}{\mu} \qquad (2.78)$$

Where C_k is the laminar flow coefficient and μ is the viscosity.

2.6.2 Contaminant Analysis

Contaminant dispersal analysis is based on mass conservation principle in a control volume of air, which can be a room or several coupled zones. Therefore, the mass of air and concentration of contaminant in a control volume can be summarized through equations (2.79) and (2.80):

$$m_i = \sum_\alpha m_i^\alpha \qquad (2.79)$$

$$C_i^\alpha = m_i^\alpha / m_i \qquad (2.80)$$

Contaminant can be added into or removed from a zone through equations (2.81) and (2.82), respectively:

$$\sum_j F_{j\to i}(1-\eta_j^\alpha)C_j^\alpha \qquad (2.81)$$

$$\sum_j F_{j\to i}C_j^\alpha \qquad (2.82)$$

Where $F_{j\to i}$ is the rate of air mass flow and η_j^α is the filter efficiency.

Combining both processes into a single equation for transient analysis in a control volume, the next equation of species mass control can be derived:

$$\rho_i V_i C_i^\alpha \Big|_{t+\Delta t} \approx \rho_i V_i C_i^\alpha \Big|_t + \Delta t \cdot \Big[\sum_j F_{j\to i}(1-\eta_j^\alpha)C_j^\alpha + G_i^\alpha + m_i \sum_\beta k^{\alpha\beta} C_i^\beta - \sum_j F_{i\to j} C_i^\alpha - R_i^\alpha C_i^\alpha \Big]_{t+\delta t}$$
(2.83)

If $\delta t = \Delta t$ is substituted in the above equation, it can be rewritten as:

$$\left[\rho_i V_i + \Delta t \cdot \left(\sum_j F_{i\to j} + R_i^\alpha\right)\right] C_i^\alpha \Big|_{t+\Delta t} \approx \rho_i V_i C_i^\alpha \Big|_t + \Delta t \cdot \left[\sum_j F_{j\to i}(1-\eta_j^\alpha) C_j^\alpha + G_i^\alpha + m_i \sum_\beta k^{\alpha\beta} C_i^\beta\right]_{t+\Delta t}$$

(2.84)

All concentrations C_i^α at time $t+\Delta t$ are functions of various other concentrations, which is known as the standard implicit method and can be suitable for a long time step. In the case of a short time step, the standard explicit method can be applied through equation (2.85)

$$\rho_i V_i C_i^\alpha \Big|_{t+\Delta t} \approx \rho_i V_i C_i^\alpha \Big|_t + \Delta t \cdot \left[\sum_j F_{j\to i}(1-\eta_j^\alpha) C_j^\alpha + G_i^\alpha + m_i \sum_\beta k^{\alpha\beta} C_i^\beta - \sum_j F_{i\to j} C_i^\alpha - R_i^\alpha C_i^\alpha\right]_t$$

(2.85)

Finally, generation and removal coefficients need to be defined. The constant coefficient model uses the following equation with S_α as the contaminant source strength:

$$S_\alpha(t) = G_\alpha - R_\alpha C_\alpha(t) \qquad (2.86)$$

References

2-1) Cullen M. "Modelling atmospheric flows", *Acta Numer.* vol. 16, pp. 67–154, 2007.

2-2) Klein K. "Scale-dependent models for atmospheric flows", *Annu. Rev. Fluid Mech.* vol. 42, pp. 249–274, 2010.

2-3) Smolarkiewicz PK, Szmelter J, and Xiao F. "Simulation of all-scale atmospheric dynamics on unstructured meshes," *J. Comput. Phys.*, vol. 322, pp. 267–287, 2016.

2-4) Orlanski I. "A rational subdivision of scales for atmospheric processes". *Bulletin of the American Meteorological Society*. vol. 56 (5), pp. 527–530, 1975.

2-5) Fujita TT. "Mesoscale classifications: their history and their application to forecasting". *In Ray, P.S. Mesoscale Meteorology and Forecasting*. *Boston: American Meteorological Societ*y. pp. 18–35, 1986.

2-6) Acheson DJ. "Elementary Fluid Dynamics". *Clarendon Press*. ISBN 0-19-859679-0, 1990.

2-7) Batchelor GK. "An Introduction to Fluid Dynamics". *Cambridge University Press*. ISBN 0-521-66396-2, 1967.

2-8) Skamarock WC, Klemp JB, Dudhia J, Gill DO, Barker DM, Huang XY, Wang W, Powers JG. "A Description of the Advanced Research WRF Version 3". *NCAR Technical Notre*, CCAR/TN–475+STR.113, 2008.

2-9) Ooyama KV. "A thermodynamic foundation for modeling the moist atmosphere". *J. Atmos. Sci.*, 47, pp. 2580–2593, 1990.

2-10) Laprise R. "The Euler Equations of motion with hydrostatic pressure as an independent variable". *Mon. Wea. Rev.*, 120, pp. 197–207, 1992.

2-11) Klemp J, Skamarock W, Dudhia J. "Conservative split-explicit time integration methods for the compressible nonhydrostatic equations", *Mon. Weather Rev*, vol. 135 pp. 2897–2913, 2007.

2-12) Wicker LJ, and Skamarock WC. “Time splitting methods for elastic models using forward time schemes”. *Mon. Wea. Rev.*, 130, pp. 2088–2097, 2002.

2-13) ANSYS/Fluent ver. 16.0, User Manual, 2016.

2-14) LeVeque RJ. “Finite‐volume methods for non‐linear elasticity in heterogeneous media”. *Int. J. Numer. Meth. Fluids,* vol. 40, pp. 93–104, 2002.

2-15) Toro EF. Riemann Solvers and Numerical Methods for Fluid Dynamics, Springer, New York , 1999.

2-16) Menter FR. “Zonal Two Equation k-ω Turbulence Models for Aerodynamic Flows”. *AIAA Paper* pp. 93–2906, 1993.

2-17) Menter FR. “Two-Equation Eddy-Viscosity Turbulence Models for Engineering Applications”. *AIAA Journal*, vol. 32, no 8, pp. 1598–1605, 1994.

2-18) Murakami S, Kato S, Chikamoto T, Laurence D, and Blay D. “New Low-Reynolds-Number k-ε model including damping effect due to Buoyancy in a stratified Flow Field”. *Int. J. Heat Mass Transfer*, Vol. 39, No. 16, pp. 3483–3496, 1996.

2-19) Modest MF. “Radiative Heat Transfer”. Series in Mechanical Engineering, McGraw-Hill, 1993.

2-20) Gosselin JR, and Chen QY. “A computational method for calculating heat transfer and airflow through a dual-airflow window.” *Energy and Building.,* vol. 40, pp. 452–458, 2008.

2-21) Chow WK. “Wind-induced indoor-air flow in a high-rise building adjacent to a vertical wall”. *Appl. Energy* 77, pp. 225–234, 2004.

2-22) Asfour OS, and Gadi MB. “A comparison between CFD and network models for predicting wind-driven ventilation in buildings”. *Build. Environ.,* vol. 42 (12) pp. 4079–4085, 2007.

2-23) Schaelin A, Dorer V, van der Maas J, and Moser A. "Improvement of multizone model predictions by detailed flow path values from CFD calculations". *ASHRAE Transactions* 100 (Part 2), pp. 709– 720, 1993.

2-24) Dols WS, and Polidoro BJ. "CONTAM User guide and program documentation Version 3.2". *Technical Notel (NIST TN) –1887*, 1, 2015.

NWP–CFD DYNAMIC DOWNSCALING STEADY-STATE APPROACH

3.1 FOREWORD

This section describes the NWP–CFD dynamic downscaling methodology and its results under steady-state. Eight different-scaled domains (*NWP1~NWP4*, *CFD1~CFD4*) have been connected at their boundaries. The final aim of this steady-state procedure is the analysis of global scale climate and its impact on flow field and contaminant transport into the human body and human respiratory system[3-1~3-6].

This section uses so-called dynamic downscaling technique to connect a mesoscale domain to a microscale one as a way of sustaining solution convergence and saving computational time. In the case of the domains analyzed by NWP (*NWP1~NWP4*), an embedded two-way nesting technique has been applied. This technique allows for feedback between the finer (micro) domain and the coarser (meso) one.

In the case of the domains analyzed by CFD (*CFD1~CFD4*), an independent one-way nesting technique has been used, where smaller domains (finer mesh) run separately to the bigger ones (coarser) (see Figure 2-1 in Chapter 2) and no feedback occurs, diminishing computational load[3-7~3-9].

This technique has been typically used in the city urban-built environment field to introduce global conditions (coarse scales) to local weather analysis (fine scales) but has few applications in the IAQ and inhalation exposure field. Therefore, it presents an opportunity for innovation and an alternative for cases of limited outdoor data[3-10~3-11].

3.2 METHODOLOGY OF DYNAMIC DOWNSCALING

Downscaling is the procedure to take information from large scales to make predictions at local scales, in which the terms "large" and "local" are variable and defined by the user (as Figure 2-1 explains for this particular study).The two types of approaches to downscaling are statistical and dynamic. Statistical downscaling is the development of statistical relationships between climate and variables to model experiments for local simulations.

Dynamic downscaling requires running climate models (or large scale models) on regional sub-domains (or micro scale models) as boundary conditions. This study has used dynamic downscaling to connect large-sized domains to small-sized ones by focusing on the boundary conditions[3-12~3-13]. The dynamic downscaling approach described in this chapter connects eight different-sized scales, hereby denoted as domains.

The first four mesoscale domains have been analyzed through NWP (*NWP1~NWP4*) by way of an embedded two-way nesting technique. Nesting technique in mesoscale modeling allows for an increase in spatial resolution only in the sub-domains where small scale phenomena might occurs and are relevant, allowing for other areas to be depicted by a rougher resolution. Embedded nesting is a finer-resolution model run within a coarser-resolution model. A two-way nesting allows for feedback between both models, in which large-scale phenomena interacts and has repercussions on fine-scale phenomena[3-14].

NWP1~NWP4 represent a target area of several thousands of square kilometers (*NWP1*) to an area covering tens of square kilometers with the target building at the center (*NWP4*). *NWP2* and *NWP3* are nested sub-domains that span hundreds of square kilometers. *NWP4* results have been treated and interpolated through a so-called quasi-coupling technique to serve as boundary conditions for the next four microscale CFD domains (*CFD1~CFD4*). A quasi-coupling technique is the combination of several, different numerical methods to link unrelated variables. In this case, mesoscale variables have been related to microscale ones[3-15]. *CFD1* portrays an area of one square kilometer while *CFD2* covers an area of two hundred square kilometers with the target building at the center. In this domain, wind pressure coefficient has been calculated at the walls of the building envelope and city urban-built air flow has been transferred to the building-indoor domain *CFD3*, the target factory building under cross-ventilation. Contaminant concentration distributions and inhalation exposure risk at the mucosal epithelial level have been predicted.

Indoor flow field and contaminant concentrations have been calculated at four different times of the day (06:00, 09:00, 13:00 and 17:00 hours) based on indoor-only sources of contaminant. Finally, flow field, turbulence kinetic energy, specific dissipation rate and contaminant concentration were transferred to *CFD4*, a local volume surrounding a human body represented by a CSP with an integrated human respiratory system (human airways model). Personal dosage by inhalation exposure was calculated at representative times of the day. Figure 3-1 depicts the outline and flow procedure of this analysis.

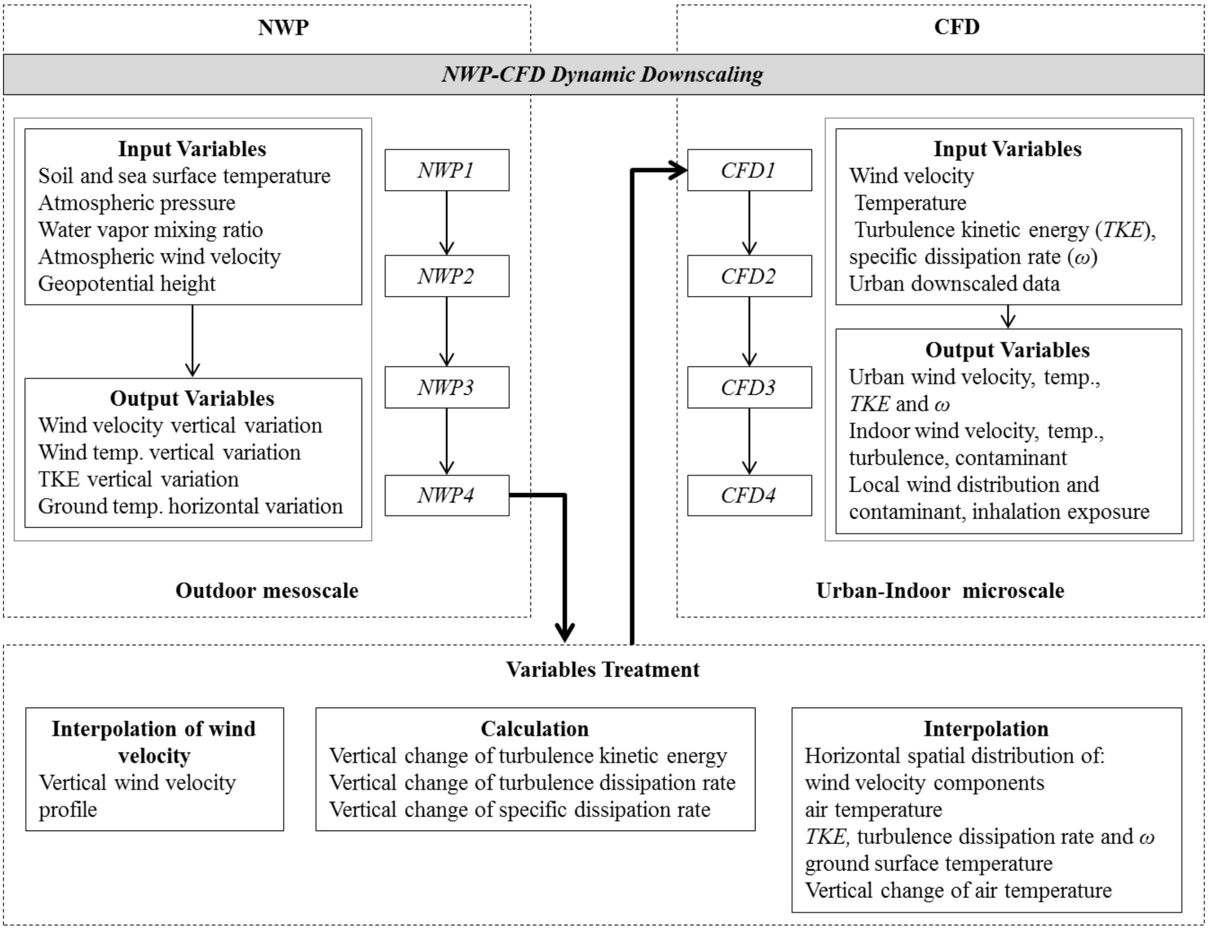

Figure 3-1. Flowchart of NWP-CFD dynamic downscaling approach

3.2.1 NWP Dynamic Downscaling

As stated in Chapter 2, the mesoscale domains of this analysis have been studied through NWP modeling and the Weather Research and Forecasting (WRF) model was used. This software was chosen due to its nesting capabilities with the possibility of analyzing domains as small as a few hundreds of meters.

The present study focuses on El Salvador, a country that targets sustainable development through industrial progression, which makes the well-being of workers an essential factor in growth, productivity and general health. In geographical terms, the country is located in Central America between latitudes 13° and 15° N and longitudes 87° and 91° W and has an area of roughly 21,000 square kilometers.

Although it is the smallest country in the region, it possesses a highly mountainous topography with over 20 volcanoes and 2 mountain ranges with a maximum elevation of 2,700 meters. This complex terrain has a considerable impact on wind flow field (velocity and vectors) and air temperature. Figure 3-2 (a) shows the nested NWP domains. *NWP1* spanned an area of 5,000 kilometers (E–W)×3,750 kilometers (S–N) with a horizontal resolution of 25 kilometers and El Salvador at the center.

The following three nested-domains had dimensions as follows: *NWP2*, 1,200 kilometers× 900 kilometers with 5 kilometers horizontal resolution and covering the southern part of Mexico and northern part of Cental America; *NWP3*, 300 kilometers×200 kilometers with 1 kilometer horizontal resolution and covering El Salvador (Figure 3-2 (b)); and, *NWP4*, 20 kilometers×20 kilometers with horizontal resolution of 200 meters covering the target urban area (Figure 3-2 (c)).

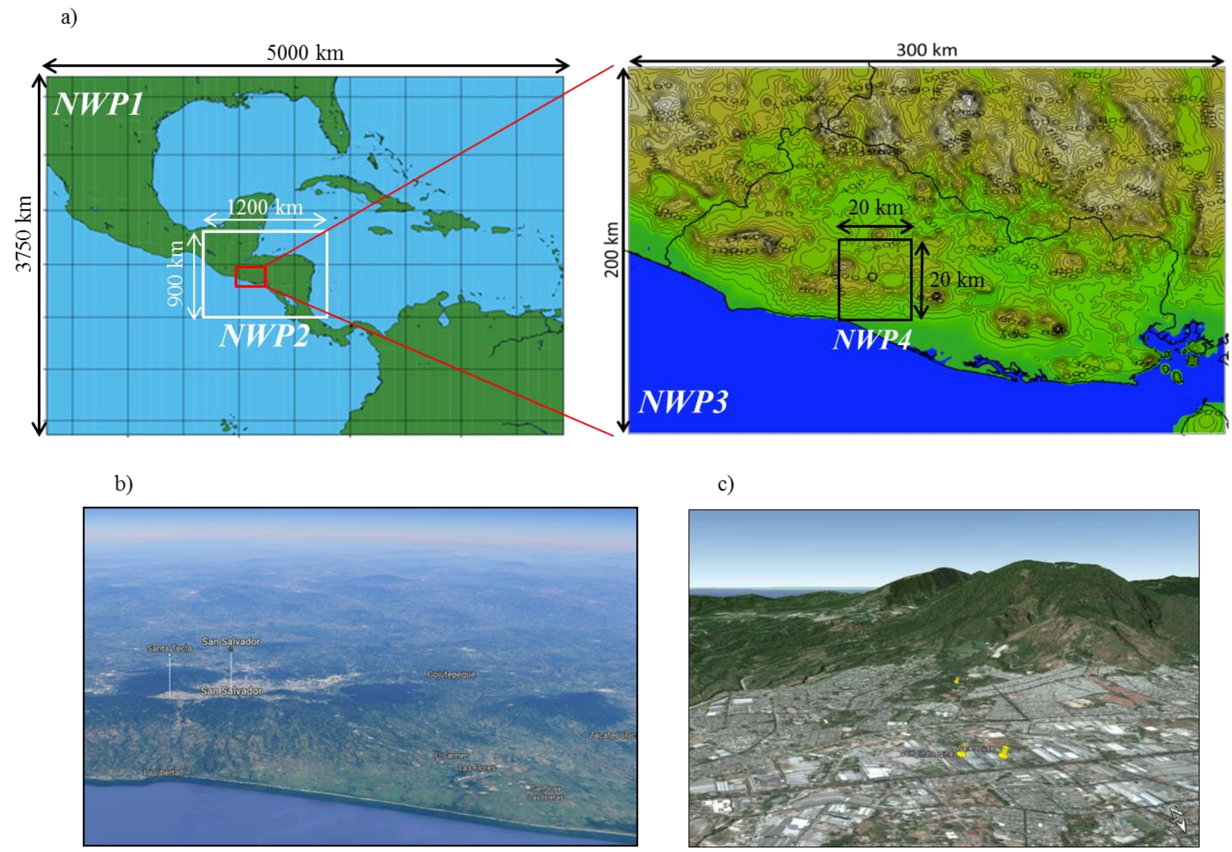

Figure 3-2. (a) NWP domains, (b) topographical terrain and (c) urban area

This study was conducted during climatologically representative summer days in April 2012. Acute or peak meteorological conditions have not been studied and El Niño-Southern Oscillation (ENSO) was not observed.

Time integration was performed during 30 days (from April 1st to April 30th) and the hourly output results of average wind velocities (three velocity components: u, v and w), turbulence kinetic energy, air and surface temperature (ensemble averaged over a month) were used.

Initial conditions such as ground surface and sea surface temperatures were obtained from the National Centers for Environmental Prediction (NCEP) Final (FNL) Operational Global Analysis data base and the spatial resolution used was 1°.

Atmospheric pressure had 26 layers of isobaric surface data – from 1000 hPa to 10 hPa – and velocity (u and v components), temperature, geopotential height and relative humidity were used for the calculation. In terms of ground and soil surface conditions, surface pressure, skin temperature (ground surface + sea surface temperature), soil temperature (four layers from ground surface) and moisture (also four layers from ground surface) were applied.

NCEP FNL data of *u* and *v* components of wind velocity, water vapor mixing ratio, potential temperature (air temperature adiabatically changed at 1000 hPa), geopotential height and dry hydrostatic pressure difference were updated every 6 hours for East, West, North and South boundary domains of *NWP1*.

For *NWP1*, relaxation lateral boundary conditions were used, i.e. a relaxation zone was implemented next to the lateral boundary to mitigate sharp gradients that exist due to data differing from the interior of the simulation domain. Furthermore, eddy diffusivity was parameterized as a function of turbulence kinetic energy and length scale.

Further schemes and conditions are described in Table 3-1[3-16].

Table 3-1. Numerical conditions for domains *NWP1* to *NWP4*

Component	**Condition and Scheme**
Cloud microphysics	Thompson scheme[3-17]
Long-wave radiation	RRTM scheme[3-18]
Short-wave radiation	Goddard scheme[3-19]
Surface layer	Monin–Obukhov scheme[3-20]
Ground surface	Noah Land–Surface model[3-21]
Atmospheric boundary layer	Mellor–Yamada–Janjic TKE scheme[3-20]
Cumulus parameterization	Grell 3D ensemble scheme (*for NWP1*)[3-22]

The Thompson scheme used for cloud microphysics introduces a new scheme with ice, snow and graupel (soft hail) processes that is suitable for high-resolution simulations. In terms of longwave radiation, the rapid radiative transfer model (RRTM) uses look-up tables to improve efficiency and accounts for multiple bands, trace gases and species.

The Goddard scheme used to calculate shortwave radiation adopts a two-stream multi-band scheme with ozone from climate and cloud effects. For ground surface, the Noah Land–Surface model allows soil temperature and moisture analysis in four layers, as well as fractional snow cover and frozen soil. The Mellor–Yamada–Janjic TKE scheme for the atmospheric boundary layer performs a one-dimensional prognostic turbulent kinetic energy with vertical mixing. Finally, in regards for cumulus parameterization, the Grell 3D ensemble scheme is a multi-closure, multi-parameter ensemble method with several sub-grid members.

3.2.2 NWP–CFD Quasi-Coupling

This study has used a quasi-coupling technique to relate mesoscale variables to the microscale environment. Due to the difference of modelling mechanisms and physical properties between NWP and CFD, data was pre-treated in order to input results of *NWP4* as boundary conditions of *CFD1*. In this section, the treatment of variables, as already illustrated in Figure 3-1, is described. Data from four different times of the day – 06:00, 09:00, 13:00 and 17:00 hours – was chosen as representative daily conditions and treated for CFD steady-state analysis.

3.2.2.1 Interpolation of Variables

Since NWP modeling focuses on mesoscale domains – course grid design –, spatial distribution of *NWP4* results was of 200 meters horizontally and 25 meters vertically. Nevertheless, microscale CFD analysis requires a finer spatial distribution of initial and boundary conditions for more stability and accuracy in terms of prediction results. From this point of view, linear interpolation between each data point was applied.

Although there are several interpolation methods, in this study, the linear technique was chosen due to its better accuracy when only scattered data is available. Specifically, in the case of NWP results, where spatial distribution was large and the spacing between each point was considerable. Different interpolation methods are visually explained in Figure 3-3.

In this study, data of wind velocity components, turbulence kinetic energy, air temperature and ground temperature has been horizontally and vertically interpolated, as explained in the next sections.

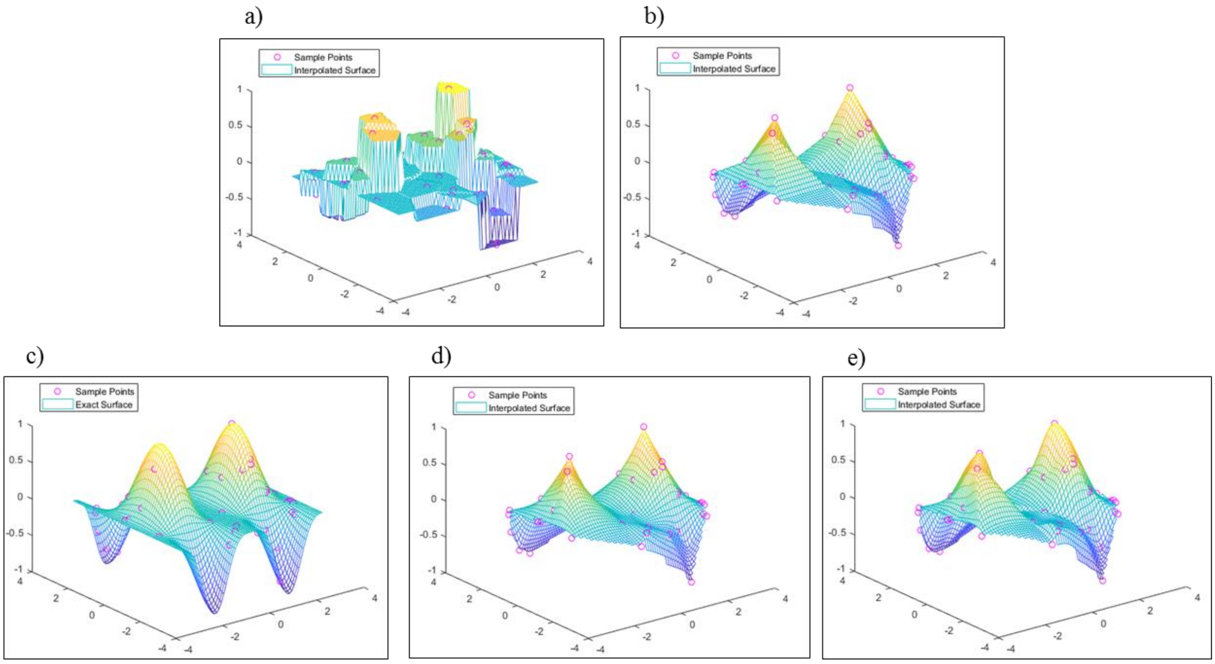

Figure 3-3[3-23]. Interpolation methods (a) nearest neighbor, (b) linear, (c) natural neighbor, (d) cubic and (d) original representative solution

- *Horizontal Interpolation*

NWP results were spatially distributed every 200 meters, horizontally. However, a closer spacing was considered crucial to adjust mesoscale wind velocity (*u*, *v* and *w* components), turbulence kinetic energy and air temperature into the microscale environment.

Therefore, spatial density of points was linearly interpolated from 200 to 30 meters through the above explained mathematical methods.

Figure 3-4 (a) shows a qualitatively visual explanation of 13:00 hours' data-interpolation at one of the lateral boundaries of domain *CFD1* for *u* velocity component. Figure 3-4 (b) exemplifies top boundary for temperature.

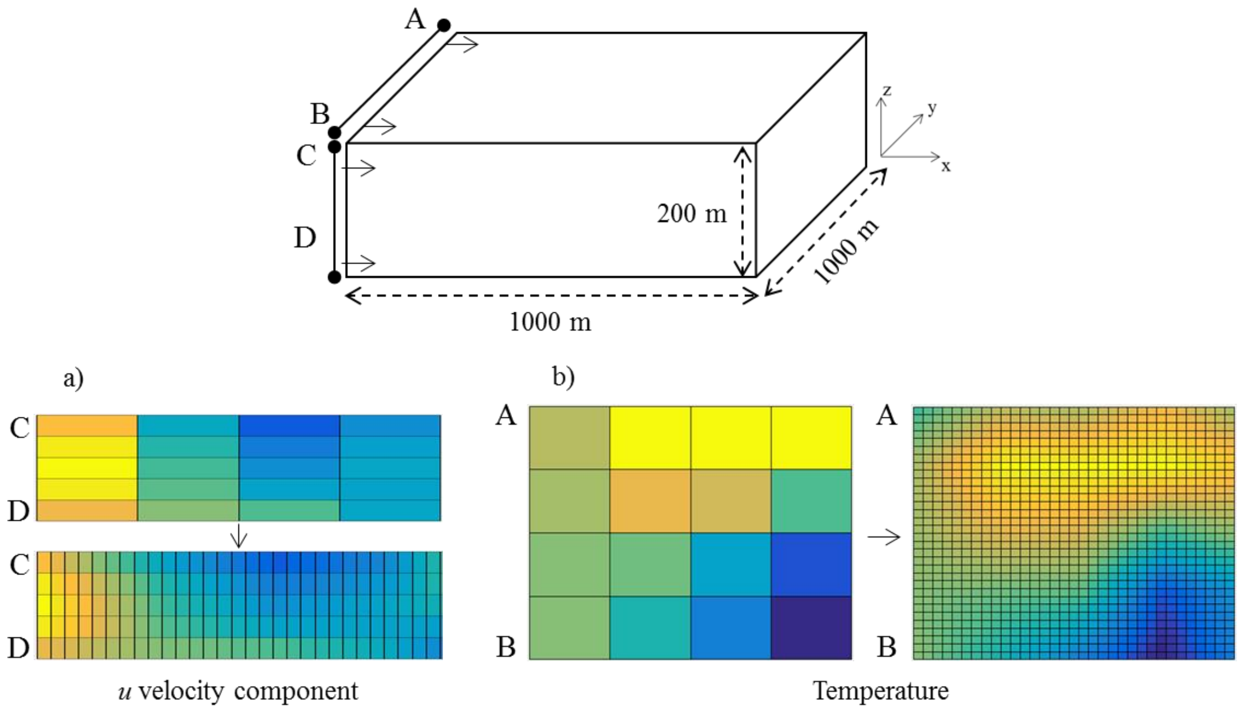

Figure 3-4. Visual exemplification of linear interpolation of 13:00 hours data at (a) one of the lateral boundaries in terms of *u* velocity component (CD section) and (b) top boundary in terms of temperature (AB section)

- *Vertical Interpolation*

This research focuses on building-indoor scale and lower scales for IAQ and inhalation exposure risk analysis (based on global climate and city urban-built transport of flow field and turbulence). Therefore, emphasis is made on heights pertinent to low-raise buildings and their paths of interaction with the outdoor environment (windows).

For this reason, data spacing above 13 meters (first grid-point of *NWP4* data results), vertically distributed every 25 meters was considered sufficient.

However, data treatment below 13 meters was considered crucial due to window height (2 meters). Consequently, air temperature below this height was linearly interpolated for a rough approximation of vertical temperature profile. Further vertical treatment of data below 13 meters is explained in the following sections of extrapolation and calculation (sections 3.2.2.2 and 3.2.2.3).

3.2.2.2 Vertical interpolation of wind velocity

It has been stated that modeling wind-speed in the lowest meters of the viscous boundary sublayer is vital. This research, therefore, interpolates wind velocity below 13 meters for a vertical wind profile through the concept explained below.

Urban canopy presents different roughness in accordance to the number of buildings in a certain region. In this situation, if the flow becomes wake-free – i.e. from individual element-roughness – it can be considered as fully adapted to upwind roughness and a spatially-averaged wind-speed profile can be therefore calculated.

There are several methods to model the wind-speed profile while at the same time taking into account ground surface roughness.

The wind power law is one of the most widely used methods because of its accuracy and usefulness in engineering applications[3-24~3-25]. This power wind law is the relationship between the wind velocities at one height and those at another. This power law can be written as[3-26]:

$$U_2 = U_1 \left(\frac{z_2}{z_1} \right)^P \qquad (3.1)$$

Where U_1 is the wind velocity at a known height, in this case, the first grid-point of *NWP4* results and z_1 is the corresponding height of 13 meters. z_2 is the corresponding height of velocity U_2, which has been interpolated every 0.5 meters until reaching ground level.

P is a function of both the atmpospheric stability in the layer over which P is determined and the underlying surface characteristics. Although several studies have focused on the calculation of *P*, which varies according to the terrain, season, time of the day, temperature and so on, this research assumes $P = 0.25$, for a ¼ power law for vertical wind profile. This wind shear exponent value has been empirically used for terrains with several buildings[3-27].

A further theoretical, visual representation of the vertical power law wind profile is presented in Figure 3-5.

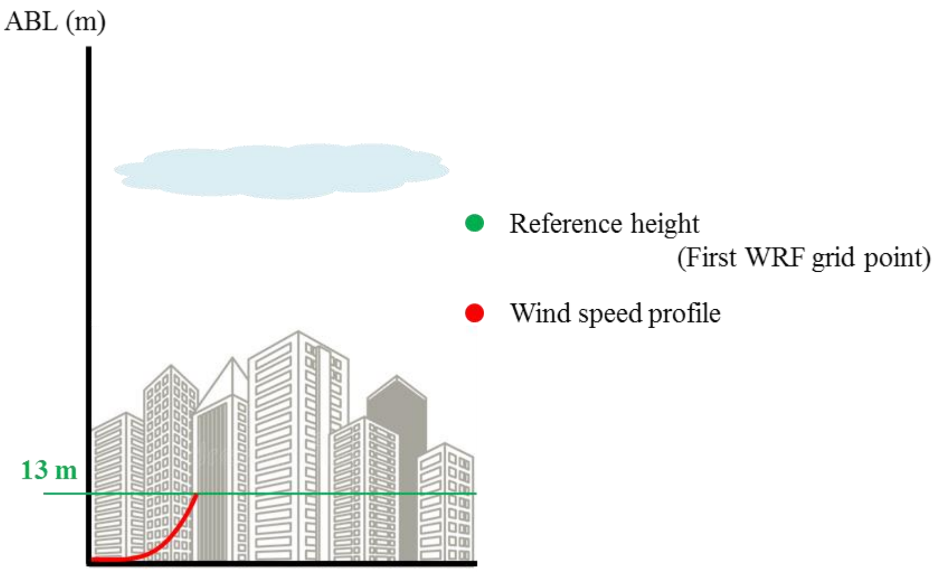

Figure 3-5. Representation of power law wind profile below 13 meters

3.2.2.3 Calculation of Variables

For *CFD1* analysis, the SST *k-ω* turbulence model has been applied, which needs additional information of variables that was not directly provided by *NWP4* results. Hence, turbulence kinetic energy (*TKE*), turbulence dissipation rate (*ε*) and specific dissipation rate (*ω*) have been calculated according to the findings made by Tominaga et al[3-28~3-30].

Turbulence kinetic energy was calculated through equation (3.2) as a function of height.

$$TKE_z = \left[0.018\left(\frac{z_2}{z_1}\right) + 0.015 \right] U_1^2 \qquad (3.2)$$

Where z_2 is the height from ground surface, spaced every 0.5 meters, z_1 is the lowest grid height corresponding to U_1^2, the square wind velocity at representative height (13 meters).

Since data of turbulence dissipation rate ε and specific dissipation rate ω was not provided directly by NWP4 data, they were calculated through equations (3.3) and (3.4) as functions of height. The constant C_μ has been set as 0.09.

$$\varepsilon_z = \frac{C_\mu TKE_z^{1.5} U_1}{4(C_\mu TKE_z)^{0.5} z_1^{0.25} z_2^{0.75}} \tag{3.3}$$

$$\omega_z = \frac{\varepsilon_z}{TKE_z} \tag{3.4}$$

Treated data explained in this section was input into *CFD1* as boundary conditions for the four vertical lateral planes facing North, South, West and East directions; the top boundary representing maximum domain height and the ground surface of the domain. Profiles have been created for data input, further explained in the next section (3.2.3).

3.2.3 CFD Dynamic Downscaling

CFD is commonly used for urban and micro-scale studies because of its productive performance and ability to identify complex air flows and turbulence in domains that use fine grids of up to 2 square kilometers.

This section describes the procedure for the CFD analysis of domains *CFD1~CFD4* through dynamic downscaling under steady-state at four different times of the day: 06:00, 09:00, 13:00 and 17:00 hours.

NWP4 results were input as inflow boundary conditions as point profiles.

The point cloud (group) of the point profiles is then interpolated to obtain values at the boundary faces. However, in order to get an accurate interpolation, the profile must contain a high density of points; hence, the need for data treatment procedures explained in the previous section is hereby clarified.

Results obtained in *CFD1* were further interpolated into domains *CFD2*, *CFD3* and *CFD4*, where grids have been carefully selected and grid independence check has been conducted. Furthermore, benchmark test guidelines for outdoor and indoor CFD applications have been followed in order to maintain quality control[3-31~3-33].

3.2.3.1 Urban Environment

Treated climate results from domain *NWP4* were used as inflow lateral boundary conditions for domain *CFD1*, as previously explained. *CFD1* was designed as a local city urban-built microscale region with an area of 1 square kilometer; domain height was of 200 meters above ground level. This region represents real topography and its ground surface was, therefore, not uniform.

Real terrain data was obtained through public ALOS data, the Advanced Land Observing Satellite launched by Japan Aerospace Exploration Agency in 2006. The four corner coordinates that encase the target region, expressed in decimal latitude and longitude and written clockwise from the top-left corner are:

(-89.1425, 13.7011), (-89.1332, 13.7011), (-89.1332, 13.6920) and (-89.1425, 13.6920). Resolution of elevation points for mesh design was of 30 meters.

Figure 3-6 (a) shows the real topographical area surrounding the target region and Figure 3-6 (b) illustrates the 1 square kilometer topographical area.

Domain *CFD1* has been discretized by an unstructured tetrahedral mesh of 2.78 million elements, where minimum grid cell size was of 5 meters near the lateral boundaries.

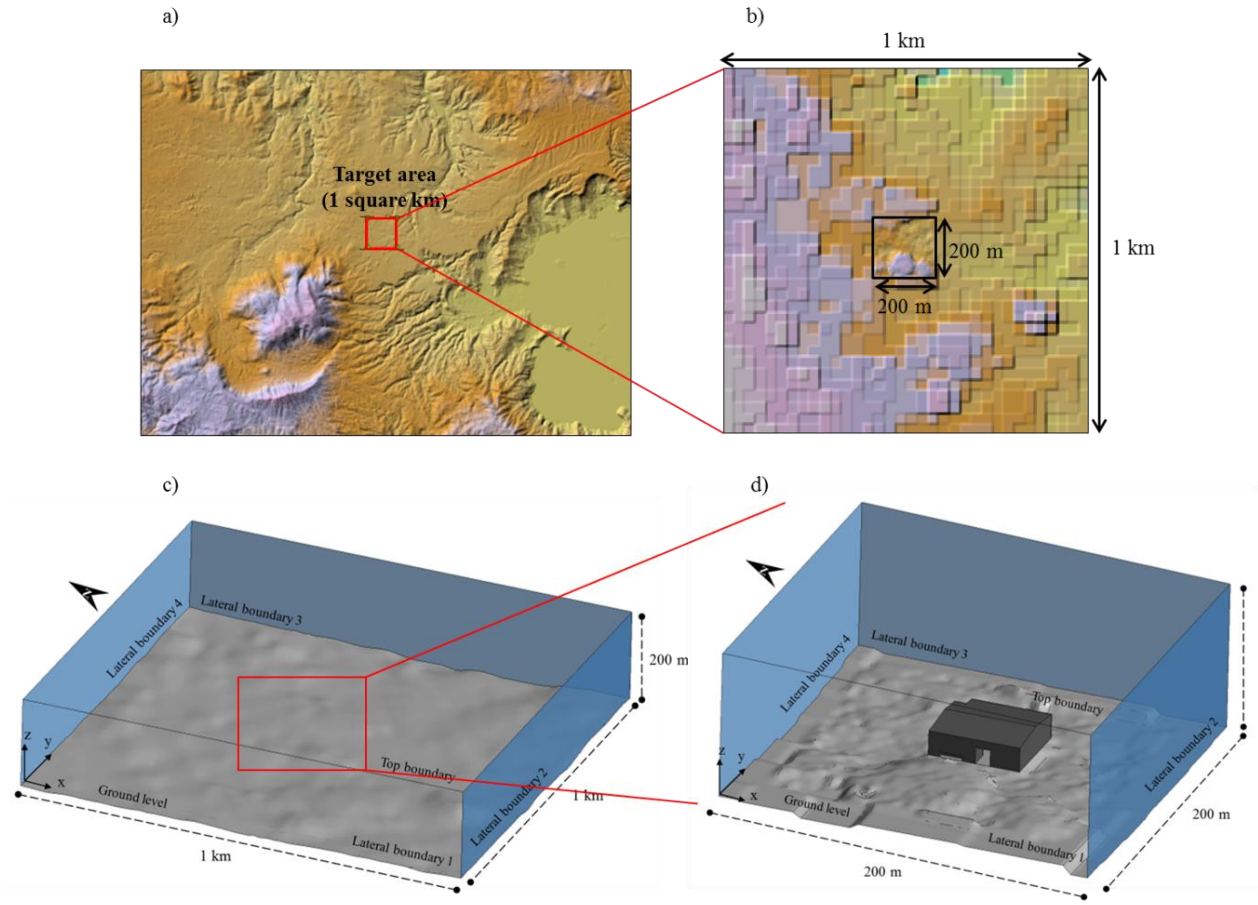

Figure 3-6. (a) Satellite image of topographical region surrounding target area, (b) Satellite image of topographical 1 km^2 region with the finer 200 m^2 area at the center, (c) CFD design of 1 km^2 topographical area and (d) CFD design of 200 m^2 topographical area

Figure 3-6 (c) shows its design created by using ANSYS/ICEM 16.0. Further mesh designed is depicted in Figure 3-6 (a). Figure 3-6 (b), (c) and (d) show mesh design of particular surfaces.

The SST *k-ω* model was used for the turbulence model due to its advantage in dual performance and accuracy when simulating flow in the viscous sublayer and free shear flow, as explained in section 2.3.4.1.

Further numerical and boundary conditions are expressed in Table 3-2.

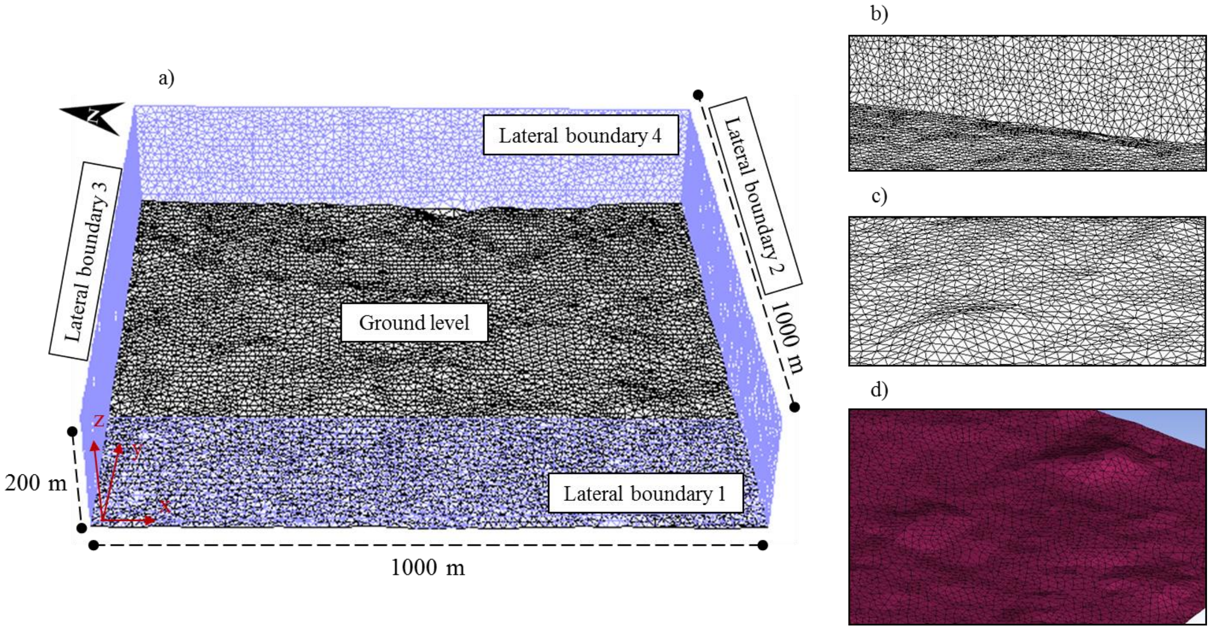

Figure 3-7. Mesh design (a) of the entire *CFD1* domain, (b) at the lateral boundaries, (c) of the ground surface and (d) closer depiction of real ground topology

Table 3-2. Numerical conditions for domains *CFD1*

Component	**Condition**
Turbulence Model	SST Type *k-ω* model (3D calculation)
Mesh	2.78 Million Mesh (unstructured, tetrahedral)
Scheme	Algorithm : SIMPLE Convection Term : Second Order Upwind
Inflow Boundary(above 13 m)	U_{in}, T_{in}, k_{in} = *NWP4* treated data ε_{in}, ω_{in}= equations (3.7) and (3.8)
Inflow boundary(below 13 m)	U_{in}= equation (3.5) k_{in}, ε_{in}, ω_{in} = equations (3.6), (3.7) and (3.8)
Outflow Boundary	U_{out} ,T_{out}, k_{out} = Free Slip
Wall Boundary	Velocity: No Slip Temperature: T_{srf} = *NWP4* data (point profile)

Distribution results of average velocities (*u*, *v*, and *w*), turbulence kinetic energy, turbulence dissipation rate, and temperature were transferred into a smaller urban-built domain *CFD2*, and input as inflow boundary conditions in the manner of profiles through the same method previously described. Each data point was interpolated through zeroth order (nearest neighbor) method.

Therefore, for each cell face at the given boundary, the profile value located closest to the cell was used during calculation. Although a high density of points is required, this method was chosen because it requires few computational resources and has a high computational speed.

Domain *CFD2* covered the smallest urban-built area of 200 square meters. Real elevation data was obtained through ALOS using AW3D high-resolution map, which was developed jointly by NTT DATA and Remote Sensing Technology Center of Japan.

Resolution of elevation points was of 5 meters. Figure 3-6 (b) shows real terrain of this region.

In this domain, the factory building was set at roughly the center. Domain height was 100 meters above ground level, which was non-uniform. This region was discretized by an unstructured tetrahedral mesh of 2.45 million elements and grid cell size ranged from 5 meters at the boundaries to a few centimeters at the windows of the building envelope. ANSYS/ICEM 16.0 was also used for its design, which can be comprehended through Figure 3.-6 (d). Figure 3-8 shows detailed mesh design.

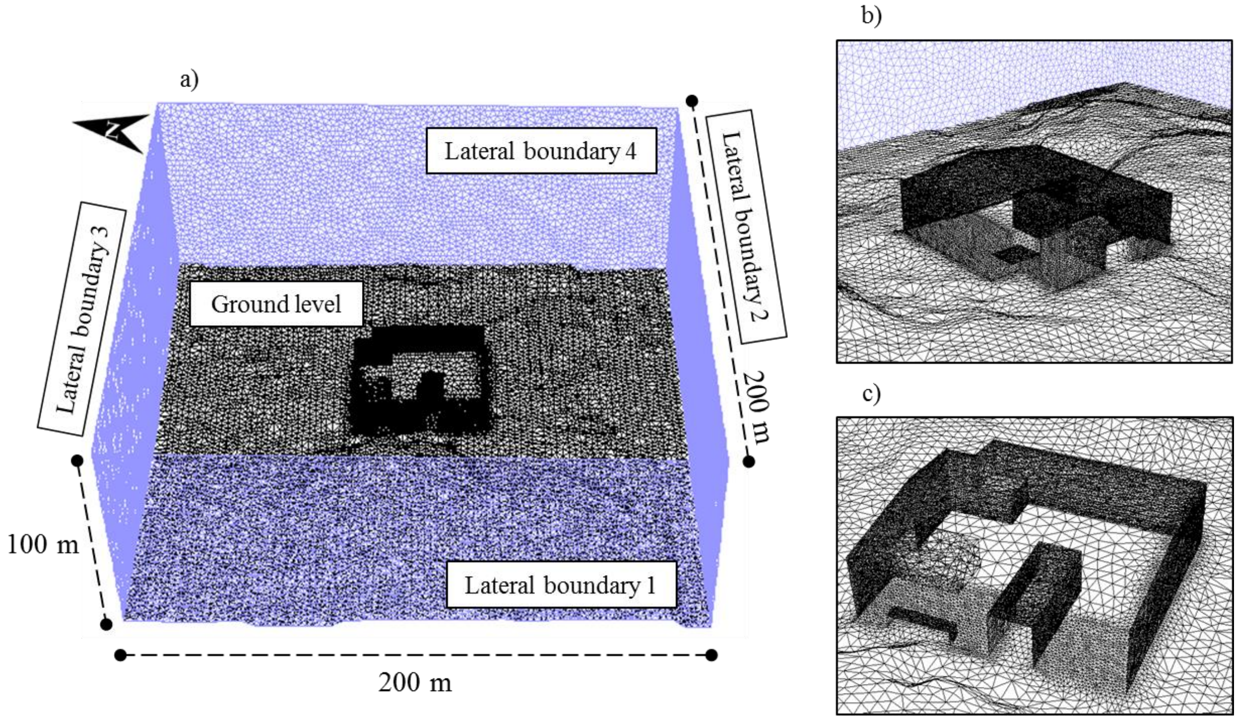

Figure 3-8 Mesh design (a) of CFD2 domain, (b) of ground near factory (c) of factory

The SST *k-ω* model was also used to simulate turbulence in *CFD2*. Previous studies have shown the numerous merits of the SST *k-ω* model when calculating cross-ventilation and wind around a building[3-34~3-35].

Further numerical conditions are presented in Table 3-3.

To transport city urban-built flow field, the concept of wind pressure coefficient has been applied. Difference of pressure at walls and flow paths has been used to generate indoor wind velocity distribution.

Other variables of turbulence and air temperature have also been transported to the building-indoor environment and contaminant concentration at different scales has been predicted, as described in the following sections.

Table 3-3. Numerical conditions for domain *CFD2*

Component	**Condition**
Turbulence Model	SST Type k-ω model (3D calculation)
Mesh	2.45 Million Mesh (unstructured, tetrahedral)
Scheme	Algorithm : SIMPLE Convection Term : Second Order Upwind
Inflow Boundary	U_{in}, T_{in}, k_{in}, ω_{in} = *CFD1* interpolated data
Outflow Boundary	U_{out} ,T_{out}, k_{out} = Free Slip
Wall Boundary	Velocity: No Slip Temperature: T_{srf} = *CFD1* data (point profile)

3.2.3.2 Pressure Analysis: wind pressure coefficient

Knowledge of pressure distribution on outside walls of a building is fundamental to assess wind-induced natural ventilation – i.e. cross-ventilation – and indoor contaminant distributions generated by air movement.

This pressure distribution can be influenced by a large number of factors like approaching flow, urban surroundings, building geometry and wind direction. Building façade has a great impact on wind pressure distribution of walls and roofs. Wind pressure coefficient (C_p) can be determined through:

i. on-site full-scale measurements,
ii. wind-tunnel measurements and
iii. numerical simulation through CFD.

Although full-scale measurements have the merits of a real-situation study, the collected data refers to a limited number of points with uncontrolled boundary conditions. Similarly, wind-tunnel measurements offer a limited number of measured points although the boundary conditions tend to be more controlled – sometimes to the point of unreality compared with the real-case scenario –.

However, CFD provides data in all the points of the computational domain and does not suffer from incompatibility with reality because the scale can be adjusted and the boundary conditions fully controlled[3-36].

CFD has been used to determine mean wind-induced pressure distributions on building envelopes. This study focuses on C_p concept, where C_p distributions on the outside walls and windows of the building envelope have been predicted in order to transport city urban-built flow through pressure differences at different points by using the following equation:

$$C_p = \frac{P_{wall} - p}{\frac{1}{2}\rho v^2} \qquad (3.5)$$

Where $P_{wall} - p$ represents the pressure difference between the outside wall and a determined representative point, ρ is the air density and v^2 is the square wind velocity at the windows.

In this study, 42 windows of dimensions 1.5 m × 2.0 m were fixed as building openings, where urban flow field in *CFD2* has been transported to indoor environment *CFD3* for a building-indoor scale analysis.

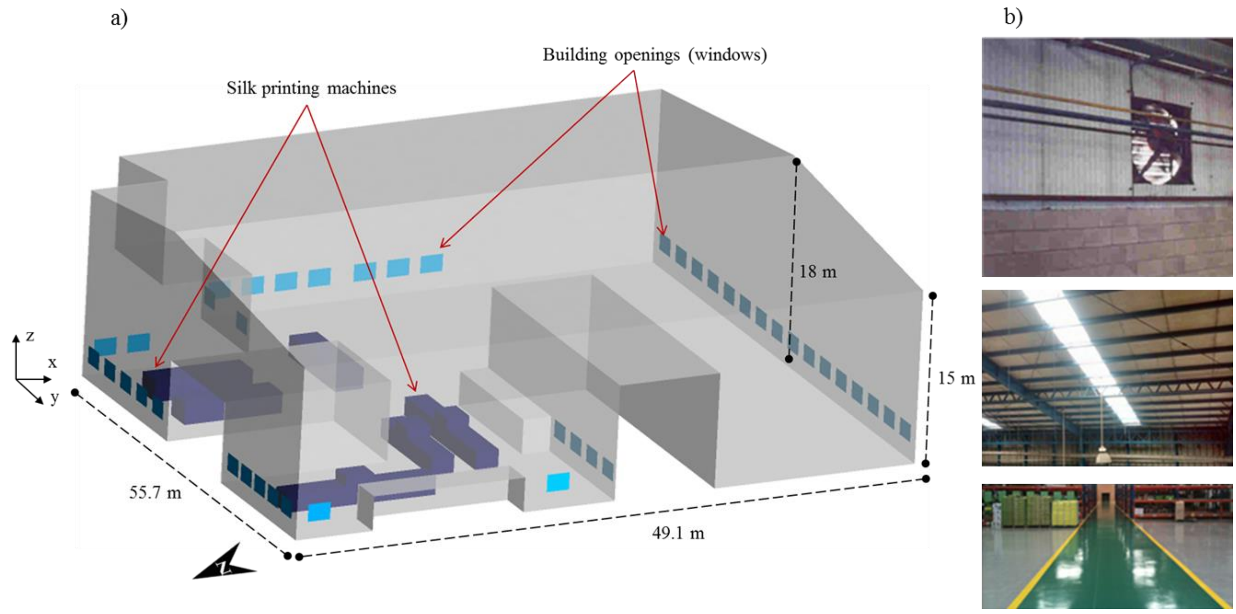

Figure 3-9. (a) Layout of factory model and geometry (b) Inside appearance of factory

3.2.3.3 Indoor Environment

The target building factory – textile industry – that represents *CFD3* domain analyzed in this study is located in Soyapango city, El Salvador, East of San Jacinto Mountain. It has an elevation of 650 meters above sea level and a North latitude of 13° 41.3' and West longitude of 89° 8.6'. Simplified geometry and building characteristics are presented in Figure 3-9.

Dimensions of this factory are of 55.7 m $\times$49.1 m with a gabled roof design as depicted in Figure 3-9 (a). Main space area is of 2452.22 m^2. Figure 3-9 (b) shows the inside characteristics of the building at determined points. The loading area for trucks in the middle of the building, which is an outside space, has been disregarded.

The total space was discretized by an unstructured tetrahedral mesh of 2.59 million elements. Minimum grid size was roughly one centimeter at the windows and ANSYS/ICEM was used to create the geometry. Figure 3-10 (a) shows mesh design of the target factory.

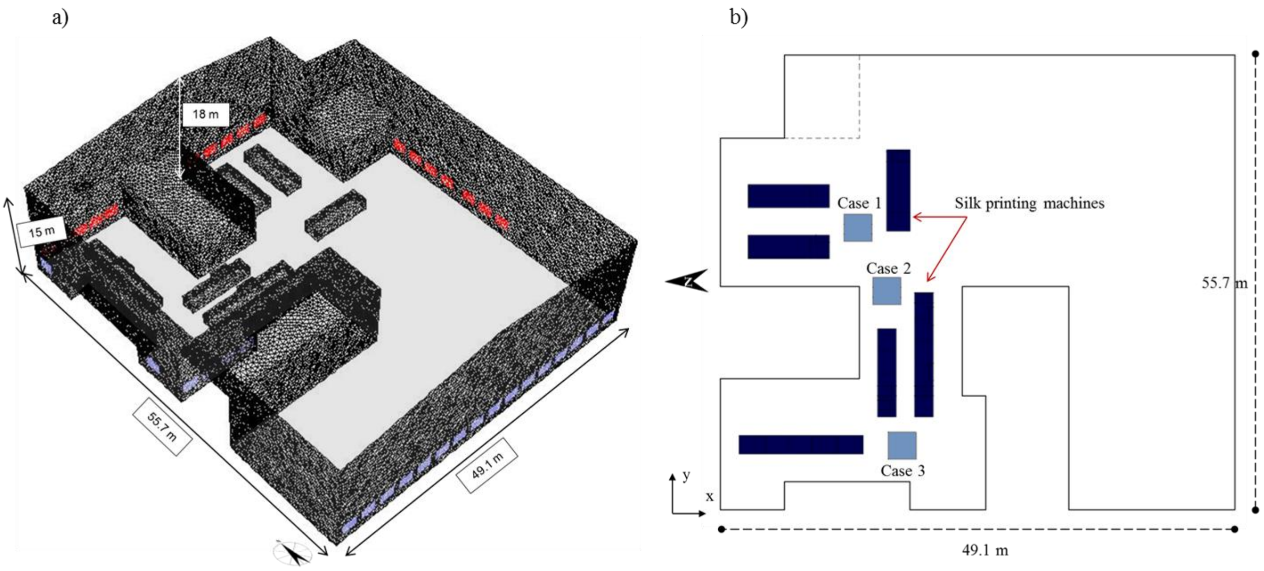

Figure 3-10. (a) Mesh design of factory model and (b) Location of machines and CSP inside factory

Table 3-4 describes the construction materials of the building, which become relevant in terms of heat transfer coefficient (w/m^{2}k) to analyze the temperature and radiation model inside the building. No insulation material was considered so as to fundamentally maintain the real building characteristics.

Furthermore, the spaces of three rooms have been eliminated of the overall enclosure: workers' lockers' room, bathrooms and picture processing room. These spaces possess their own ventilation system and the doors remain closed during working time, separating them from the main space.

Table 3-4. Construction materials of factory

Wall	Material	Heat Transfer Coefficient (w/m^2-k)
Upper outer wall	Galvanized Steel Sheet	9,000
Lower outer wall	Conventional Concrete Block	5.9
Inner walls	Conventional Concrete Block	5.9
Floor	Reinforced Concrete	10.87
Roof	Galvanized Steel Sheet	9,000
	Transparent Acrylic Sheet	143.75

To analyze IAQ inside the factory, six silk printing machines were set as indoor contaminant and heat sources. Cyclohexanone (gas phase) was set as the target chemical – indoor-source only –, with a generation rate of 8.54 g/s.

Furthermore, surface temperature of the machines was set to 333.15 K (60° C) and 338.15 K (65°). Contaminant and temperature settings correspond to the production framework of the textile printing industry in El Salvador. The model layout of the machines is explained in Figure 3-11.

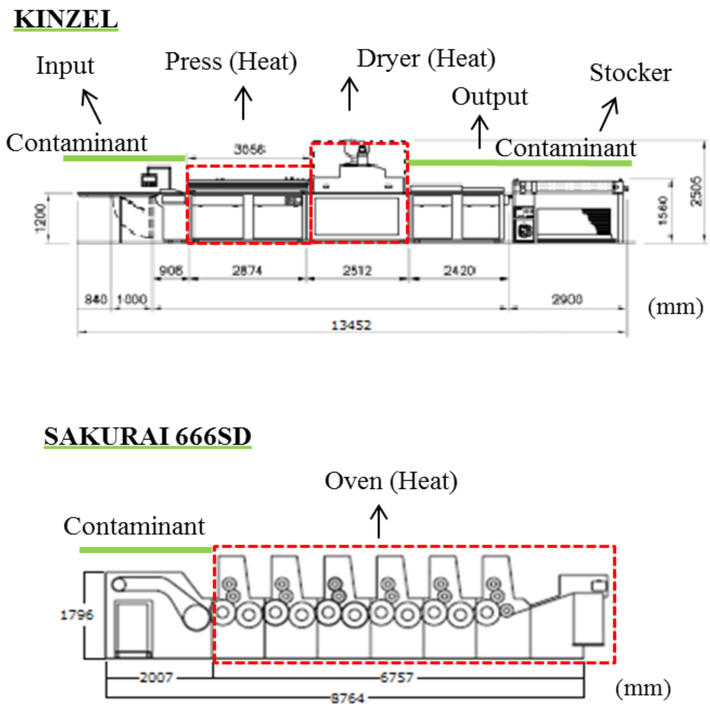

Figure 3-11 Layouts of silk printing machines

The SST *k-ω* model was once again used to analyze the turbulence inside the building to keep consistency with the other domains. The S2S radiation model was adopted for long-wave radiative heat transfer. Solar heat load distributions were calculated at the external wall surfaces through a solar-ray tracing method in order to consider short-wave radiative heat transfer.

A simulation of radiation-convection-conduction was performed indoors. Inflow-boundary conditions are: static pressure given by C_p, turbulence kinetic energy and specific dissipation rate, and outdoor air temperature.

In terms of contaminant concentration analysis, cyclohexanone adsorption was disregarded at the indoor wall surfaces through a gradient zero-type condition. No ambient air pollution was considered.

Table 3-5. Numerical conditions of *CFD3*

Component	Condition
Turbulence Model	SST k-ω Model
Mesh	2.59 million mesh (Unstructured)
Scheme	Algorithm : SIMPLE ; Convection Term : 2nd Order Upwind
Inflow Boundary	P_{in}, T_{in}, k_{in}, ω_{in} = *CFD2* data
Outflow Boundary	P_{out}, T_{out}, k_{out}, ω_{out} = *CFD2* data
Heat Source	333.15K(Kinzel) , 338.15K(Sakurai)
Radiation	View Factor : Hemicube Method Solar Load : Solar-Ray Tracing
Scalar	Cyclohexanone, Scalar Type : Passive Contaminant
Wall Boundary	Velocity: No Slip

A steady-state, non-uniform contaminant concentration distribution analysis was performed at four different times of the day: 06:00, 09:00, 13:00 and 17:00 hours to analyze the impact a change in cross-ventilation has on IAQ and inhalation exposure risk. Further numerical conditions are shown in Table 3-5.

To be able to analyze the effect of various contaminant concentrations in the human body, indoor results of flow field and pollutant from *CFD3* were further transported to *CFD4*, the final CFD domain which enclosed a CSP in a local space of 3×3×3meters. A male adult model in orthostatic position that reproduces the physical characteristics of a Japanese person was set at the middle.

This geometry had been previously created by using POSER 4.0J (Curious Labs Inc.) and the posterior data was read using DXF format and adjusted through CAD. Final geometry simplification was obtained by applying GRIDGEN V15 (VINAS Co. Ltd.).

CFD4 domain was discretized by an unstructured mesh of 1.95 million elements and minimum grid size was less than one millimeter near the cutis (walls) and nares (inflow). A numerical model representing the human respiratory system was integrated into the CSP to analyze wind-induced inhalation exposure risk.

The respiratory tract started from the nasal cavities (nares) and ended at the fourth bifurcation of the bronchial tubes. It was discretized by a mesh of 7.53 million elements.

Figure 3-12 (a) shows CSP domain with the integrated respiratory tract; Figure 3-12 (b) shows further details of CSP and mesh design of the CSP head and Figure 3-12 (c) shows geometry design of respiratory tract and bronchial tubes' mesh design

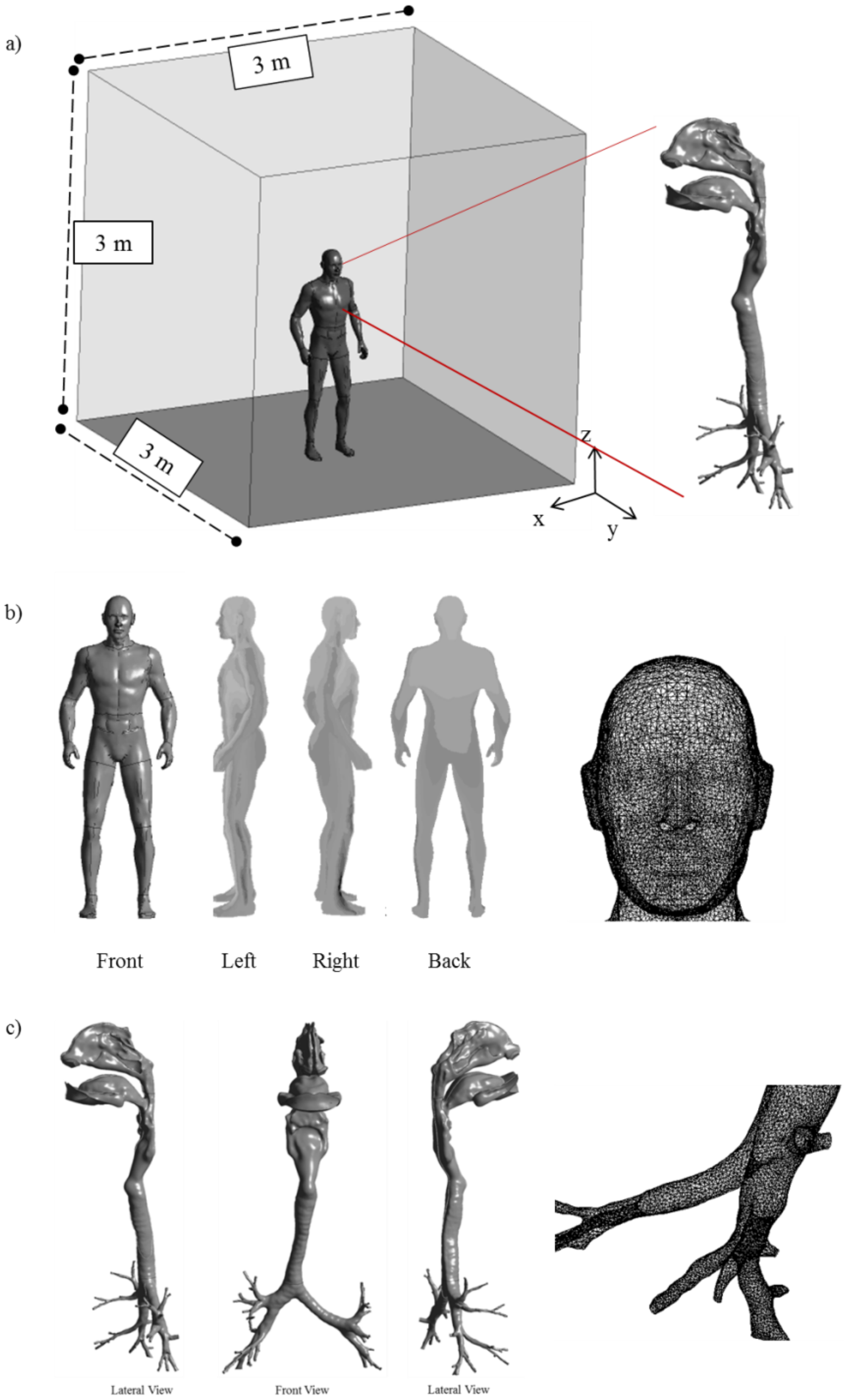

Figure 3-12 (a) CSP domain with the integrated respiratory tract b) geometry and mesh design and (c) respiratory tract geometry and mesh design

As depicted in Figure 3-10 (b), three cases of variation of CSP location-dependence of inside the factory have been considered so as to relate positioning and building design to pollutant exposure levels. They have been denominated as Case 1, Case 2 and Case 3.

Turbulence in *CFD4* has been analyzed through time-averaged Navier–Stokes and continuity equations, as explained in Chapter 2. In this case, the low Reynolds k-ε (Abe–Kondo–Nagano) model was applied for air flow analysis around the CSP. Prediction accuracy of this model as a function of the Reynolds number has been previously reported[3-37].

Table 3-6. Numerical conditions of *CFD4*

Component	**Condition**
Turbulence model	Low Reynolds number k– ε model (ANK) (3D calculation)
Mesh	CSP: 1.95 million Human airways: 7.53 million
Algorithm	SIMPLE
Scheme	Convection term: Second-order, upwind
Inflow boundary	U_{in}, T_{in}, C_{in}, k_{in}, ε_{in} = *CFD3* indoor data
Human surface (skin)	Velocity, k_{wall} : No slip Constant skin temperature = 307.15 K
Human breathing	U_{in} = 0.478 m/s (constant inhalation) $k_{in} = 3/2 \times (U_{in} \times 0.1)^2$ $\varepsilon_{in} = C_\mu^{3/4} \times k_{in}^{3/2}/l_{in}$ $C_\mu = 0.09$, $l_{in} = 10^{-3}$ m Scalar type : Passive contaminant $C_{inhaled}$: Gradient zero condition
Wall boundary	Velocity: No slip

Contaminant entered the human body through both nares of the CSP at a constant respiration rate 0.45 m^3/h. *CFD3* data of wind velocity components (*u*, *v*, *w*), turbulence kinetic energy *k* and turbulence dissipation rate *ε*, and cyclohexanone concentration was interpolated to the lateral boundaries of *CFD4*. Further numerical conditions are depicted in Table 3-6.

Finally, inhalation exposure risk affecting the mucosal epithelial cells of the nasal cavity, pharynx, larynx and upper trachea are calculated through equation (3.6):

$$IC_v = V_i \times A_n \times C_n \tag{3.6}$$

Where IC_v is the inhaled volume of the contaminant through the nares, V_i is the inhalation velocity at the nostrils, A_n represents the area of both CSP nares and C_n is the contaminant concentration at the nostrils calculated through area-weighted average.

Validation results for the flow and convective heat transfer rate of the CSP through wind tunnel experiments have been previously reported[3-38]. Perfect sink condition – i.e. zero-tissue surface concentration in the air-tissue interface – has been assumed for deposition in the respiratory tract[3-39~3-41].

3.3 RESULTS AND DISCUSSION

This section presents the results of the overall NWP–CFD dynamic downscaling steady-state procedure. NWP results have been averaged over a 30-day period while CFD results are shown at the four times of the day analyzed: 06:00, 09:00, 13:00 and 17:00 hours.

3.3.1 NWP Dynamic Downscaling Results

Figure 3-13 (a) shows a time-series of temperature and wind direction vectors over the mesoscale domain *NWP3* at 12:00, 13:00 and 16:00 hours (30-day averaged).

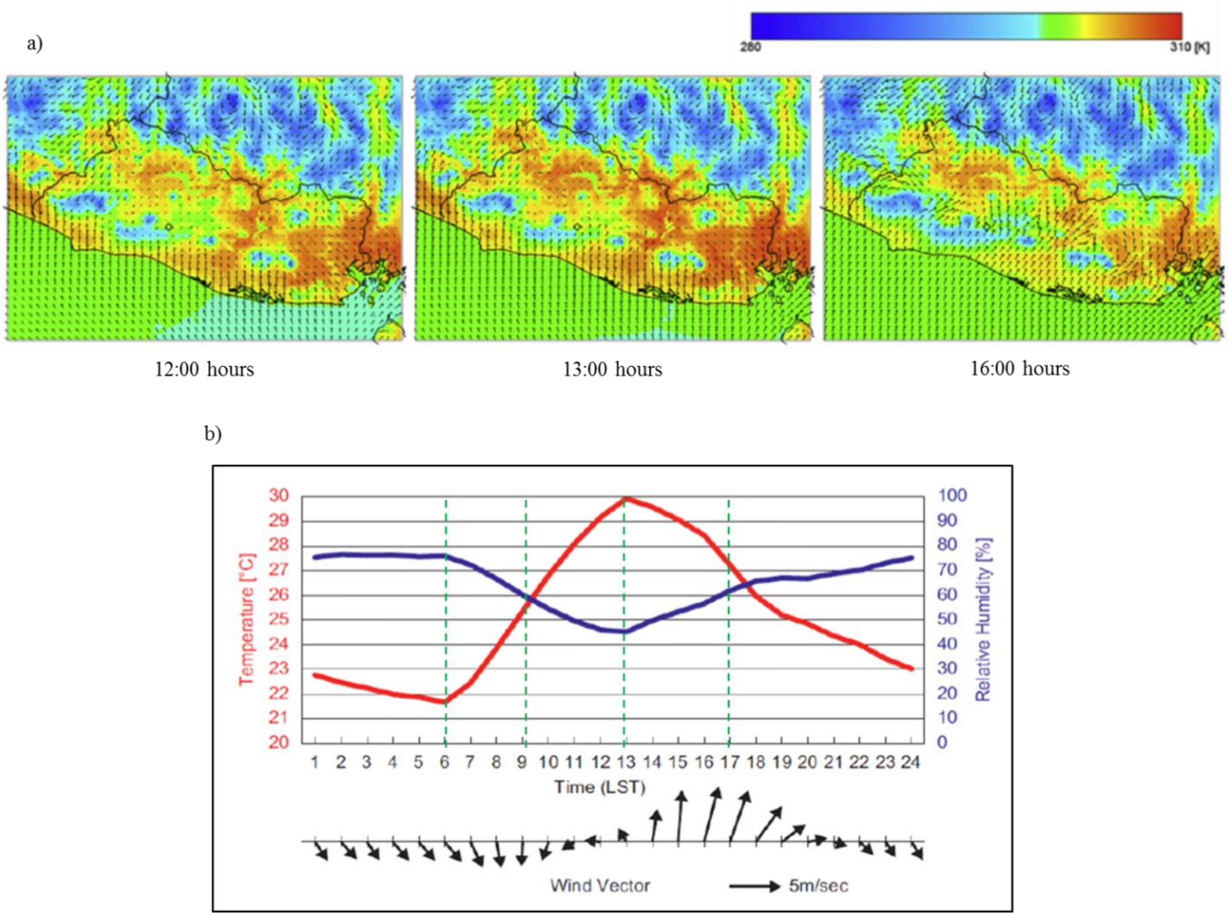

Figure 3-13. Mesoscale results of (a) temperature at 2 meters height and wind vectors at 10 meters height at three different times of the day over a month period; (b) temperature and wind velocity in *NWP4*

High temperature at 13:00 hours can be appreciated, though relatively high levels are maintained throughout the day, consistent with summer settings. These results are also in accordance with weather patterns during the months of November–April, when trade winds are prevalent from the Northeast. Figure 3-13 (b) presents mesoscale results of temperature, humidity, wind velocity and wind direction during a period of 24 hours (30-day averaged) in domain *NWP4*. Peak temperature was consistent with *NWP3* at 13:00 hours. High urban wind velocity occurred at 17:00 while weak urban air persisted at 13:00. This roughly stagnant air movement accounts for a higher temperature during this dime. These mesoscale results were treated and interpolated into domain *CFD1*. Designated times used for the steady-state downscaling analysis have been identified by using green lines.

3.3.2 CFD Dynamic Downscaling Results

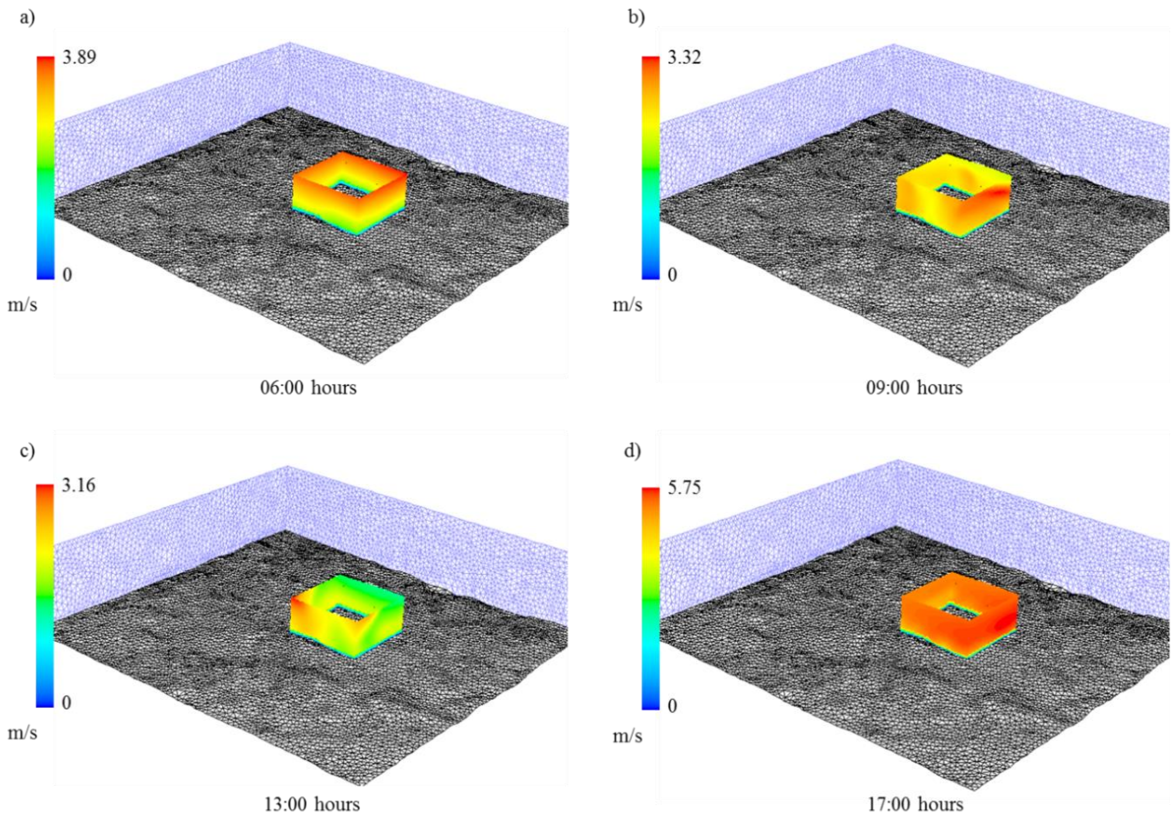

Figure 3-14 *CFD1* results of wind velocity magnitude at the lateral boundaries surrounding the building at (a) 06:00, (b) 09:00, (c) 13:00 and (d) 17:00.

Urban results of wind velocity at the lateral boundaries where the target factory is roughly located (in *CFD1*, the one square kilometer domain) at the four different times of the day, are presented in Figure 3-14.

High urban wind velocity was confirmed in this domain at 17:00 while weaker urban air occurred at 13:00 and thus accurately downscaled in agreement with NWP results.

Figure 3-15 (a) shows urban wind velocity results in domain *CFD2* on a horizontal plane relevant to window height. Factory building was located at the center of the domain. Peak conditions were shown at 17:00 hours with strong incoming wind from the South. Wind velocity vectors are also presented to portray wind direction around the building façade. Building geometry directly impact flow field distribution around at nearby distance, dampening velocity.

In this study, only one building was analyzed for demonstrative purposes and effects of urban canopy and urban heat island have not been considered. Future studies should introduce a more complex urban domain which evaluates ground surface topography and other urban-built topology.

Figure 3-15 (b) presents C_p distribution at the exterior walls the building envelope and the averaged C_p value per wall. Figure 3-15 (c) shows C_p distribution at the window openings and the averaged C_p value per window.

It can be appreciated that urban wind direction had a major direct impact in the pressure distribution along the exterior walls and windows, with positive coefficients for windward façades and negative coefficient for leeward ones. Fluctuating flow field was confirmed to be transported to the indoor environment.

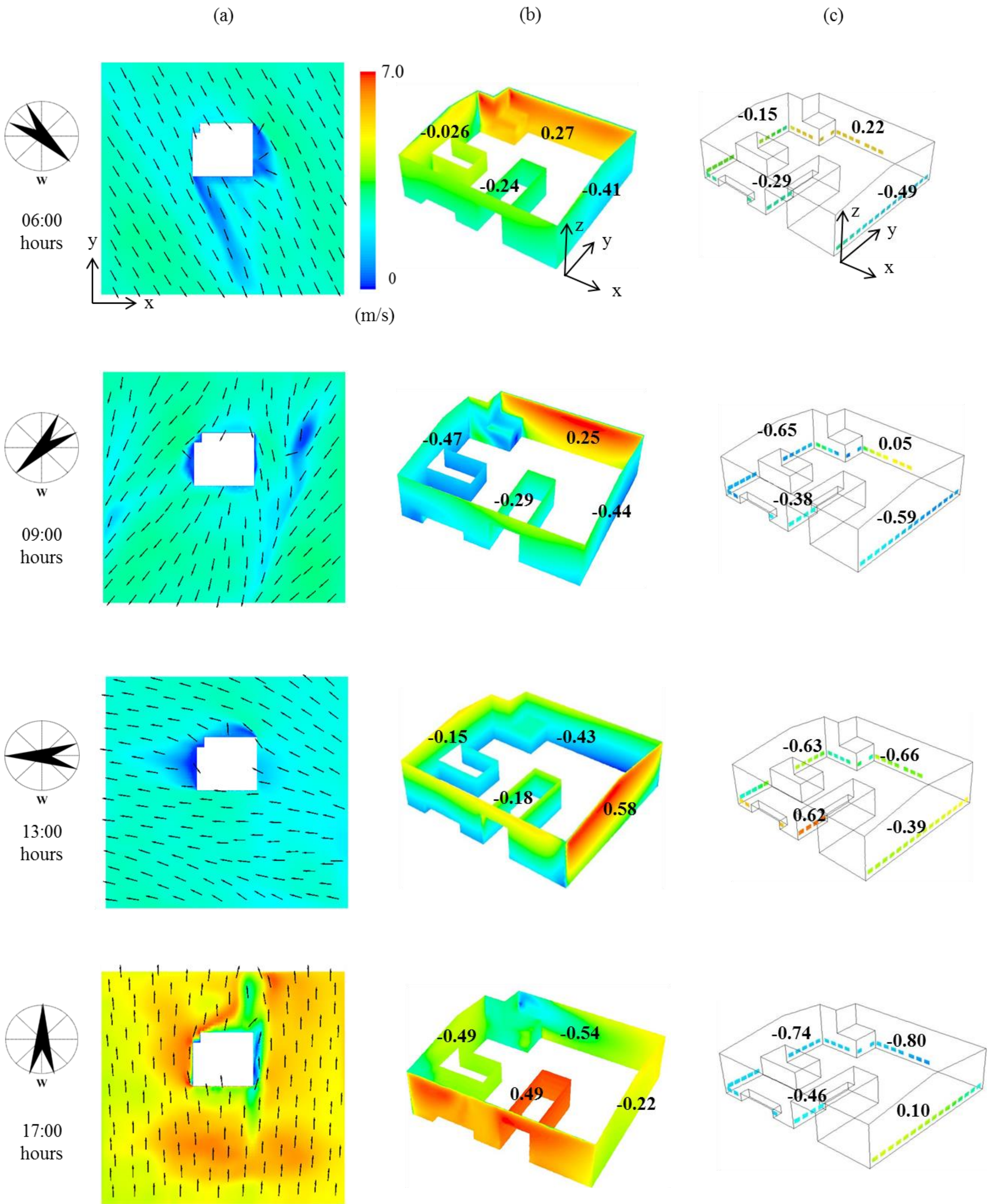

Figure 3-15. Results of *NWP2* at different times of the day of (a) urban wind velocity and wind vectors (b) C_p distribution at the exterior walls and (c) C_p distribution at window openings

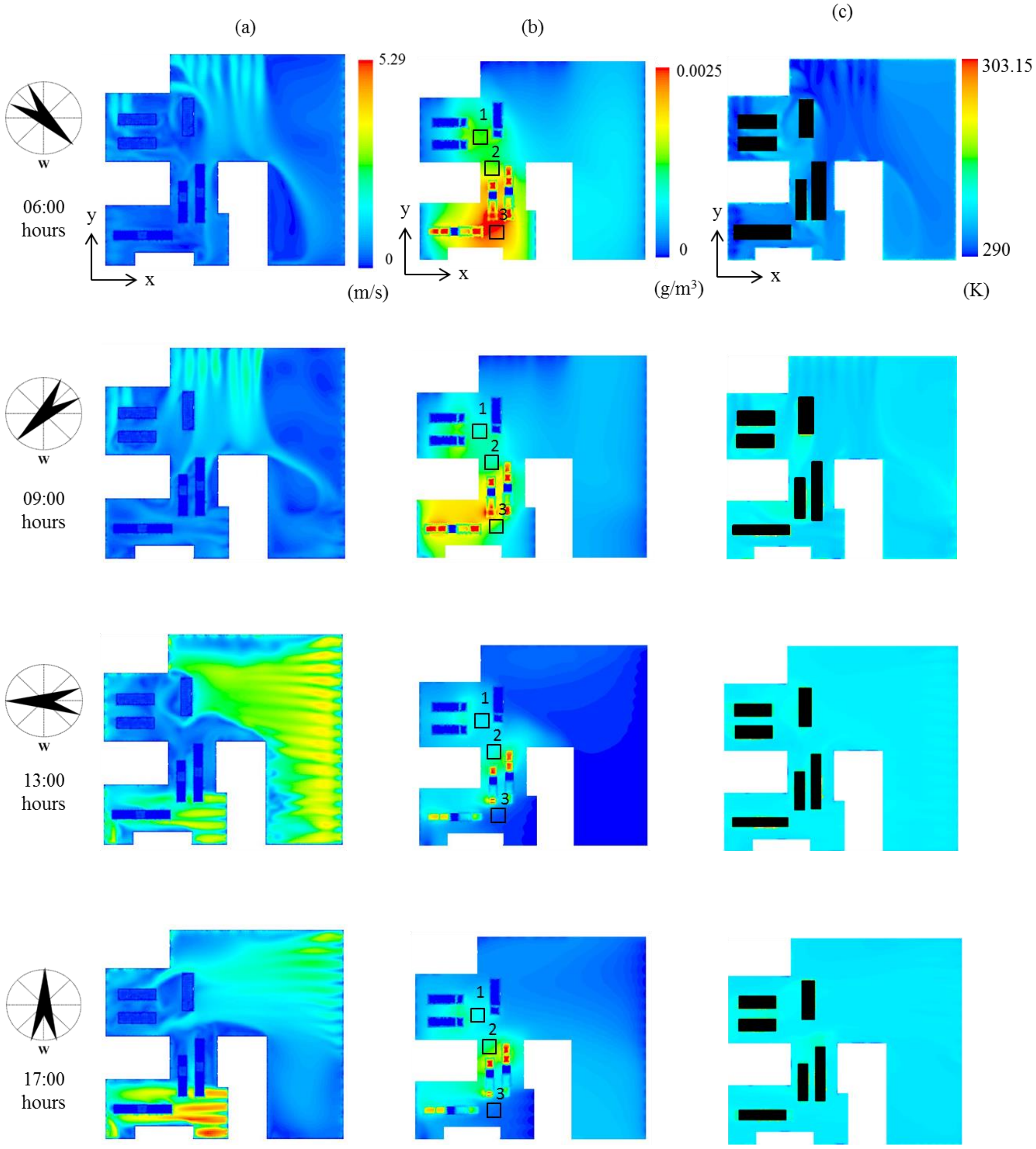

Figure 3-16. Indoor results in *CFD3* of (a) wind velocity magnitude distributions, (b) cyclohexanone distributions and (c) temperature distributions

Velocity magnitude distribution inside the building transported through C_p concept, along with contaminant concentration and indoor temperature at the breathing height (z=1.6 meters) are explained in Figure 3-16.

Lower C_p values at the windows carried higher wind velocity into the building, conforming to the stagnation pressure concept.

At 06:00 hours, a roughly indoor stagnant air distribution due to weak incoming wind from the North-East (around 1.8 m/s) caused a higher cyclohexanone concentration of almost 2.5 mg/m^3 next to the silk printing machines at the breathing height. However, a lower temperature was found at this time due to outdoor weather, where temperature is low during this period.

Relatively high contaminant concentration of 1.8 mg/m^3 was also observed at 09:00 hours due to the same reasons (with an incoming wind in the south-east direction). Low values of wind flow distribution persisted during the morning.

In contrast, a higher non-uniform wind distribution inside the building happened when wind direction was heading into the south-west direction, specifically at 13:00 hours.

During the afternoon, almost-zero contaminant concentration can be observed on the right part of the factory due to large fresh air intake through the windows facing south, especially at 13:00 hours.

Although peak urban velocity happened at 17:00 hours, building position and geometry hindered its transport into the enclosure. While stronger gusts moved through scattered windows, their effect had no major impact. This allowed for a slight spike in contaminant concentration.

Temperature shows no relevant fluctuation during the afternoon.

In this case, building position, urban topography and location of windows had a direct impact on urban air intake by cross-ventilation. In order to analyze local contaminant concentrations around the CSP at different locations, three different cases that varied position have been set, as exemplified in Figure 3-10 (b) and once again in Figure 3-16 (b).

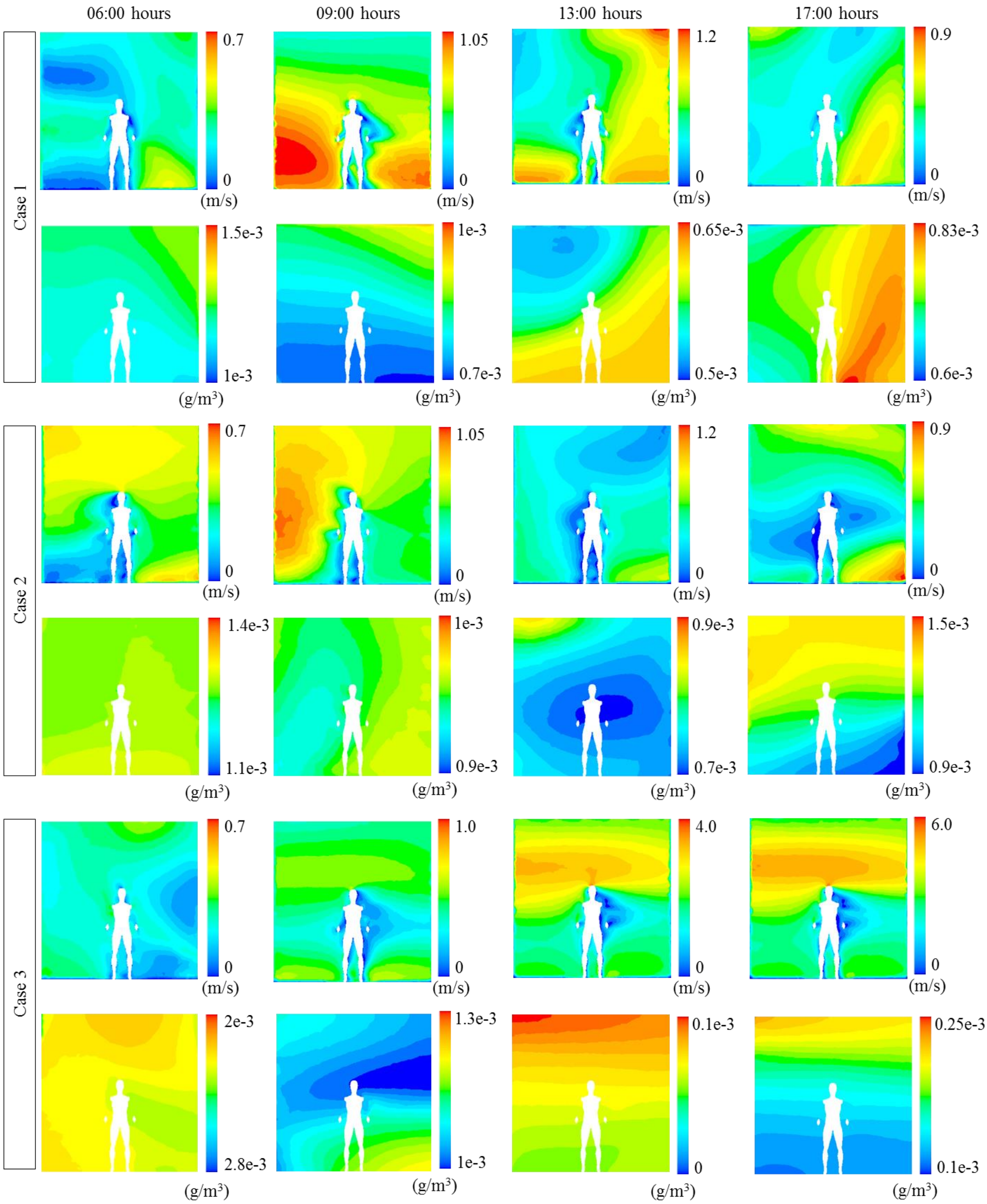

Figure 3-17. Local results of wind velocity magnitude and gas-phase cyclohexanone concentration at the four different times of the day for Cases 1, 2 and 3

In Figure 3-17, all cases at the four different times of the day are presented in terms of velocity magnitude and cyclohexanone concentration distributions to demonstrate de relationship between indoor flow field fluctuation and local contaminant surrounding the human body.

In terms of time-dependency of immediate exposure, lowers values of local velocity allow a higher concentration around the human body. Especially weak wind distribution occurred at 06:00 hours for all cases and contaminant concentration around the CSP was found to be higher. However, positioning of the representative worker also had an impact in local cyclohexanone distribution. Stronger wind velocity distribution diminished the contaminant greatly, especially in Case 3 at 13:00 and 17:00 hours.

In terms of position of the CSP, Case 1 and Case 2, located roughly in the middle of the printing machines and with less access to windows, had a higher contaminant concentration than Case 3. In Case 3, velocity distribution was found to be stronger due to close proximity of the windows, lessening the amount of local contaminant.

As final quantitative results, Table 3-7 presents the results of average wind velocity, average cyclohexanone concentration in the CSP space and the volume of inhaled contaminant calculated by equation (3.6).

It can be confirmed that average cyclohexanone concentration was lower when average wind velocity became high, particularly in Case 3 during the afternoon, close to the windows.

During the morning, Case 3 presented a decrease of 57% in contaminant concentration and a decline of 61% in inhaled volume, while local wind velocity grew by 49% from 06:00 to 09:00 hours.

Overall, it was found that an upsurge in local velocity magnitude decreased local cyclohexanone concentration and the inhaled amount of contaminant in differing proportions. It can also be confirmed that window location, wind direction and the position of the CSP have a direct impact on contaminant distribution and intake into the representative worker.

Table 3-7. Average local wind velocity, average contaminant concentration and inhaled contaminant volume of CSP

Location	**Average wind velocity (m/s)**	**Average contaminant concentration ($\mu g/m^3$)**	**Inhaled volume ($\mu g/s$)**
		Morning Time	
06:00 (Case 1)	0.320	1180	0.096
06:00 (Case 2)	0.435	1280	0.157
06:00 (Case 3)	0.253	2510	0.314
09:00 (Case 1)	0.704	788	0.098
09:00 (Case 2)	0.718	982	0.122
09:00 (Case 3)	0.485	1080	0.126
		Afternoon Time	
13:00 (Case 1)	0.653	583	0.073
13:00 (Case 2)	0.381	766	0.096
13:00 (Case 3)	2.364	75	0.009
17:00 (Case 1)	0.381	748	0.094
17:00 (Case 2)	0.334	1180	0.147
17:00 (Case 3)	3.433	155	0.019

3.4 CONCLUSION

In this study, global flow field, temperature and turbulence were calculated through NWP and then transported to the city urban-built environment through CFD. A quasi-coupling method was used to adjust physical properties between both models.

Wind pressure coefficient distributions along the outside walls of a target building envelope were calculated to transport city urban-built wind flow into a building-indoor environment. Indoor air flow field, local contaminant concentration and inhalation exposure risk of a human worker were calculated by using a CSP and respiratory system model.

Though previous studies have linked NWP to CFD and wind pressure coefficient to IAQ, few have directly connected the global climate scale to the urban-built environment for personal prediction of IAQ and inhalation exposure risk, as it has been proposed in the present research. This becomes especially true in cases where few measured climate data is available. Therefore, this research allows for the implementation of a comprehensive analysis in every case, making this dynamic downscaling technique of utmost importance in regions where wind environmental monitoring data is not sufficiently measured for detailed research.

Fluctuation of cross-ventilation, successfully predicted by wind pressure coefficient, was studied at four times of the day and was found to have significant influence on indoor flow field, which affected non-uniform distributions of contaminant concentration and inhalation exposure risk. Integration of a CSP and respiratory tract system model has provided quantitative information of inhalation exposure risk on building-indoor and mucosal epithelial cell scales.

References

3-1) Murga A, Sano Y, Kawamoto Y, Ito K. "Integrated analysis of numerical weather prediction and computational fluid dynamics for estimating cross-ventilation effects on inhaled air quality inside a factory," *Atmos. Environ.*, vol. 167, pp. 11–22, Oct. 2017.

3-2) Sano Y, Murga A, Kawamoto K, Ito K. "Dynamic downscaling analysis of air quality from urban to human scale: Part 1 Integration of WRF and CFD to predict wind pressure coefficient". *In: Proceedings of Indoor Air 2016*, Belgium, July 3–8, Paper ID: 722, 2016.

3-3) Murga A, Sano Y, Kawamoto K, Ito K. "Dynamic downscaling analysis of air quality from urban to human scale: Part 2 Exposure concentration in a large factory space". *In: Proceedings of Indoor Air 2016*, Belgium, July 3–8, Paper ID: 721, 2016.

3-4) Sano Y, Murga A, Kawamoto K, Ito K. "Integration of numerical weather prediction and computational fluid dynamics to analyze indoor air quality: Part 1, prediction of wind pressure coefficient distributions". *In: Proceedings of Healthy Buildings Asia 2017*, Taiwan, Sept. 2-5, Paper ID: IM 2-2, pp. 222-226, 2017.

3-5) Murga A, Sano Y, Kawamoto K, Ito K. "Integration of numerical weather prediction and computational fluid dynamics to analyze indoor air quality: Part 2, prediction of contaminant concentration and inhalation exposure in a factory". *In: Proceedings of Healthy Buildings Asia 2017,* Taiwan, Sept. 2-5, Paper ID: IM 1-3pp. 57-60, 2017.

3-6) Murga A, Ito K. "Prediction of inhalation exposure in a factory by integrated analysis of numerical weather prediction and computational fluid dynamics". *In: Proceedings of the 29th Conference of the Society of Heating, Air-Conditioning and Sanitary Engineers of Japan, SHASE*, Japan, September 13-15, Paper ID: IS-11, pp. 1-4, 2017.

3-7) Harris LM, and Durran DR. "An idealized comparison of one-way and two-way grid nesting". *Monthly Weather Review*, vol. 138, 2174-2178, 2010.

3-8) Koch SE. “A survey of nested grid techniques and their potential for use within the mass weather prediction model”. *NASA. Technical Memorandum* 87808. 1987.

3-9) Blake DW. “One-way nesting for a primitive equation ocean model”. *In: Proceedings for the ICASE Workshop on Heterogeneous Boundary Conditions.* NASA, MS, USA, 55-59, 1991.

3-10) Srebric J. “Opportunities and challenges for multi-scale modelling of sustainable buildings”. *In: Proceedings of US Frontiers of Engineering Symposium. Report on leading-edge engineering.* National Academy of Engineering, Washington DC, USA, September 19–21, pp. 97–100, 2011.

3-11) Maurer EP, Hidalgo HG. “Utility of daily vs. monthly large-scale climate data: an intercomparison of two statistical downscaling methods”. *Hydrol. Earth Syst. Sci,.*vol. 12, pp. 551–563, 2008.

3-12) The National Center for Atmospheric Research. “Climate change scenarios. What is downscaling?” Taken from https://gisclimatechange.ucar.edu/question/63 on June 26th, 2018.

3-13) Tang J, Niu X, Wang S, Gao H, Wang X, and Wu J. “Statistical downscaling and dynamical downscaling of regional climate in China: Present climate evaluations and future climate projections”, *J. Geophys. Res. Atmos.*, vol. 121, pp. 2110–2129, 2016.

3-14) C. Soriano C, Jorba O, and Baldasano J “One-Way Nesting Versus Two-Way Nesting: Does It Really Make a Difference?” pp. 177–185, 2004.

3-15) Li ZC and Bui TD. “Coupling techniques in boundary-combined methods,” *Eng. Anal. Bound. Elem.*, vol. 10, no. 1, pp. 75–85, 1992.

3-16) Kawamoto Y. “Effect of urbanization on the urban heat island in Fukuoka-Kitakyushu metropolitan area, Japan”. *Procedia Eng.*, vol. 169, pp. 224–231, 2016.

3-17) Thompson G, Field PR, Rasmussen RM, Hall WD. "Explicit forecasts of winter precipitation using an improved bulk microphysics scheme. Part II: implementation of a new snow parameterization". *Mon. Weather Rev.,* vol. 136, pp. 5095–5115, 2008.

3-18) Mlawer EJ, Taubman SJ, Brown PD, Iacono MJ, Clough SA. "Radiative transfer for inhomogeneous atmospheres: RRTM, a validated correlated-k model for the longwave". *J. Geophys. Res. Atmos*., vol. 102, pp. 16663–16682, 1997.

3-19) Chou MD, Suarez MJ, Liang XZ, Yan MMH. "A thermal infrared radiation parameterization for atmospheric studies". *NASA Tech. Memo*. 104606 (19), 68, 2001.

3-20) Janjic Z. "Nonsingular Implementation of the Mellor-yamada Level 2.5 Scheme in the NCEP Meso Model". National Centers for Environmental Prediction, 2002.

3-21) Tewari M, Chen F, Wang W, Dudhia J, LeMone MA, Mitchell K, Ek M, Gayno G, Wegiel J, Cuenca RH. "Implementation and verification of the unified NOAH land surface model in the WRF model". *In: Proceedings of the 20th Conference on Weather Analysis and Forecasting/16th Conference on Numerical Weather Prediction.* American Meteorological Society, Seattle, WA, US. January 11–15, 2004.

3-22) Grell GA, and Dévényi D. "A generalized approach to parameterizing convection combining ensemble and data assimilation techniques," *Geophys. Res. Lett.*, vol. 29, no. 14, pp. 38-1-38–4, Jul., 2002.

3-23) Mathworks. MATLAB Documentation. "Griddata" Taken from (May 1st, 2018): https://www.mathworks.com/help/matlab/ref/griddata.html

3-24) Touma JS. "Dependence of the wind profile power law on stability for various locations", *J. Air Pollution Control Association*, vol. 27, pp. 863-866, 1977.

3-25) Panofsky HA and Dutton JA. "Atmospheric turbulence". *Models and methods for engineering applications*, 1984.

3-26) Hsu SA, Meindl EA, and Gilhousen DB. “Determining the Power-Law Wind-Profile Exponent under Near-Neutral Stability Conditions at Sea”. *J. Appl. Meteor.*, vol. 33, pp. 757–765, 1994.

3-27) Garratt J. “The Atmospheric Boundary Layer”, *Cambridge Atmospheric and Space Science Series.* Cambridge University Press, Cambridge, pp. 444, 1992.

3-28) Tominaga Y, Mochida A, Yoshie R, Kataoka H, Nozu T, Yoshikawa M, and Shirasawa T. “AIJ guidelines for practical applications of CFD to pedestrian wind environment around buildings”, *J. of Wind Eng. and Ind. Aero.*, vol 96, pp. 1749–1761, 2008.

3-29) Mochida A, Tominaga Y, Murakami S, Yoshie R, Ishihara T, Ooka R. “Comparison of various k-εmodel and DSM applied to flow around a high-rise building - report on AIJ cooperative project for CFD prediction of wind environment”, *Wind & Structures 5*, No.2–4, pp. 227–244, 2002.

3-30) Shirasawa T, Tominaga T, Yoshie R, Mochida A, Yoshino H, Kataoka H, and Nozu T, “Development of CFD method for predicting wind environment around a high-rise building Part2: The cross comparison of CFD results using various k- models for the flowfield around a building model with 4:4:1 shape”, *AIJ Journal of Technology and Design*, No.18, pp. 169–174, 2003. (In Japanese)

3-31) Frick S, Huenges E, Jorde K, Jung R, Kabus F, and Kehl K. “Renewable energy: Technology, economics and environment,” *Wind Power Gener.*, pp. 295–348, 2007.

3-32) Ito K, Inthavong K, Kurabuchi T, Ueda T, Endo T, Omori T, Ono H, Kato S, Sakai K, Suwa Y, Matsumoto H, Yoshino H, Zhang W, Tu J. “CFD benchmark tests for indoor environmental problems: Part 1, isothermal/non-isothermal flow in 2D and 3D room model”, *Int. J. Archit. Eng. Technol.* vol. 2, pp. 1–22, 2015.

3-33) Ito K, Inthavong K, Kurabuchi T, Ueda T, Endo T, Omori T, Ono H, Kato S, Sakai K, Suwa Y, Matsumoto H, Yoshino H, Zhang W, Tu J. “CFD benchmark tests for indoor environmental problems: Part 2, cross-ventilation airflows and floor heating systems”, *Int. J. Archit. Eng. Technol*. vol. 2, pp. 23–49, 2015.

3-34) Ito K, Inthavong K, Kurabuchi T, Ueda T, Endo T, Omori T, Ono H, Kato S, Sakai K, Suwa Y, Matsumoto H, Yoshino H, Zhang W, Tu J. “CFD benchmark tests for indoor environmental problems: Part 3, numerical thermal manikins”, *Int. J. Archit. Eng. Technol.* vol. 2, pp. 50–75, 2015.

3-35) Ramponi R, Blocken B. “CFD simulation of cross-ventilation for a generic isolated building: impact of computational parameters”. *Build. Environ.*, vol. 53, pp. 34–48, 2012.

3-36) Perén JI, van Hooff T, Leite BCC, Blocken B. “CFD analysis of cross-ventilation of a generic isolated building with asymmetric opening positions: impact of roof angle and opening location”. *Build. Environ.*, vol. 85, pp. 263–276, 2015.

3-37) Montazeri H, and Blocken B. “CFD simulation of wind-induced pressure coefficients on buildings with and without balconies: Validation and sensitivity analysis,” *Build. Environ.*, vol. 60, pp. 137–149, 2013.

3-38) Phuong NL, and Ito K. “Investigation of flow pattern in upper human airway including oral and nasal inhalation by PIV and CFD”. *Build. Environ.* vol. 94, pp. 504–515, 2015.

3-39) Li C, and Ito K. “Numerical and experimental estimation of convective heat transfer coefficient of human body under strong forced convective flow”. *J.Wind Eng. Ind. Aerodyn.* vol. 126, pp. 107–117, 2014.

3-40) Yoo S-J, and Ito K. “Numerical prediction of tissue dosimetry in respiratory tract using computer simulated person integrated with physiologically based pharmaco-kinetic-computational fluid dynamics hybrid analysis”. *Indoor Built Environ.* (in press): Online First e-publication ahead of print, 2017.

3-41) Kuga K, Ito K, Yoo S-J, Chen W, Wang P, Liao J, Fowles J, Shusterman D, Kumagai K. "First- and second-hand smoke dispersion analysis from e-cigarettes using a computer-simulated person with a respiratory tract model". *Indoor Built Environ.* (in press): Online First e-publication ahead of print, 2017.

[Previously published documents related to this chapter]

[1] Murga A, Sano Y, Kawamoto Y, Ito K. "Integrated analysis of numerical weather prediction and computational fluid dynamics for estimating cross-ventilation effects on inhaled air quality inside a factory," *Atmos. Environ.*, vol. 167, pp. 11–22, Oct. 2017.

[2] Sano Y, Murga A, Kawamoto K, Ito K. "Dynamic downscaling analysis of air quality from urban to human scale: Part 1 Integration of WRF and CFD to predict wind pressure coefficient". *In: Proceedings of Indoor Air 2016*, Belgium, July 3–8, Paper ID: 722, 2016.

[3] Murga A, Sano Y, Kawamoto K, Ito K. "Dynamic downscaling analysis of air quality from urban to human scale: Part 2 Exposure concentration in a large factory space". *In: Proceedings of Indoor Air 2016*, Belgium, July 3–8, Paper ID: 721, 2016.

[4] Sano Y, Murga A, Kawamoto K, Ito K. "Integration of numerical weather prediction and computational fluid dynamics to analyze indoor air quality: Part 1, prediction of wind pressure coefficient distributions". *In: Proceedings of Healthy Buildings Asia 2017*, Taiwan, Sept. 2-5, Paper ID: IM 2-2, pp. 222-226, 2017.

[5] Murga A, Sano Y, Kawamoto K, Ito K. "Integration of numerical weather prediction and computational fluid dynamics to analyze indoor air quality: Part 2, prediction of contaminant concentration and inhalation exposure in a factory". *In: Proceedings of Healthy Buildings Asia 2017*, Taiwan, Sept. 2-5, Paper ID: IM 1-3pp. 57-60, 2017.

[6] Murga A, Ito K. “Prediction of inhalation exposure in a factory by integrated analysis of numerical weather prediction and computational fluid dynamics”. *In: Proceedings of the 29th Conference of the Society of Heating, Air-Conditioning and Sanitary Engineers of Japan, SHASE*, Japan, September 13-15, Paper ID: IS-11, pp. 1-4, 2017.

FULL NWP-CFD TRANSIENT APPROACH

4.1 FOREWORD

While a direct dynamic downscaling approach is the most straightforward procedure in terms of steady-state, it can only be applied for immediate contaminant concentration and inhalation risk, as specified by the times selected in Chapter 3 (06:00, 09:00, 13:00 and 17:00 hours). However, in most cases, the analysis of inhalation exposure risk on a person, especially on a factory worker that spends at least eight hours in the workplace, requires a long-term approach.

Against this reasoning, this Chapter describes the full NWP–CFD approach for a transient solution over a period of eight working hours (from 08:00 to 17:00 hours with a one-hour interlude). At this time, only representative NWP meteorological results have been transported to an urban-built CFD domain and consequently to a building-indoor environment with an integrated CSP.

The same embedded two-way nesting technique has been applied for the NWP domains. Furthermore, the change of cross-ventilation has been analyzed through C_p and wind direction variability during the day. This type of full NWP–CFD transient approach has been proven to be of higher accuracy for long-term prediction. However, while a pioneering way of transporting flow field from the global to the urban-built scale for an IAQ and inhalation exposure risk analysis, it requires higher computational resources and time, which might not be available at every opportunity.

4.2 METHODOLOGY OF FULL NWP-CFD TRANSIENT APPROACH

The full NWP-CFD transient approach[4-1] explained in this chapter transports flow field, turbulence, temperature and pollutant through six domains. The first four domains have been analyzed through NWP (*NWP1~NWP4*) and denote a target area of several thousands of square kilometers (*NWP1*) to an area covering tens of square kilometers with the target building at the center (*NWP4*). *NWP2* and *NWP3* are nested sub-domains that span hundreds of square kilometers.

These domains have previously been explained in Chapter 3 and have remained the same for this part of the study. In this case, representative *NWP4* results have been treated and input as boundary conditions for the previously established domain *CFD2* and *CFD1* has been omitted.

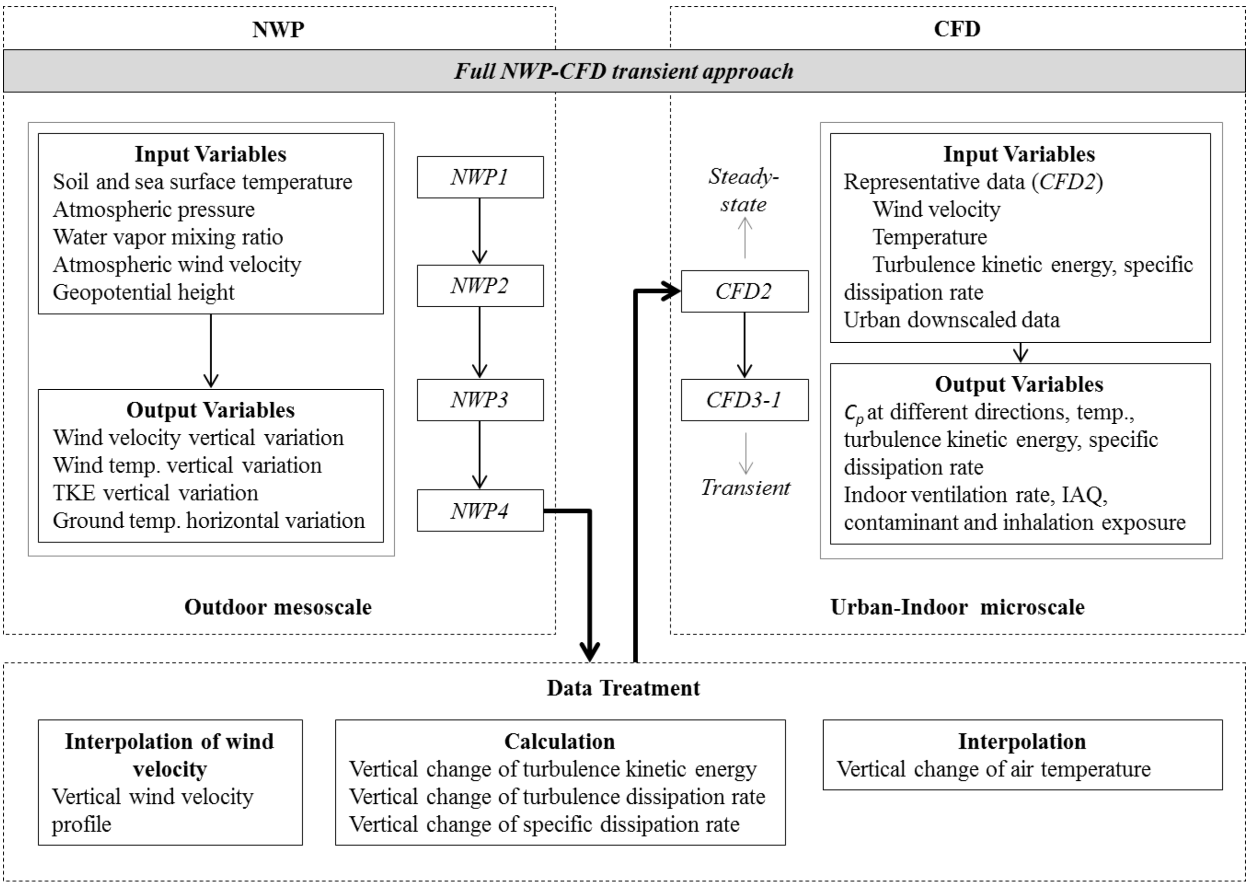

Figure 4-1. Flowchart of full NWP–CFD transient approach

Wind pressure coefficient (C_p) has been calculated at the walls of the building envelope in *CFD2* under steady-state at different times of the day according fluctuating wind direction to generate indoor transient flow field. A modified factory domain *CFD3-1* with an integrated CSP has been used to predict transient indoor flow field, long-term contaminant concentration and inhalation exposure risk. In this study, a long-term period has been defined as eight work working hours, from 08:00 to 17:00 hours with a one-hour interlude. Figure 4-1 describes the outline for the procedure of this approach.

4.2.1 NWP Dynamic Downscaling

As stated previously, the NWP analysis of this approach has not varied and will therefore not be explained in detail as it has already been described in section 3.2.1.

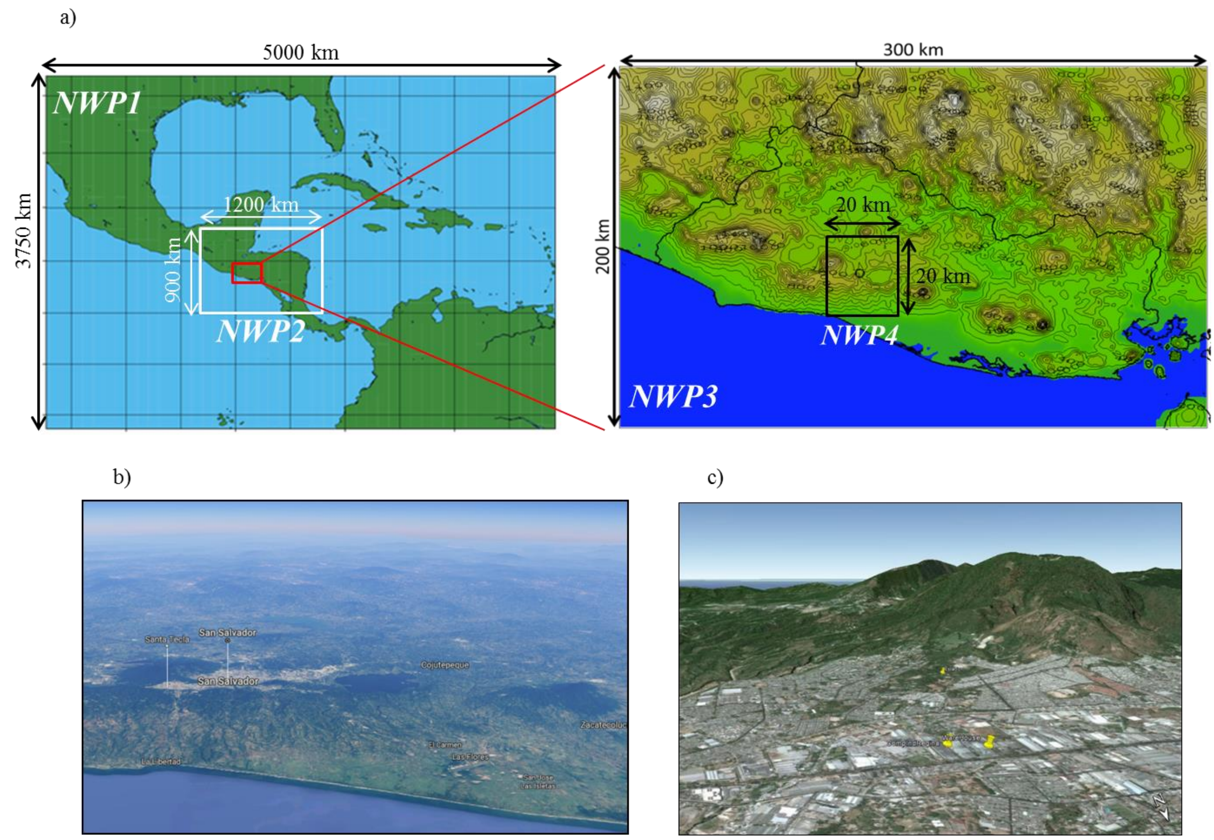

Figure 4-2. Further recollection of (a) NWP domains and (b) Topographical terrain of target area

It has been established that the *NWP1* and the subsequent three nested domains (*NWP2~NWP4*) encase the country of El Salvador, located in Central America between latitudes 13° and 15° N and longitudes 87° and 91°. Although dimensions have been previously explained, Figure 4-2 and Table 4-1 refresh the memory of said domains' designs and numerical conditions and should be therefore acknowledged.

This part of the study was conducted during climatologically representative summer days during April 2012, from April 1st to April 30th during which peak meteorologically conditions and El Niño-Southern Oscillation (ENSO) have not been considered.

Table 4-1. Numerical conditions for domains *NWP1* to *NWP4*

Component	**Condition and Scheme**
Cloud microphysics	Thompson scheme[4-2]
Long-wave radiation	RRTM scheme[4-3]
Short-wave radiation	Goddard scheme[4-4]
Surface layer	Monin–Obukhov scheme[4-5]
Ground surface	Noah Land–Surface model[4-6]
Atmospheric boundary layer	Mellor–Yamada–Janjic TKE scheme[4-5]
Cumulus parameterization	Grell 3D ensemble scheme (*for NWP1*)[4-7]

Further explanation of geometry and mesh design as well as detailed boundary and other numerical conditions[4-8] have already been explained in section 3.2.1. Time integration was performed during 30 days and the hourly output results of average wind velocities (three velocity components: *u*, *v* and *w*), wind direction, turbulence kinetic energy, air and surface temperature (ensemble averaged over a month) were treated and used to set as representative data for the inflow boundary conditions of domain *CFD2*.

4.2.2 NWP–CFD Data Treatment

Due to the difference of modelling mechanisms and physical properties between NWP and CFD, data was pre-treated in order to input representative results of *NWP4* as boundary conditions of *CFD2*.

In this section, the treatment of variables is described. This procedure is different from the one described in section 3.2.2 and is thus explained in detail.

4.2.2.1 Interpolation of Variables

As a first step, treatment process has been simplified and mesoscale data of wind velocity at every hour has been assumed 1 m/s. This was adopted to save numerical processing time. *NWP4*-obtained data of temperature has been maintained. Further adjustment of spatial distribution is described below.

- *Horizontal Interpolation*

In contrast with Chapter 3, 0^{th} order interpolation (nearest neighbor) has been applied to wind velocity, turbulence kinetic energy, turbulence dissipation rate, specific dissipation rate, and air temperature. This mathematical process applies a continuous step function for data over time/distance. Figure 4-3 describes this procedure.

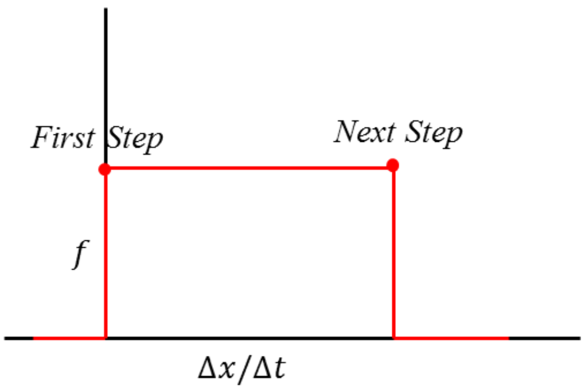

Figure 4-3. Graphical explanation of 0^{th} order interpolation.

- *Vertical Interpolation*

For vertical data spacing above 13 meters (first grid-point of *NWP4* data results), wind velocity, turbulence kinetic energy, turbulence dissipation rate, specific dissipation rate, and air temperature were treated through 0^{th} order interpolation (above explained procedure).

Vertical special distribution of data below 13 meters directly affects flow paths and flow field transport and data was carefully treated. Consequently, wind temperature below this height was linearly interpolated from ground surface to first-grid point for a rough approximation of vertical profile.

Further vertical treatment of data below 13 meters is explained in the following sections (4.2.2.2 and 4.2.2.3).

4.2.2.2 Vertical interpolation of wind velocity

To model wind-speed at the viscous boundary sublayer, extrapolation below 13 has been applied for a vertical wind profile that uses ¼ power law, extensively explained in the previous Chapter. It can be defined by equation (4.1):

$$U_2 = U_1 \left(\frac{z_2}{z_1} \right)^P \qquad (4.1)$$

Where U_1 is the wind velocity at a known height, in this case, the first grid-point of *NWP4* results and z_1 is the corresponding height of 13 meters. z_2 is the corresponding height of velocity U_2, which has been interpolated every 0.5 meters until reaching ground level.

P is a function of both the atmpospheric stability in the layer over which P is determined and the underlying surface characteristics. This research assumes $P = 0.25$, for a ¼ power law for vertical wind profile.

4.2.2.3 Calculation of Variables

Further vertical treatment of data below 13 meters was performed. Turbulence kinetic energy (*TKE*), turbulence dissipation rate (ε) and specific dissipation rate (ω) have been calculated under the assumption that U_1 = 1 m/s, according to the findings made by Tominaga et al[4-9~4-11].

Turbulence kinetic energy was calculated through equation (4.2) as a function of height.

$$TKE_z = \left[0.018\left(\frac{z_2}{z_1} \right) + 0.015 \right] U_1^2 \qquad (4.2)$$

Where z_2 is the height from ground surface, spaced every 0.5 meters, z_1 is the lowest grid height corresponding to U_1^2, the square wind velocity at representative height (13 meters).

Turbulence dissipation rate ε and specific dissipation rate ω were calculated through equations (4.3) and (4.4) as functions of height also under the assumption that U_1 = 1 m/s. The constant C_μ has been set as 0.09.

$$\varepsilon_z = \frac{C_\mu TKE_z^{1.5} U_1}{4(C_\mu TKE_z)^{0.5} z_1^{0.25} z_2^{0.75}} \qquad (4.3)$$

$$\omega_z = \frac{\varepsilon_z}{TKE_z} \qquad (4.4)$$

Treated data was input into *CFD2* as boundary conditions for analysis of C_p variability based on 16 different wind directions, as explained in section 4.2.3.

4.2.3 Variability analysis of diurnal wind pressure coefficient (steady-state)

This section describes the procedure to calculate C_p daily variation based on a 16-direction analysis. As a first step, 16 cases of prevailing daily wind have been assumed according to cardinal directions (N, S, E and W), intercardinal and secondary-intercardinal points, as explained in Figure 4-4.

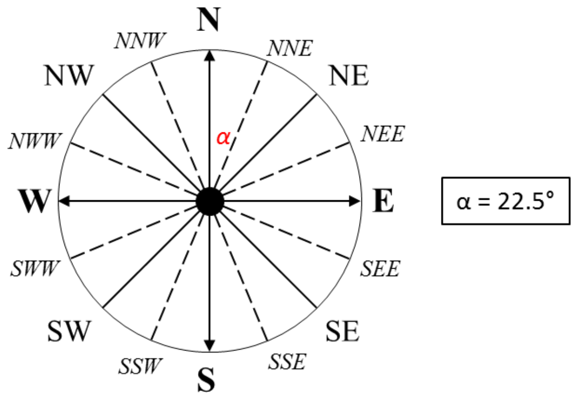

Figure 4-4. 16 directions assumed: cardinal, intercardinal and secondary-cardinal

CFD2 is once again briefly described. It covered a city-urban area of 200 square meters based on real elevation data obtained through ALOS using AW3D high-resolution map. Resolution of elevation points was of 5 meters.

Domain height was roughly 100 meters above ground level and the factory building was set at the center of the domain.

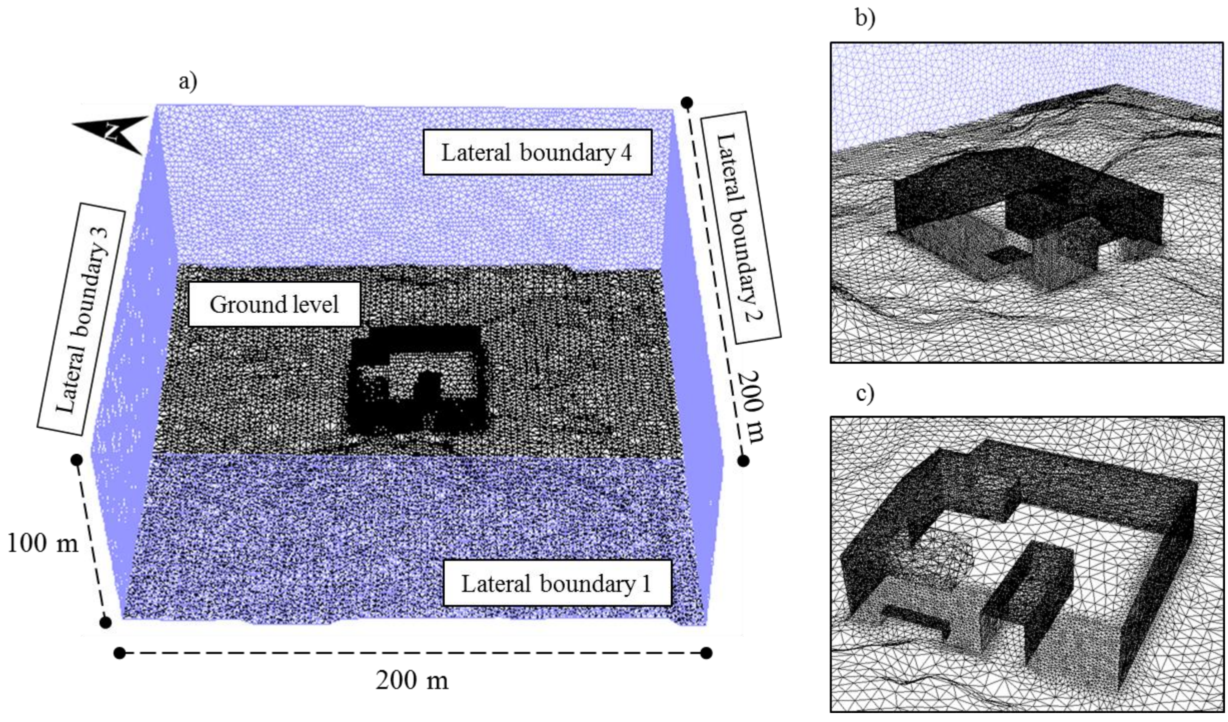

Figure 4-5 Mesh design (a) of *CFD2* domain, (b) of ground near factory (c) of factory

This region was discretized by an unstructured tetrahedral mesh of 2.45 million elements and grid cell size ranged from 5 meters at the boundaries to a few centimeters at the windows of the building envelope. ANSYS/ICEM 16.0 was also used for its design.

Figure 4-5 (a) shows the entire urban domain and Figure 4-5 (b) shows real terrain of this region.

The SST *k-ω* model was used to simulate turbulence in *CFD2* to maintain consistency with previous. Summarized numerical conditions are presented in Table 4-2; further details can be read in section 3.2.3.1.

Table 4-2. Numerical conditions for domain *CFD2*

Component	**Condition**
Turbulence Model	SST Type *k-ω* model (3D calculation)
Mesh	2.45 Million Mesh (unstructured, tetrahedral)
Scheme	Algorithm: SIMPLE Convection Term: Second Order Upwind
Inflow Boundary	U_{in}, T_{in}, k_{in}, ω_{in} = *NWP4* treated data
Outflow Boundary	U_{out} ,T_{out}, k_{out} = Free Slip
Wall Boundary	Velocity: No Slip Temperature: T_{srf} = *NWP4* data (point profile)

C_p distributions along the outside walls of the target building were calculated using equation (4.5):

$$C_p = \frac{P_{wall} - p}{\frac{1}{2}\rho v^2} \tag{4.5}$$

Where $P_{wall} - p$ represents the pressure difference between the outside wall and a determined representative point, ρ is the air density and v is the square wind velocity at the openings. In this study, 42 windows of dimensions 1.5 m$\times$2.0 m were fixed as building openings.

Of these 16 cases, those which direction occurred during the day according to *NWP4* results were chosen and further treated.

As the second step, an azimuth interpolation was performed to correct hourly azimuth in the calculation by using the following equation (4.6):

$$P_A = P_1 \times \left(\frac{b}{22.5} \right) + P_2 \times \left(\frac{a}{22.5} \right) \quad (4.6)$$

Where P_A is the corrected pressure including azimuth, P_1 is the static pressure at the current hour, P_2 is static pressure from previous hour, a is the product of integer division between angle of incidence and total degrees and b is $22.5 - a$.

Correction equations for, *TKE*, ε and ω are given by expressions (4.7), (4.8) and (4.9):

$$TKE_A = TKE_1 \times \left(\frac{b}{22.5} \right) + TKE_2 \times \left(\frac{a}{22.5} \right) \quad (4.7)$$

$$\varepsilon_A = \varepsilon_1 \times \left(\frac{b}{22.5} \right) + \varepsilon_2 \times \left(\frac{a}{22.5} \right) \quad (4.8)$$

$$\omega_A = \omega_1 \times \left(\frac{b}{22.5} \right) + \omega_2 \times \left(\frac{a}{22.5} \right) \quad (4.9)$$

As the third and final step, corrected results of pressure, *TKE*, ε and ω were multiplied by representative mesoscale velocity from *NWP4* results to correct assumed mesoscale velocity = 1 m/s through the following equations:

$$P_c = P \times v_r^2 \tag{4.10}$$

$$TKE_c = TKE \times v_r^2 \tag{4.11}$$

$$\varepsilon_c = \varepsilon \times \frac{1}{v_r^3} \tag{4.12}$$

$$\omega_c = \omega \times \frac{1}{v_r^3} \tag{4.13}$$

Where $P_c, TKE_c, \varepsilon_c,$ and ω_c are the corrected variables, v_r is the ratio of local velocity (NWP4-obtained data) and representative mesoscale velocity = 1 m/s, [-]. $P, TKE, \varepsilon,$ and ω are results with assumed velocity =1 m/s. These data was used for the building-indoor scale transient analysis, as explained in the next section.

4.2.4 Transient indoor air quality analysis

Based on the above analysis, urban steady-state pressure, turbulence and temperature were transported to the building-indoor environment *CFD3-1* for a transient analysis by way of a User Defined Function (UDF), called a macro.

In Fluent software, a macro is a journal file in a manner of record/playback function. Here, a DEFINE_PROFILE macro that defines hourly steady-state boundary conditions stated in the previous section has been applied. A transient calculation from 08:00 to 17:00 hours has been performed.

The following equation to interpolate hourly data has been applied inside the macro:

$$\phi_t = \phi_1 \times \left(\frac{t_2 - t}{3600} \right) + \phi_2 \times \left(\frac{t - t_1}{3600} \right) \tag{4.14}$$

Where ϕ_t is the parameter at current time, ϕ_1 is the parameter value at the previous hour, ϕ_2 is the parameter value at present hour, t_2 is the present hour [s], t_1 is the previous hour [s] and t is current time [s].

Previous domain *CFD3*, the target factory, has been modified with an integrated CSP to analyze indoor IAQ and inhalation exposure risk.

Figure 4-6 (a) shows the entire new *CFD3-1* domain with the integrated CSP, Figure 4-6 (b) describes the geometry of the CSP inside the factory and Figure 4-6 (c) explains the mesh design near the CSP with a finer mesh around the human body.

To improve calculation accuracy, five layers of prism mesh with height 0.5 mm have been modeled around the CSP (Figure 4-6 (d)).

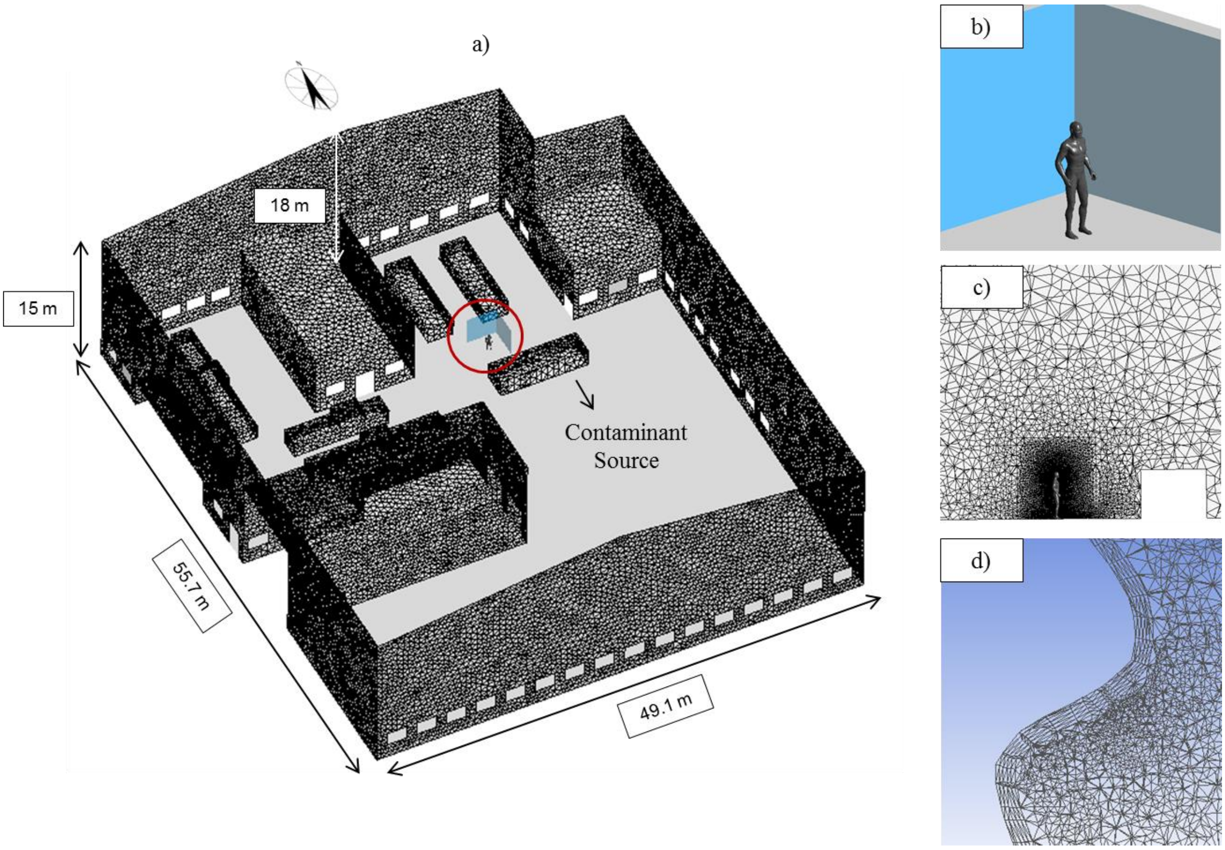

Figure 4-6 Design of (a) mesh and geometry of *CFD3-1*, (b) CSP geometry inside factory, (c) mesh near CSP inside factory and (d) prims layers

Dimensions of this modified domain were kept the same: 55.7 m × 49.1 m with a gabled roof design. Total space was discretized by an unstructured tetrahedral mesh of 4.92 million elements. Minimum grid size was roughly one centimeter at the windows and less than one millimeter at the nostrils. ANSYS/ICEM was used to create the geometry. For the contaminant, the same six silk printing machines were set as indoor-only sources.

Cyclohexanone (gas phase) was set as the target chemical with generation rate of 8.54 g/s from 08:00 to 12:00 and from 13:00 to 17:00 hours while having zero generation rate from 12:00 to 13:00 hours (interlude). A macro (UDF) was also input for this calculation.

The same passive contaminant transport was applied. Cyclohexanone adsorption was disregarded at the indoor wall surfaces through a gradient zero-type condition. No ambient air pollution was considered.

The SST k-ω model was to analyze the turbulence inside the building to keep consistency with the other domains. The S2S radiation model was adopted for long-wave radiative heat transfer. Solar heat load distributions were calculated at the external wall surfaces to consider short-wave radiative heat transfer.

Numerical boundary conditions are explained in Table 4-4; further settings have already been explained in section 3.2.3.3. A time step of 1 minute was used and analysis was conducted for 9 hours: 8-hour occupational period with a one-hour interlude, standard agreement for a one-day labor for factory workers in El Salvador.

Through this technique, transient diurnal results of ventilation rate, contaminant concentration in the indoor environment and at the nares of the CSP for an inhalation risk exposure assessment were obtained.

Table 4-3. Numerical conditions of domain *CFD3-1*

Component	**Condition**
Turbulence Model	SST *k-ω* Model
Mesh	4.92 million mesh (Unstructured)
Scheme	Algorithm: SIMPLE; Convection Term: 2^{nd} Order Upwind
Inflow Boundary	P_{in}, T_{in}, k_{in}, ω_{in} = *CFD2* data
Human surface (skin)	Velocity, k_{wall}: No slip
Human breathing	U_{in} = 0.478 m/s (constant inhalation) Length Scale: 0.001 Turbulence Intensity: 10% Scalar type: Passive contaminant $C_{inhaled}$: Gradient zero condition
Outflow Boundary	P_{out}, T_{out}, k_{out}, ω_{out} = *CFD2* data
Heat Source	333.15K (Kinzel), 338.15K (Sakurai)
Radiation	View Factor: Hemicube Method Solar Load: Solar-Ray Tracing
Scalar	Cyclohexanone, Scalar Type: Passive Contaminant
Wall Boundary	Velocity: No Slip

4.3 RESULTS AND DISCUSSION

This section presents the results of the full NWP–CFD transient approach. NWP results have been averaged over a 30-day period while CFD results are divided into steady-state results for C_p diurnal variability analysis and transient results for indoor ventilation rate, IAQ analysis and inhalation exposure risk.

Table 4-4 summarizes mesoscale results in terms of wind velocity and wind direction (secondary-intercardinal description and azimuth) over a 24-hour period, which have been used for calculation of diurnal C_p variability.

During the morning, prevailing wind direction from North could be appreciated and velocity magnitude was found to be lower, especially at noon.

Wind direction from South during the afternoon allowed for higher wind velocity, particularly at 16:00 hours. During night time wind direction was continuous from NNW.

The representative results of wind velocity and direction that were used during C_p calculation have been encased in a black frame in Table 4-4. Other mesoscale results have already been presented in section 3.3.1.

4.3.1 NWP Dynamic Downscaling Results

Table 4-4. *NWP4* results of wind velocity and wind direction

Hour	Direction	Azimuth	Velocity Magnitude (m/s)
01:00	NNW	60.2	5.94
02:00	NNW	60.2	6.18
03:00	NNW	62.8	6.71
04:00	NNW	64.8	7.35
05:00	NNW	63	6.49
06:00	NNW	58.7	5.86
07:00	NNW	59.7	5.16
08:00	NNW	69.1	6.08
09:00	N	91.2	2.98
10:00	NNE	107.9	2.53
11:00	NE	128.3	1.96
12:00	ENE	152.7	0.52
13:00	SSE	250.6	2.29
14:00	S	272.1	6.63
15:00	S	274.2	8.30
16:00	S	278.9	9.78
17:00	S	279.8	8.94
18:00	S	279.5	5.99
19:00	SSW	293.7	2.80
20:00	NWW	32.1	1.51
21:00	NW	47.3	1.96
22:00	NNW	61.7	3.83
23:00	NNW	64.9	5.72
24:00	NNW	60.7	5.28

4.3.2 Wind pressure coefficient variability results

4.3.2.1 C_p variability results for v=1 m/s

Figure 4-7 shows results of 16-cases steady-state analysis assuming mesoscale wind velocity v=1 m/s. Wind directions that occurred during the evaluated time have been marked in red.

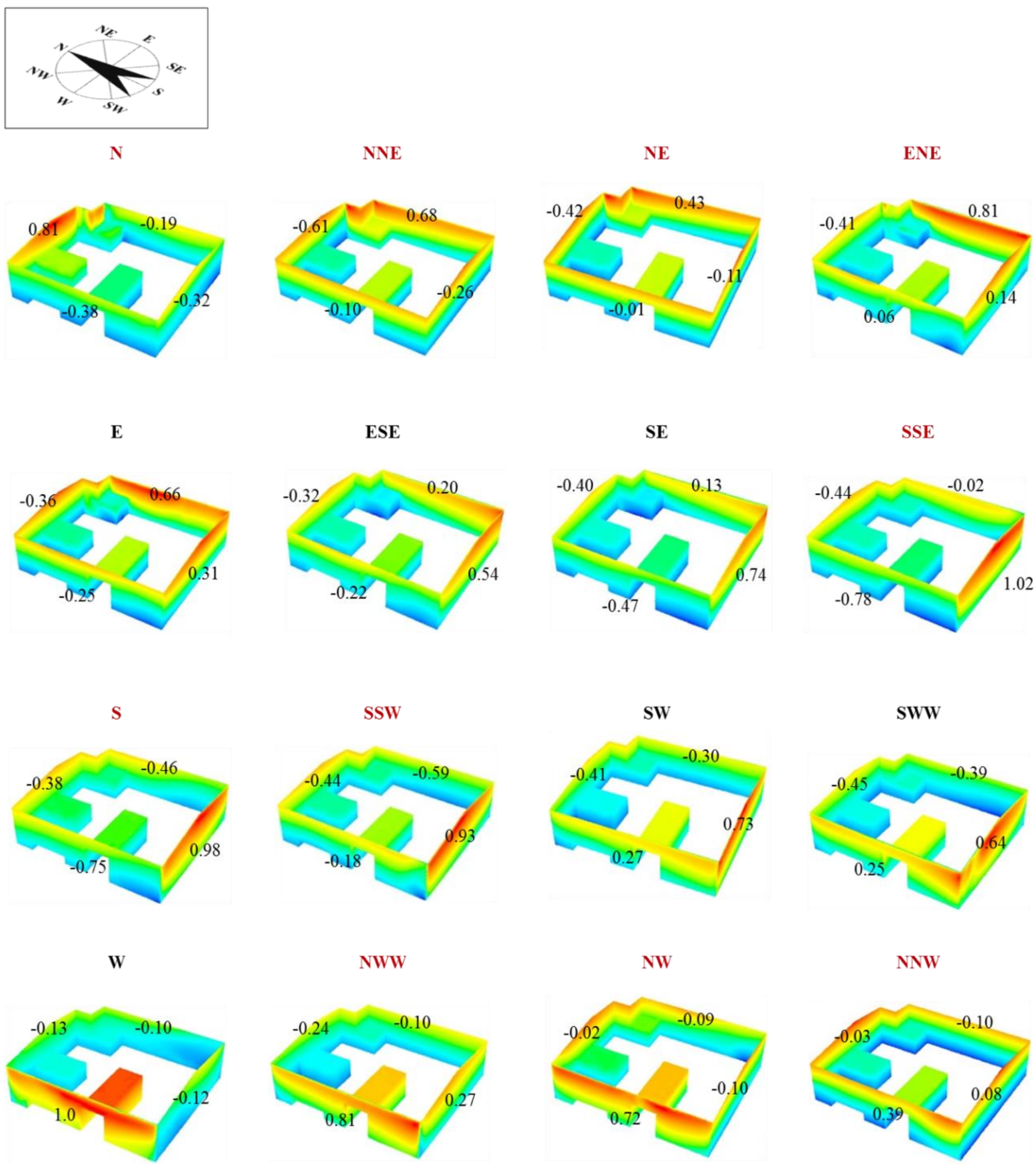

Figure 4-7 C_p steady-state results at the walls of the building envelope for every prevailing wind direction at each hour (mesoscale v=1 m/s)

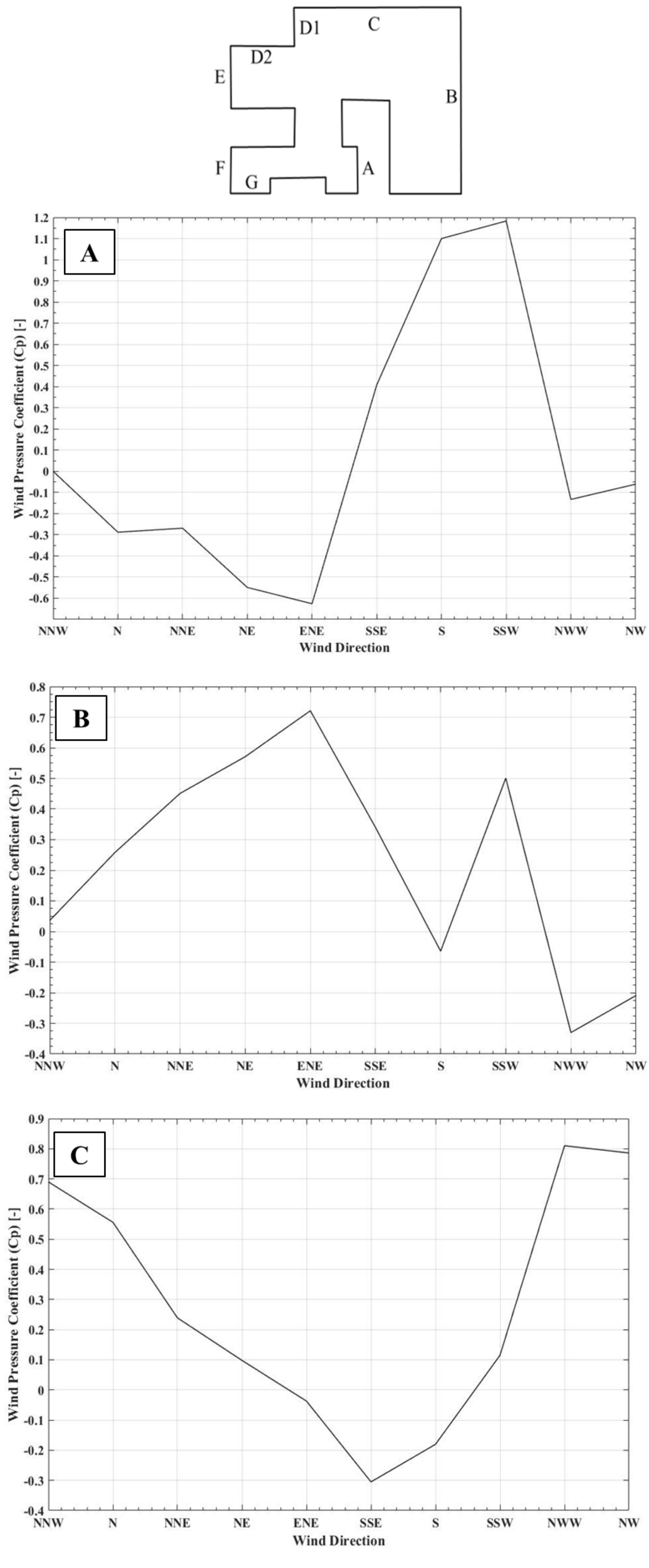

Figure 4-8. C_p variability (average) vs. diurnal wind direction for walls A, B and C

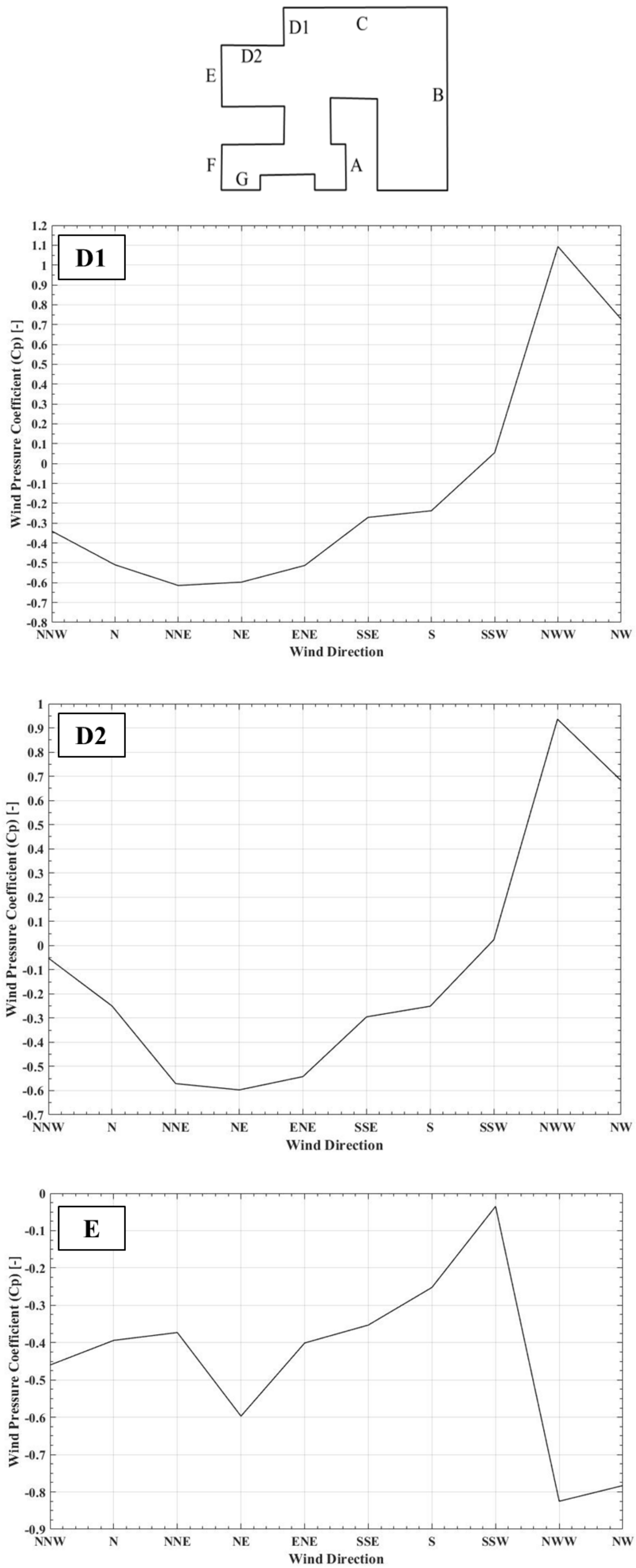

Figure 4-9. C_p variability (average) vs. diurnal wind direction for walls D1, D2 and E

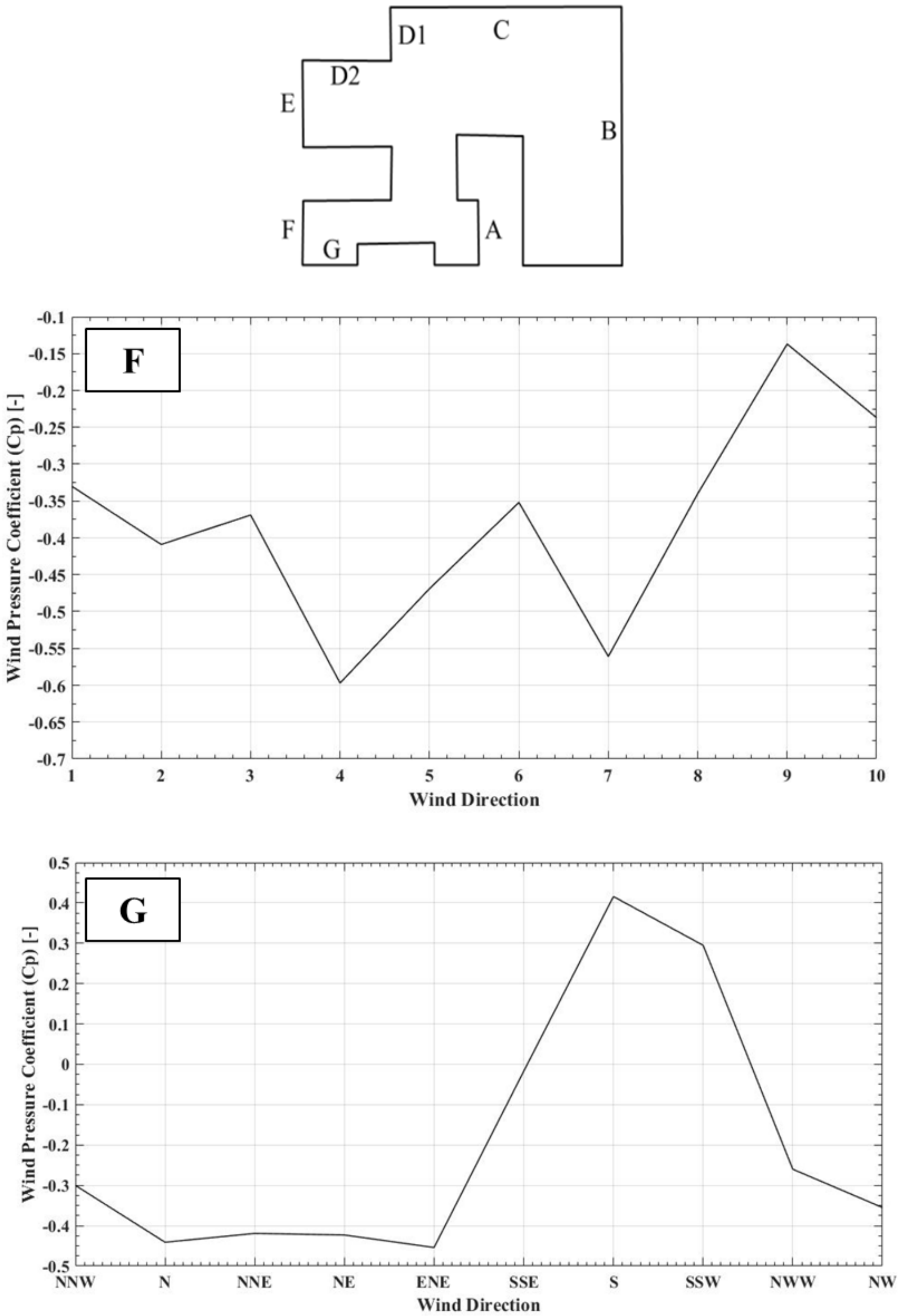

Figure 4-10. C_p variability (average) vs. diurnal wind direction for walls F and G

According to the results, the maximum positives values of C_p were generally generated when wind directions where between 0 and 90° to the end wall. No tendency was observed based on different wind directions.

4.3.2.2 C_p variability results for real mesoscale representative velocity

Figure 4-8, Figure 4-9 and Figure 4-10 show C_p averaged results for every wall in terms of wind direction. It can be confirmed that C_p varied greatly depending on wind direction. These results prove the viability of using the described procedure to calculate diurnal variability of wind pressure coefficient. Nonetheless, C_p results on wall A were slightly higher than 1.

4.3.3 Transient indoor air quality results

The above summarized C_p daily variation generated indoor transient conditions examined from 08:00 to 17:00 hours. Figure 4-11 shows results of ventilation rate in terms of air change per hour (ACH) where high time-dependent variation can be seen. ACH was found to be highest during the afternoon, specifically at 16:00, which is consistent with city-urban results, given the high urban wind velocity ensued at that time.

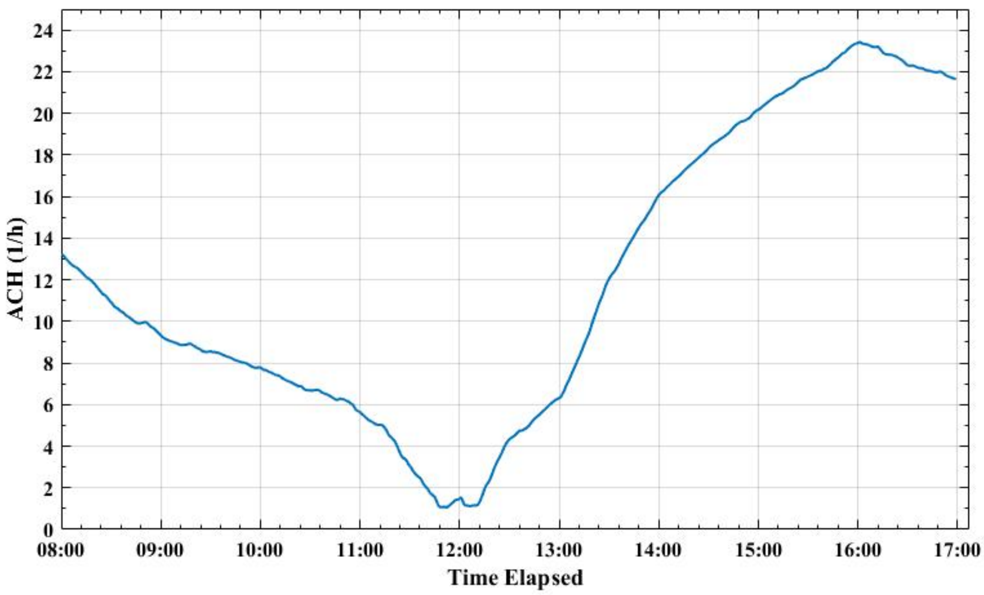

Figure 4-11. Transient factory ACH results

Finally, Figure 4-12 shows results of IAQ analysis and inhalation exposure risk in terms of time and wind direction. Contaminant concentration inside the factory volume, marked in green, was found to change diurnally according to ACH results.

The working schedule showed a diminishment in contaminant during rest-hour that quickly increased when generation rate enlarged. Higher contaminant concentration in both cases was found during morning period when ACH was particularly low and reached peak value around noon when lowest ACH values happened. This trend confirms the direct relationship between ventilation rate and contaminant concentration.

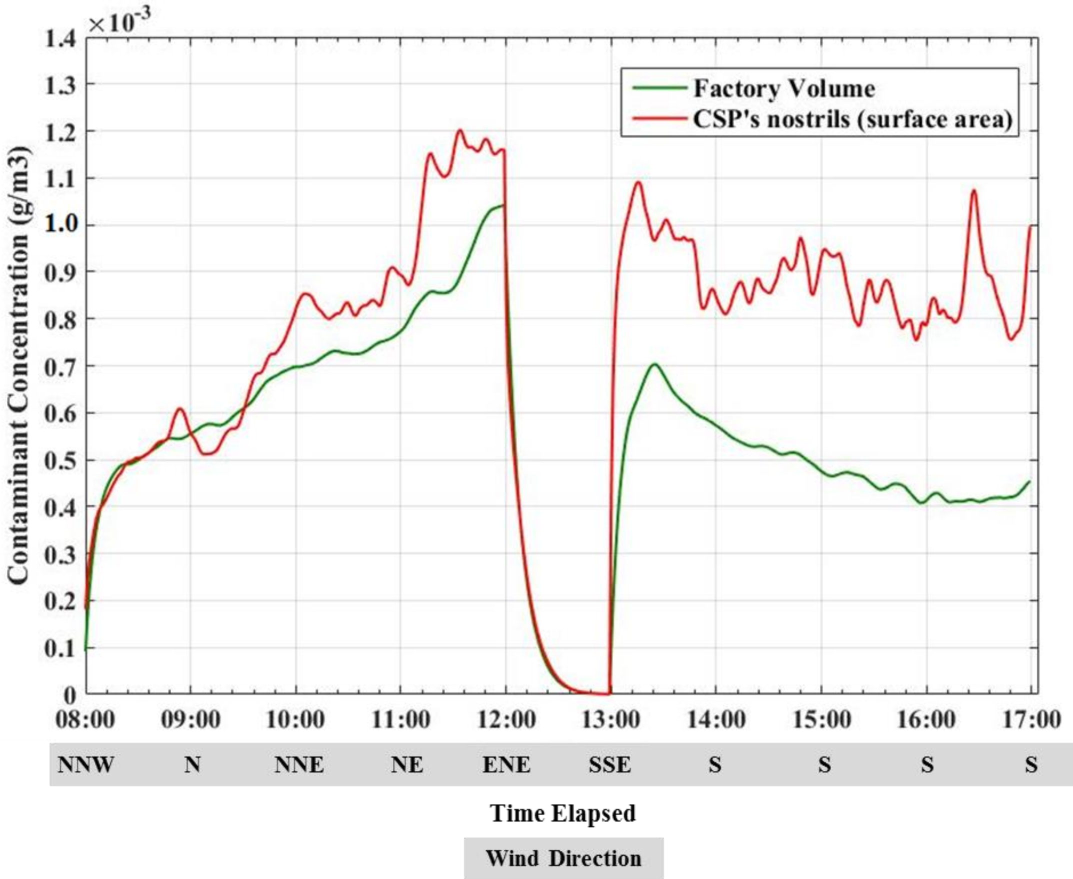

Figure 4-12. Transient results of contaminant concentration inside the factory and at the nostrils of the CSP

Results of indoor contaminant concentration are marked in green and inhalation exposure risk was summarized as the contaminant concentration at the nares of the CSP.

4.4 CONCLUSION

In this Chapter, steady-state diurnal variation of wind pressure coefficient distributions along the outside walls of a target building was analyzed and used to transport city-urban flow field and to the building-indoor environment. Corresponding results showed that variability in wind direction and city-urban wind flow has a direct impact wind pressure coefficient variation and thus, ventilation rate. ACH variation had a direct impact in building contaminant concentration and inhalation exposure risk.

In terms of the building-indoor transient analysis, a CSP was integrated to the factory model to analyze inhalation exposure risk through area-weighted average at the nares of the human body. Indoor contaminant behavior was also analyzed and found that contaminant is always present with constant generation rate but only a small residue persists during the interlude.

Although a straight-forward and accurate approach; one of the demerits of this full type of analysis is the computational resources and time needed to perform a transient CFD calculation during eight hours for an occupational application. This may present a considerable obstacle in some cases. From this point of view, a hybrid NWP–CFD–MNM approached that consumes fewer resources and computational time has been proposed in the next Chapter.

References

4-1) Murga A, Ito K. "Integrated analysis of numerical weather prediction and computational fluid dynamics for estimating cross-ventilation effects on inhaled air quality inside a factory". *In: Proceedings of RoomVent Ventilation 2018,* June 2-5, Finland, Paper ID: 66.

4-2) Thompson G, Field PR, Rasmussen RM, Hall WD. "Explicit forecasts of winter precipitation using an improved bulk microphysics scheme. Part II: implementation of a new snow parameterization". *Mon. Weather Rev.,* vol. 136, pp. 5095–5115, 2008.

4-3) Mlawer EJ, Taubman SJ, Brown PD, Iacono MJ, Clough SA. "Radiative transfer for inhomogeneous atmospheres: RRTM, a validated correlated-k model for the longwave". *J. Geophys. Res. Atmos*., vol. 102, pp. 16663–16682, 1997.

4-4) Chou MD, Suarez MJ, Liang XZ, Yan MMH. "A thermal infrared radiation parameterization for atmospheric studies". *NASA Tech. Memo*. 104606 (19), 68, 2001.

4-5) Janjic Z. "Nonsingular Implementation of the Mellor-yamada Level 2.5 Scheme in the NCEP Meso Model". National Centers for Environmental Prediction, 2002.

4-6) Tewari M, Chen F, Wang W, Dudhia J, LeMone MA, Mitchell K, Ek M, Gayno G, Wegiel J, Cuenca RH. "Implementation and verification of the unified NOAH land surface model in the WRF model". *In: Proceedings of the 20th Conference on Weather Analysis and Forecasting/16th Conference on Numerical Weather Prediction.* American Meteorological Society, Seattle, WA, US. January 11–15, 2004.

4-7) Grell GA, and Dévényi D. "A generalized approach to parameterizing convection combining ensemble and data assimilation techniques," *Geophys. Res. Lett.*, vol. 29, no. 14, pp. 38-1-38–4, Jul., 2002.

4-8) Kawamoto Y. "Effect of urbanization on the urban heat island in Fukuoka-Kitakyushu metropolitan area, Japan". *Procedia Eng.*, vol. 169, pp. 224–231, 2016.

4-9) Tominaga Y, Mochida A, Yoshie R, Kataoka H, Nozu T, Yoshikawa M, and Shirasawa T. "AIJ guidelines for practical applications of CFD to pedestrian wind environment around buildings", *J. of Wind Eng. and Ind. Aero.*, vol 96, pp. 1749–1761, 2008.

4-10) Mochida A, Tominaga Y, Murakami S, Yoshie R, Ishihara T, Ooka R. "Comparison of various k-εmodel and DSM applied to flow around a high-rise building - report on AIJ cooperative project for CFD prediction of wind environment", *Wind & Structures 5*, No.2–4, pp. 227–244, 2002.

4-11) Shirasawa T, Tominaga T, Yoshie R, Mochida A, Yoshino H, Kataoka H, and Nozu T, "Development of CFD method for predicting wind environment around a high-rise building Part2: The cross comparison of CFD results using various k- models for the flowfield around a building model with 4:4:1 shape", *AIJ Journal of Technology and Design*, No.18, pp. 169–174, 2003. (In Japanese)

[Previously published documents related to this chapter]

[1] Murga A, Ito K. "Integrated analysis of numerical weather prediction and computational fluid dynamics for estimating cross-ventilation effects on inhaled air quality inside a factory". *In: Proceedings of RoomVent Ventilation 2018,* June 2-5, Finland, Paper ID: 66.

HYBRID NWP–CFD–MNM TRANSIENT APPROACH

5.1 FOREWORD

As it was expressed in Chapter 4, although convenient in terms of accuracy, one of the disadvantages of a full NWP–CFD transient approach is the need for extensive computational resources and time needed for a long-term calculation in the case of occupational applications.

From this point of view, this Chapter includes the use of multizone network modelling (MNM) to evaluate transient IAQ. This type of modeling allows for a faster calculation because it only supplies average features of airflow and contaminant transport inside the building by way of interconnected zones. It also allows a connection to the outdoor environment through flow paths to create pressure differences[5-1~5-3].

Therefore, this Chapter describes a hybrid NWP–CFD–MNM transient approach to analyze a time-dependent solution over eight working-hours (from 08:00 to 17:00 hours with a one-hour interlude). Only representative NWP meteorological conditions have been transported to a city-urban CFD domain to predict diurnal variability of C_p, same as the previous Chapter. Thereafter, this information was transported to an MNM domain by way of C_p profiles at the windows. Average contaminant concentration at zones has been predicted based on perfect mixing concept.

This type of hybrid NWP–CFD–MNM transient approach guarantees a reduction in computational resources and time while creating an innovative platform concept that uses several types of models and scales. IAQ and inhalation exposure risk prediction procedures can be potentially reduced this way.

5.2 METHODOLOGY OF HYBRID NWP–CFD–MNM TRANSIENT APPROACH

The hybrid NWP–CFD–MNM transient approach[5-4] explained in this chapter joins six domains. The first four domains have been analyzed through NWP (*NWP1~NWP4*) and represent a target area spanning several thousands of square kilometers (*NWP1*) until a refined area of tens of square kilometers with the target building at the center (*NWP4*). *NWP2* and *NWP3* are nested sub-domains of hundreds of square kilometers. These domains have previously been explained in Chapter 3and 4, having remained the same for this part of the study.

In this case, representative *NWP4* results have been treated and input as boundary conditions for domain *CFD2*, as explained in Chapter 4. Hourly change of wind pressure coefficient has been calculated at the walls of the building envelope under steady-state conditions in terms of mesoscale direction variability.

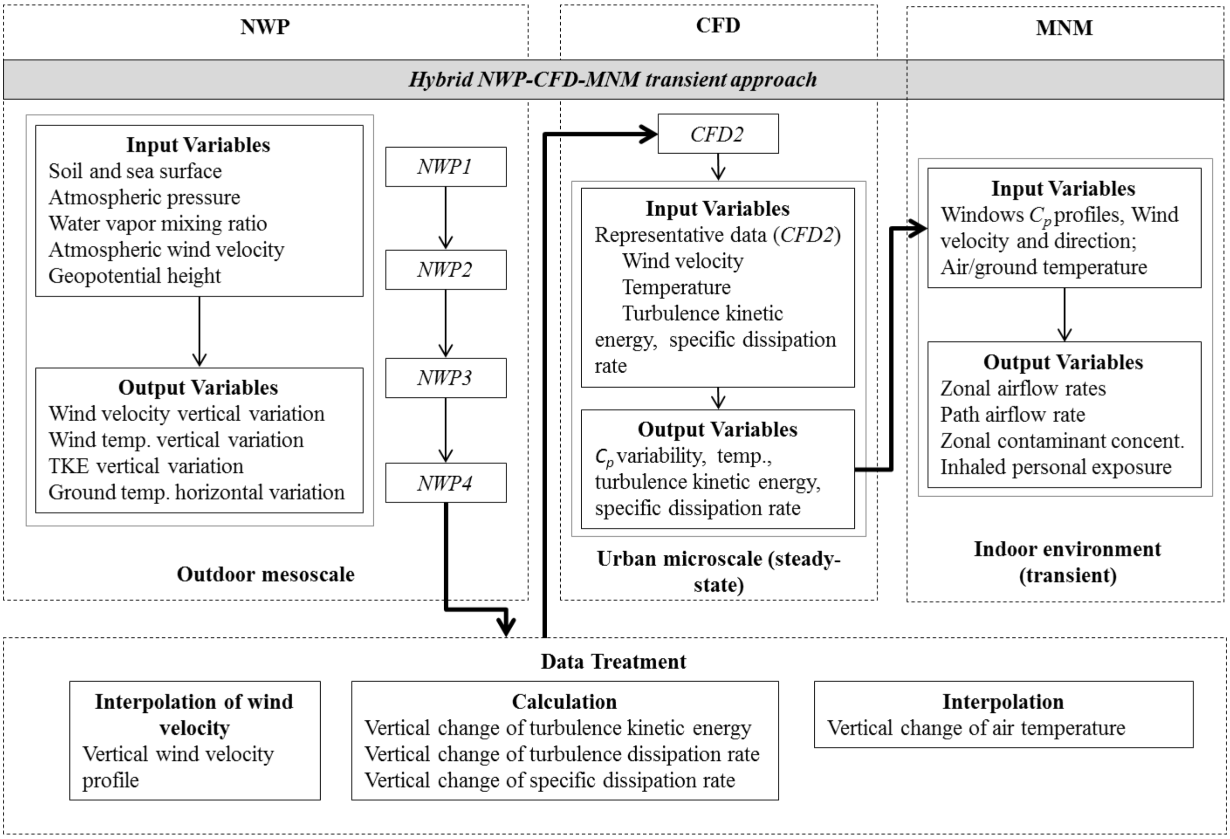

Figure 5-1. Outline of hybrid NWP–CFD–MNM transient approach

Transient indoor conditions and contaminant concentrations have been calculated based on C_p profiles built at the windows in the MNM model. This new domain using multizone network modeling has been divided into 4 zones (*MNM1~MNM4*). Finally, average indoor contaminant inside the target zone of the building was calculated. Figure 5-1 describes the outline of this approach.

5.2.1 NWP Dynamic Downscaling

As this domain has been previously explained, this section offers a brief description only. The complete detailed explanation of its design and numerical conditions have been stated in section 3.2.1.

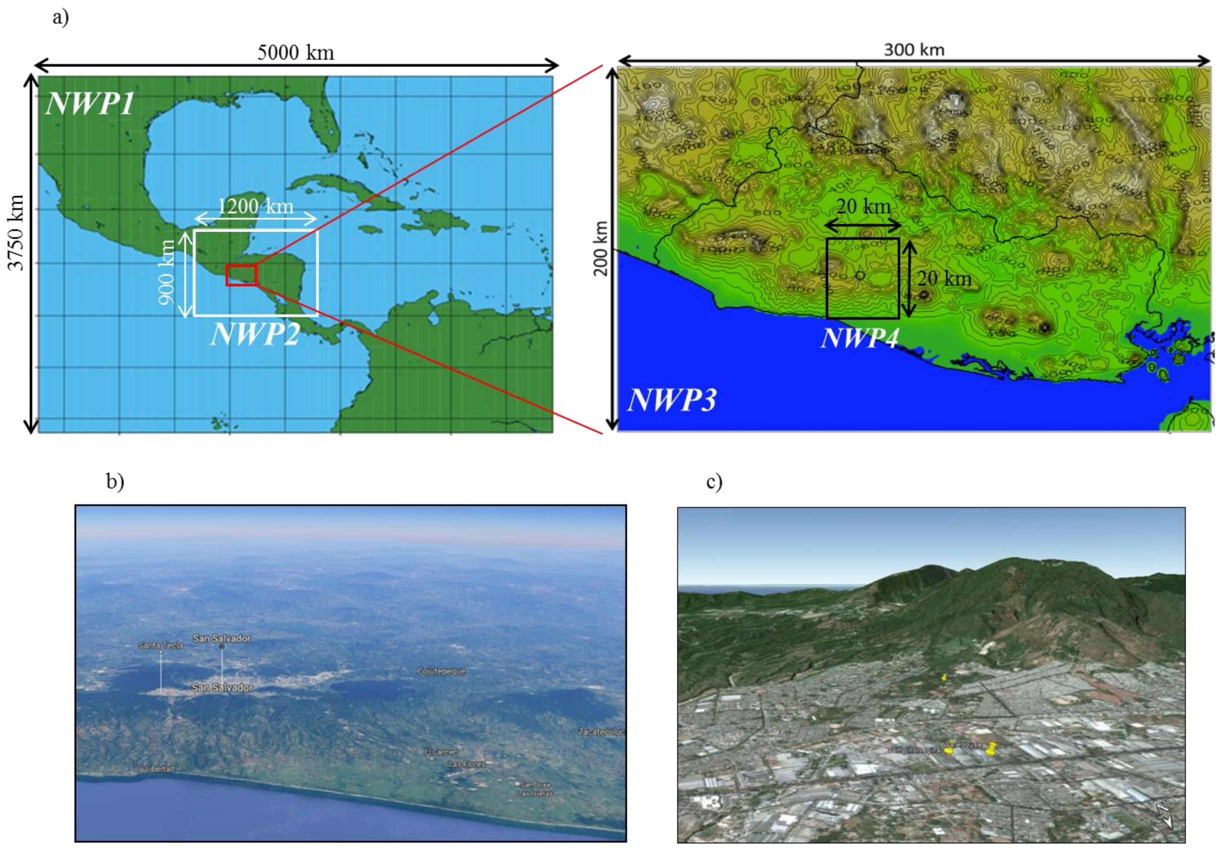

Figure 5-2. Further recollection of (a) NWP domains and (b) Topographical terrain of target area

All NWP domains encase the country of El Salvador, located in Central America between latitudes 13° and 15° N and longitudes 87° and 91°. Figure 5-2 presents once again all NWP domains (*NWP1~NWP4*), considered important in this study.

This part of the study was conducted during climatologically representative summer days during April 2012, from April 1st to April 30th and no peak meteorologically conditions or El Niño-Southern Oscillation (ENSO) were considered. Further explanation of geometry and mesh design as well as detailed boundary and other numerical conditions have already been explained in section 3.2.1. Table 5-1 has been once again presented to outline NWP boundary conditions.

Table 5-1. Numerical conditions for domains *NWP1* to *NWP4*

Component	**Condition and Scheme**
Cloud microphysics	Thompson scheme[5-5]
Long-wave radiation	RRTM scheme[5-6]
Short-wave radiation	Goddard scheme[5-7]
Surface layer	Monin–Obukhov scheme[5-8]
Ground surface	Noah Land–Surface model[5-9]
Atmospheric boundary layer	Mellor–Yamada–Janjic TKE scheme[5-8]
Cumulus parameterization	Grell 3D ensemble scheme (*for NWP1*)[5-10]

Further explanation of geometry and mesh design as well as detailed boundary and other numerical conditions have already been explained in section 3.2.1 and will thus be omitted. Time integration was performed during 30 days and the hourly output results of average wind velocities (three velocity components: u, v and w), wind direction, turbulence kinetic energy, air and surface temperature (ensemble averaged over a month) were treated and used to set as representative data for the inflow boundary conditions of domain *CFD2*.

5.2.2 NWP–CFD Data Treatment

This section describes briefly once again the procedure used in section 4.2.2.

5.2.2.1 Interpolation of Variables

As a first step, mesoscale data of wind velocity at every hour has been assumed 1 m/s. This was adopted to save numerical processing time. *NWP4*-obtained data of temperature has been maintained. Further adjustment of spatial distribution is described below.

- *Horizontal Interpolation*

Zeroth order interpolation has been applied to wind velocity, turbulence kinetic energy, turbulence dissipation rate, specific dissipation rate, and air temperature. This mathematical process applies a continuous step function for data over time/distance, as previously stated.

- *Vertical Interpolation*

In terms of vertical data spacing above 13 meters (first grid-point of NWP4 data results), wind velocity, turbulence kinetic energy, turbulence dissipation rate, specific dissipation rate, and air temperature were treated through 0th order interpolation.

Furthermore, wind temperature below 13 meters was linearly interpolated from ground surface to first-grid point for a rough approximation of vertical profile. Further vertical treatment of data below 13 meters is briefly explained in the following sections (5.2.2.2 and 5.2.2.3).

5.2.2.2 Vertical interpolation of wind velocity

A vertical wind profile that uses ¼ power law has been applied below 13 meters through the following equation (5.1):

$$U_2 = U_1 \left(\frac{z_2}{z_1} \right)^P \tag{5.1}$$

Where U_1 is the wind velocity at a known height, in this case, the first grid-point of *NWP4* results and z_1 is the corresponding height of 13 meters. z_2 is the corresponding height of velocity U_2, which has been interpolated every 0.5 meters until reaching ground level.

P is a function of both the atmpospheric stability in the layer over which P is determined and the underlying surface characteristics. This research assumes $P = 0.25$, for a ¼ power law for vertical wind profile.

5.2.2.3 Calculation of Variables

Further vertical treatment of data below 13 meters was performed. Turbulence kinetic energy (*TKE*), turbulence dissipation rate (*ε*) and specific dissipation rate (*ω)* have been calculated under the assumption that U_1 = 1 m/s, according to the findings made by Tominaga et al[5-11~5-13].

Turbulence kinetic energy was calculated through equation (5.2) as a function of height.

$$TKE_z = \left[0.018\left(\frac{z_2}{z_1}\right) + 0.015\right]U_1^2 \tag{5.2}$$

Where z_2 is the height from ground surface, spaced every 0.5 meters, z_1 is the lowest grid height corresponding to U_1^2, the square wind velocity at representative height (13 meters).

Turbulence dissipation rate *ε* and specific dissipation rate *ω* were calculated through equations (5.3) and (5.4) as functions of height also under the assumption that U_1 = 1 m/s. The constant C_μ has been set as 0.09.

$$\varepsilon_z = \frac{C_\mu TKE_z^{1.5} U_1}{4(C_\mu TKE_z)^{0.5} z_1^{0.25} z_2^{0.75}} \tag{5.3}$$

$$\omega_z = \frac{\varepsilon_z}{TKE_z} \tag{5.4}$$

Treated data was input into *CFD2* as boundary conditions for analysis of C_p variability based on 16 different wind directions, as explained in section 4.2.3.

5.2.3 Variability analysis of diurnal wind pressure coefficient (steady-state)

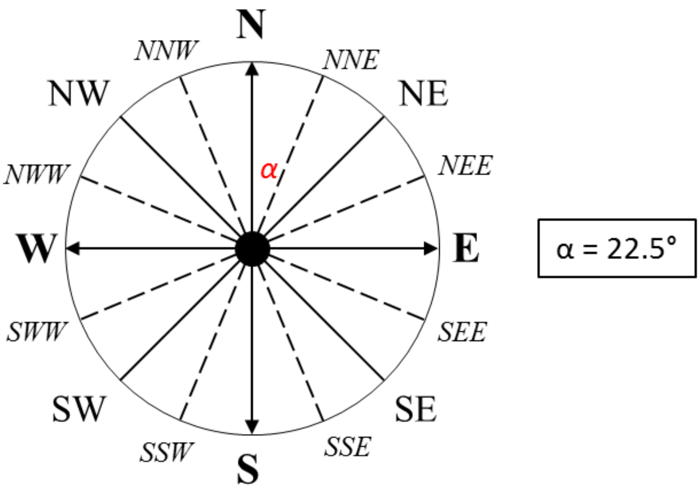

Figure 5-3. 16 directions assumed: cardinal, intercardinal and secondary-cardinal

First, 16 cases of prevailing daily wind have been assumed according to cardinal directions (N, S, E and W), intercardinal and secondary-intercardinal points (Figure 5-3).

CFD2 is briefly explained. A city-urban area of 200 square meters based on real elevation data was covered. Resolution of elevation points was of 5 meters.

Domain height was roughly 100 meters above ground level and the factory building was set at the center of the domain.

This region was discretized by an unstructured tetrahedral mesh of 2.45 million elements and grid cell size ranged from 5 meters at the boundaries to a few centimeters at the windows of the building envelope. ANSYS/ICEM 16.0 was also used for its design.

Figure 5-4 (a) shows the entire urban domain and Figure 5-4 (b) shows real terrain conditions of this region.

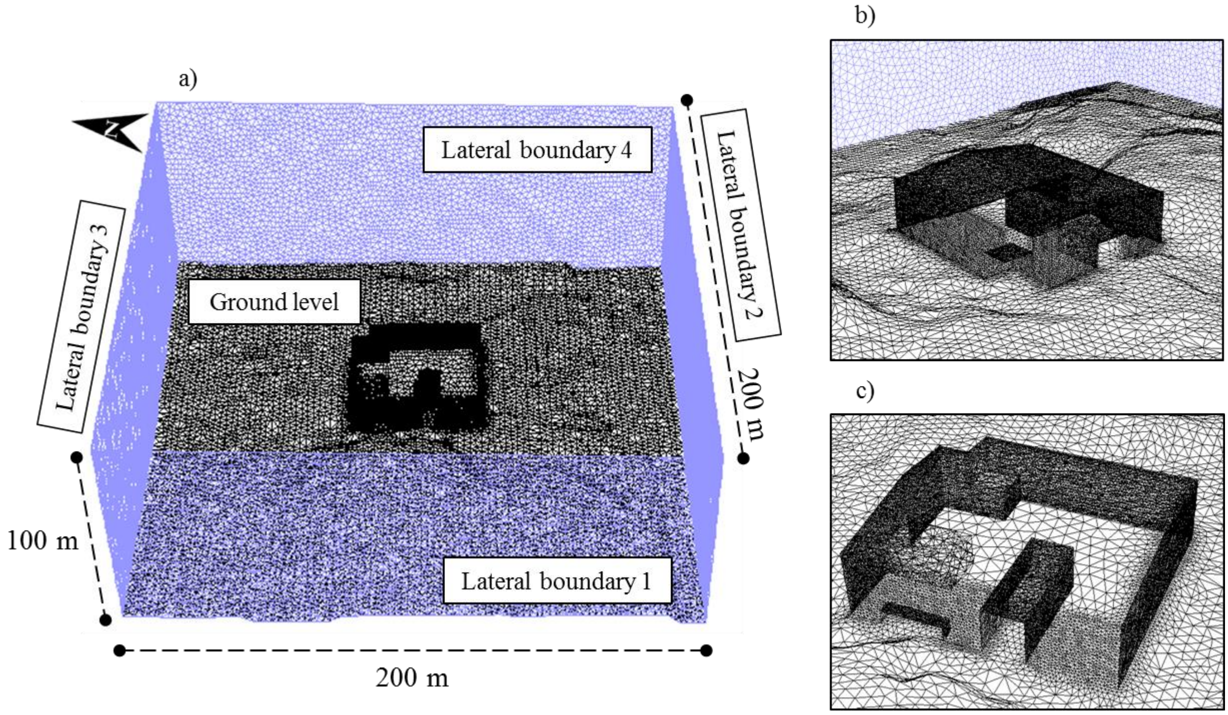

Figure 5-4 Mesh design (a) of *CFD2* domain, (b) of ground near factory (c) of factory

The SST *k-ω* model was used to simulate turbulence in *CFD2* and summarized numerical conditions are presented in Table 4-2. Further details can be read in section 3.2.3.1.

Table 5-2. Numerical conditions for domain *CFD2*

Component	**Condition**
Turbulence Model	SST Type *k-ω* model (3D calculation)
Mesh	2.45 Million Mesh (unstructured, tetrahedral)
Scheme	Algorithm: SIMPLE Convection Term: Second Order Upwind
Inflow Boundary	U_{in}, T_{in}, k_{in}, ω_{in} = *NWP4* treated data
Outflow Boundary	U_{out} ,T_{out}, k_{out} = Free Slip
Wall Boundary	Velocity: No Slip Temperature: T_{srf} = *NWP4* data

C_p distributions along the outside walls of the target building were calculated using equation (5.5):

$$C_p = \frac{P_{wall} - p}{\frac{1}{2}\rho v^2} \tag{5.5}$$

Where $P_{wall} - p$ represents the pressure difference between the outside wall and a determined representative point, ρ is the air density and v is the wind velocity at the openings.

Of these 16 cases, those which direction occurred during the day according to *NWP4* results were chosen and further treated.

Equations for azimuth correction and corrections for *TKE*, ε and ω are given by (5.6), (5.7), (5.8), and (5.9):

$$P_A = P_1 \times \left(\frac{b}{22.5}\right) + P_2 \times \left(\frac{a}{22.5}\right) \tag{5.6}$$

Where P_A is the corrected pressure including azimuth, P_1 is the static pressure at the current hour, P_2 is static pressure from previous hour, a is the product of integer division between angle of incidence and total degrees and b is $22.5 - a$.

$$TKE_A = TKE_1 \times \left(\frac{b}{22.5}\right) + TKE_2 \times \left(\frac{a}{22.5}\right) \tag{5.7}$$

$$\varepsilon_A = \varepsilon_1 \times \left(\frac{b}{22.5}\right) + \varepsilon_2 \times \left(\frac{a}{22.5}\right) \tag{5.8}$$

$$\omega_A = \omega_1 \times \left(\frac{b}{22.5}\right) + \omega_2 \times \left(\frac{a}{22.5}\right) \tag{5.9}$$

As the third and final step, corrected results of pressure, *TKE*, ε and ω were multiplied by representative mesoscale velocity from *NWP4* results to correct assumed mesoscale velocity = 1 m/s through the following equations:

$$P_c = P \times v_r^2 \tag{5.10}$$

$$TKE_c = TKE \times v_r^2 \tag{5.11}$$

$$\varepsilon_c = \varepsilon \times \frac{1}{v_r^3} \tag{5.12}$$

$$\omega_c = \omega \times \frac{1}{v_r^3} \tag{5.13}$$

Where $P_c, TKE_c, \varepsilon_c,$ and ω_c are the corrected variables, v_r is the ratio of local velocity (NWP4-obtained data) and representative mesoscale velocity = 1 m/s, [-]. $P, TKE, \varepsilon,$ and ω are results with assumed velocity =1 m/s. Real C_p data was used to build C_p profiles at the windows of the building modeled by MNM for transient urban wind flow variation.

5.2.4 Transient indoor air quality analysis through multizone network modeling

From this point on, multizone network modeling (MNM) has been introduced to the indoor air quality analysis for a transient hybrid approach and CFD-calculated pressure differences have been used as boundary conditions at the flow paths of the multizone calculation[5-14].

This type of modeling has been widely used in indoor design – for residential, commercial or industrial purposes – due to its good prediction of building air infiltration and contaminant transport under well-mixed conditions. Furthermore, this approach can calculate airflow and contaminant transport within minutes or even seconds, saving a significant amount of time and other resources[5-15~5-17].

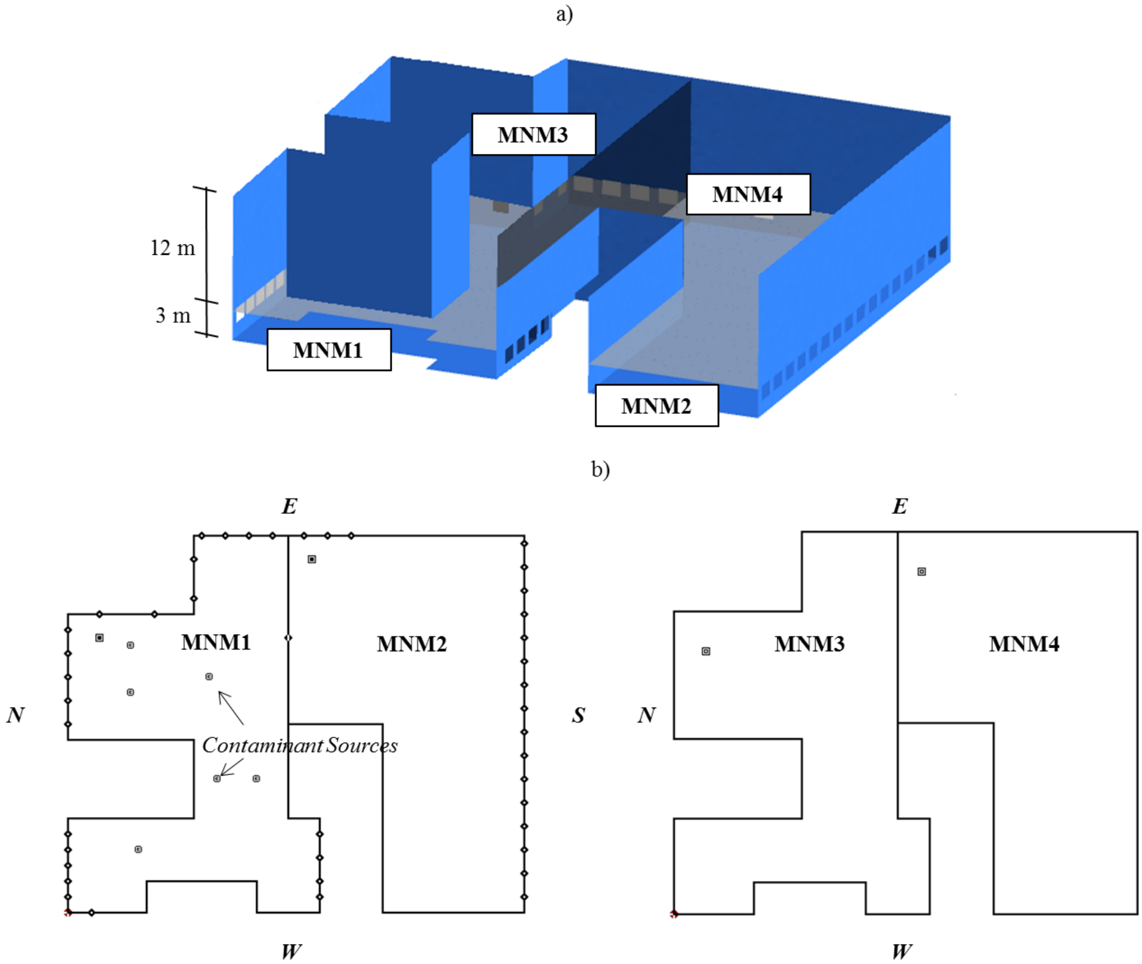

Figure 5-6. MNM design of (a) entire factory building (b) zones inside the building

In this part of the research, the MNM tool CONTAM, version 3.2 has been used to predict indoor quality by linking the city-urban environment to the indoor one. Building airflow was predicted by external wind pressures linked to the indoor environment through cross-ventilation for a transient analysis from 08:00 to 17:00 hours.

Figure 5-6 (a) describes the same target factory, this time simplified for a multizone approach. Factory dimensions were $(49.1 \times 55.7 \times 15)$ $(L \times W \times H)$ meters, where the gabled roof design was excluded due to the simplicity of the multizone modeling technique.

Furthermore, flow paths and contaminant sources have been modeled inside the enclosure. The enclosure was divided into two levels:

i) level 1 represented factory space up to a height of 3 meters, considered enough for human inhabitation,

ii) level 2 characterized the factory space above 3 meters.

Table 5-3. Numerical conditions for MNM domains

Component	**Condition**
Zones	*MNM1*: Normal, volume = 19160.30 *MNM2*: Normal, volume = 20765.30 *MNM3*: Phantom, volume = *MNM1* *MNM4*: Phantom, volume = *MNM2*
Initial temperature	*MNM1*: 24 °C (*CFD3* steady-state results) *MNM2*: 23 °C (*CFD3* steady-state results) *MNM3*: *MNM1* *MNM4*: *MNM2*
Airflow paths	One-way power law; orifice area data Cross-sectional area = 3 meters Discharge coefficient = 1 Flow exponent = 0.5 Relative elevation = 2.25 meters Wind pressure = variable (C_p profiles)
Contaminant	Constant coefficient Generation rate = 8.5 g/s Schedule: 0 g/s between 12:00 and 13:00 hours Species : Cyclohexanone

Moreover, the factory building was divided into four zones: *MNM1*, *MNM2*, *MNM3* and *MNM4*. *MNM1* was considered the most important one due to the positioning of the contaminant sources and worker's station, where the person is considered to spend most of the working day.

Table 5-3 shows the numerical conditions used for MNM analysis in the simplified factory illustrated above. Infiltration and contaminant transport principles used in CONTAM calculation have been explained in section 2.4.1 and 2.4.2, respectively. Total building volume was 39,925.60 cubic meters. Conformity of factory volume was maintained between CFD and MNM modeling.

Wind pressure coefficient profiles were created. In CONTAM software, variable wind pressure for an airflow path can be measured through a wind pressure modifier (wind pressure profile), which accounts for wind direction effects through the following equation:

$$P_w = \frac{\rho V^2}{2} C_h f\left(\theta\right) \quad (5.14)$$

Where ρ is ambient density, V is mesoscale velocity (.WTH file), C_h is the wind speed modifier coefficient accounting for terrain and elevation effects (calculated by CONTAM) and $f\left(\theta\right)$ is the wind pressure coefficient as a function of the relative wind direction.

To build $f\left(\theta\right)$, up to 16 angle/pressure coefficient pairs must be input. The first value must be 0°, which indicates wind blowing directly toward the surface opening. An identical value at 360° is assumed. 90° is the wind blowing parallel to the wall from the right and 270° is from the left. This is explained in Figure 5-7.

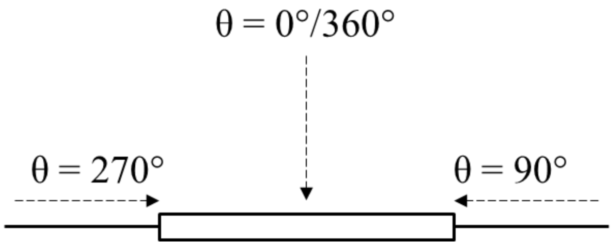

Figure 5-7. Angles of wind incidence according to CONTAM

C_p profile of each window has been presented in Figure 5-8 and Figure 5-9. Values vary from 0 to 1, being slightly higher than one in a couple of cases. In each profile, diurnal variation in terms of incoming wind direction at the window can be appreciated. City-urban flow field has been introduced this way into the MNM enclosure.

To account for other urban-city environment impact during the day, not only C_p profiles but also weather conditions during a 24-hour period have been introduced for the transient calculation. These weather conditions have been input into CONTAM as a weather file (.WTH) and are summarized in Table 5-4.

Although any period of time can be analyzed under transient conditions, the shortest time CONTAM software allows for weather variation is a 24-hour period, from 0:00:00 to 24:00:00. In this situation, NWP representative results have been used as input for the transient weather file. No precipitation has been considered.

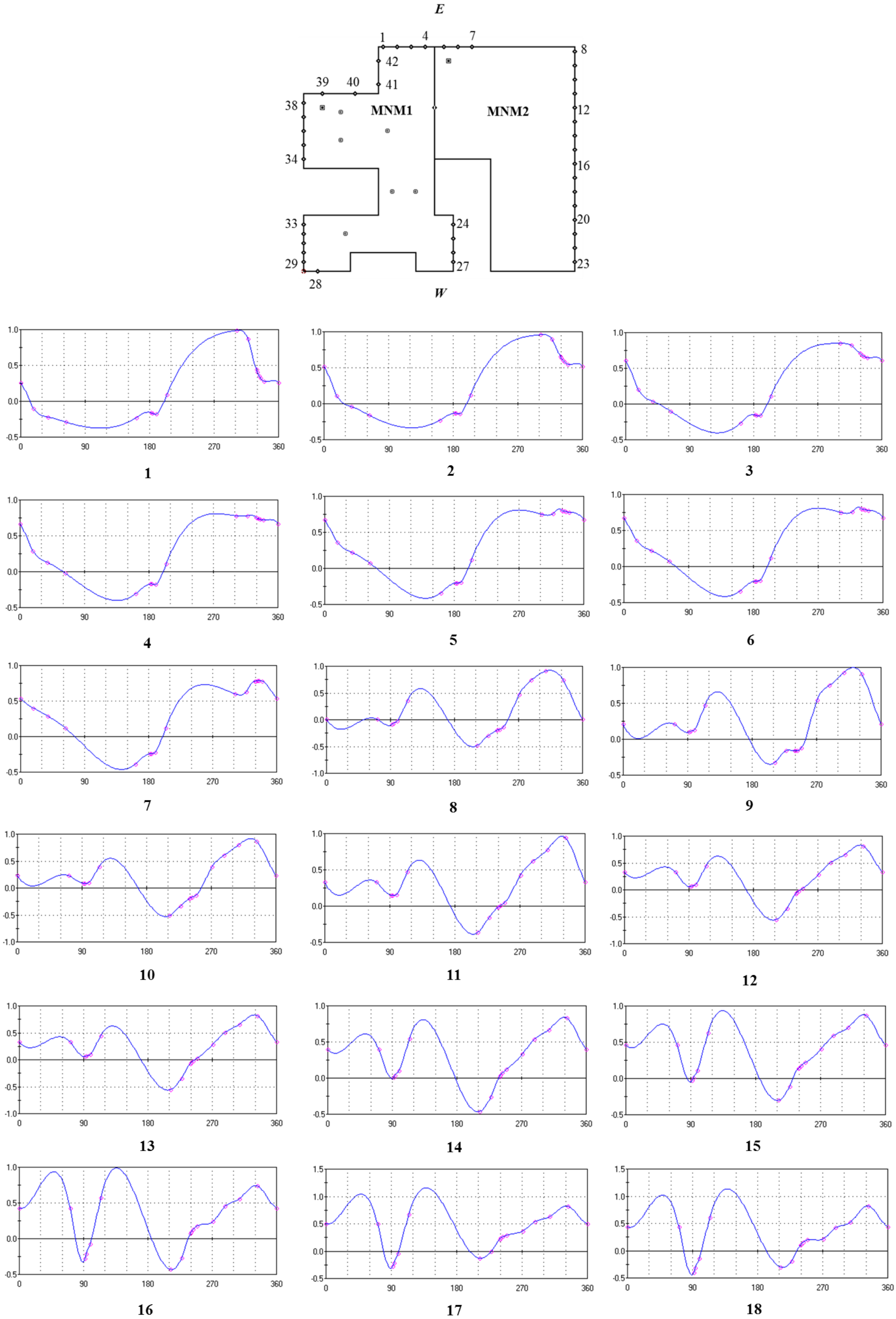

Figure 5-8. C_p profiles from windows 1-18

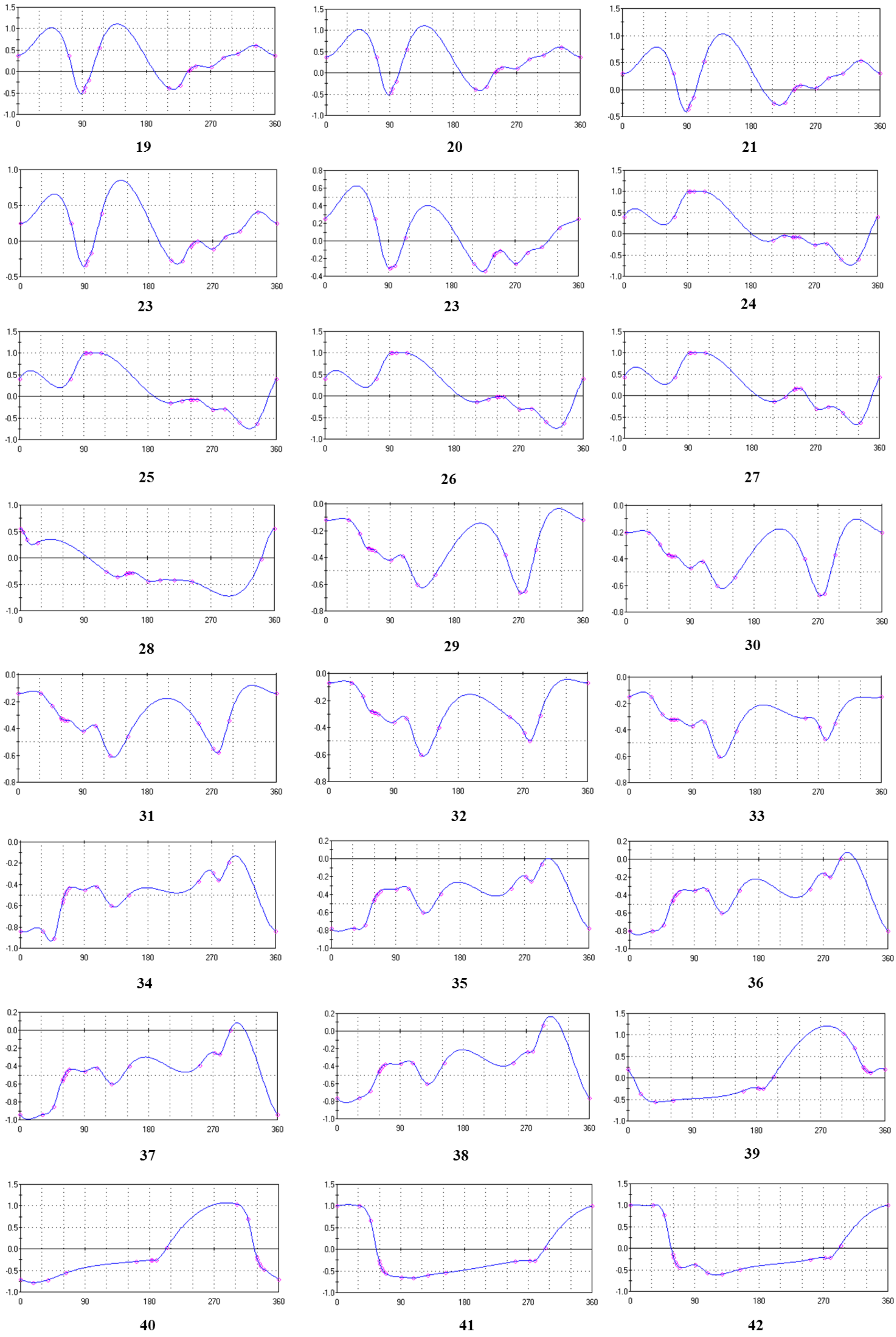

Figure 5-9. C_p profiles from windows 19-42

Table 5-4 Transient weather conditions for MNM analysis

Time	**Air temp. (°C)**	**Absolute Pressure (Pa)**	**Wind velocity (m/s)**	**Azimuth (°)**
01:00	18.35	101040.1	5.94	60.2
02:00	18.39	101040.1	6.18	60.2
03:00	18.39	101040.0	6.71	62.8
04:00	18.20	101040.0	7.35	64.8
05:00	18.06	101040.0	6.49	63.0
06:00	18.19	101040.1	5.86	58.7
07:00	18.50	101040.1	5.16	59.7
08:00	18.43	101040.2	6.08	69.1
09:00	17.94	101043.7	2.98	91.2
10:00	20.14	101048.6	2.53	107.9
11:00	21.40	101050.5	1.96	128.3
12:00	22.80	101051.0	0.52	152.7
13:00	23.47	101058.6	2.29	250.6
14:00	22.23	101054.3	6.63	272.1
15:00	22.04	101053.9	8.30	274.2
16:00	21.62	101052.9	9.78	278.9
17:00	21.53	101052.7	8.94	279.8
18:00	21.56	101052.8	5.99	279.5
19:00	20.37	101049.8	2.80	293.7
20:00	19.78	101040.2	1.51	32.1
21:00	19.33	101040.3	1.96	47.3
22:00	18.28	101040.1	3.83	61.7
23:00	18.05	101040.0	5.72	64.9
24:00	18.35	101040.1	5.28	60.7

5.3 RESULTS AND DISCUSSION

This section presents the results of the hybrid NWP–CFD–MNM transient approach. NWP results have been averaged over a 30-day period while CFD results are divided into steady-state results; MNM results are presented for a transient solution.

5.3.1 NWP Dynamic Downscaling Results

Since NWP results have already been presented in previous Chapters (Chapter 3 and Chapter 4), they have been summarized to times between 08:00 and 17:00 hours.

Table 5-5 summarizes *NWP4* mesoscales results of wind direction (azimuth) and wind velocity magnitude. These results were used for both the C_p diurnal variation analysis and as input for the weather file used for the multizone analysis in terms of transient city-urban conditions.

Table 5-5. NWP4 results of wind velocity and wind direction

Hour	**Direction**	**Azimuth (°)**	**Veloc. Magnit. (m/s)**
08:00	NNW	69.1	6.08
09:00	N	91.2	2.98
10:00	NNE	107.9	2.53
11:00	NE	128.3	1.96
12:00	ENE	152.7	0.52
13:00	SSE	250.6	2.29
14:00	S	272.1	6.63
15:00	S	274.2	8.30
16:00	S	278.9	9.78
17:00	S	279.8	8.94

5.3.2 Wind pressure coefficient variability results

5.3.2.1 C_p variability results for v=1 m/s

Results of corresponding C_p distribution along the outside walls of the building envelope have been summarized for all 16 prevailing wind directions when mesoscale velocity v=1 m/s (Figure 5-10).

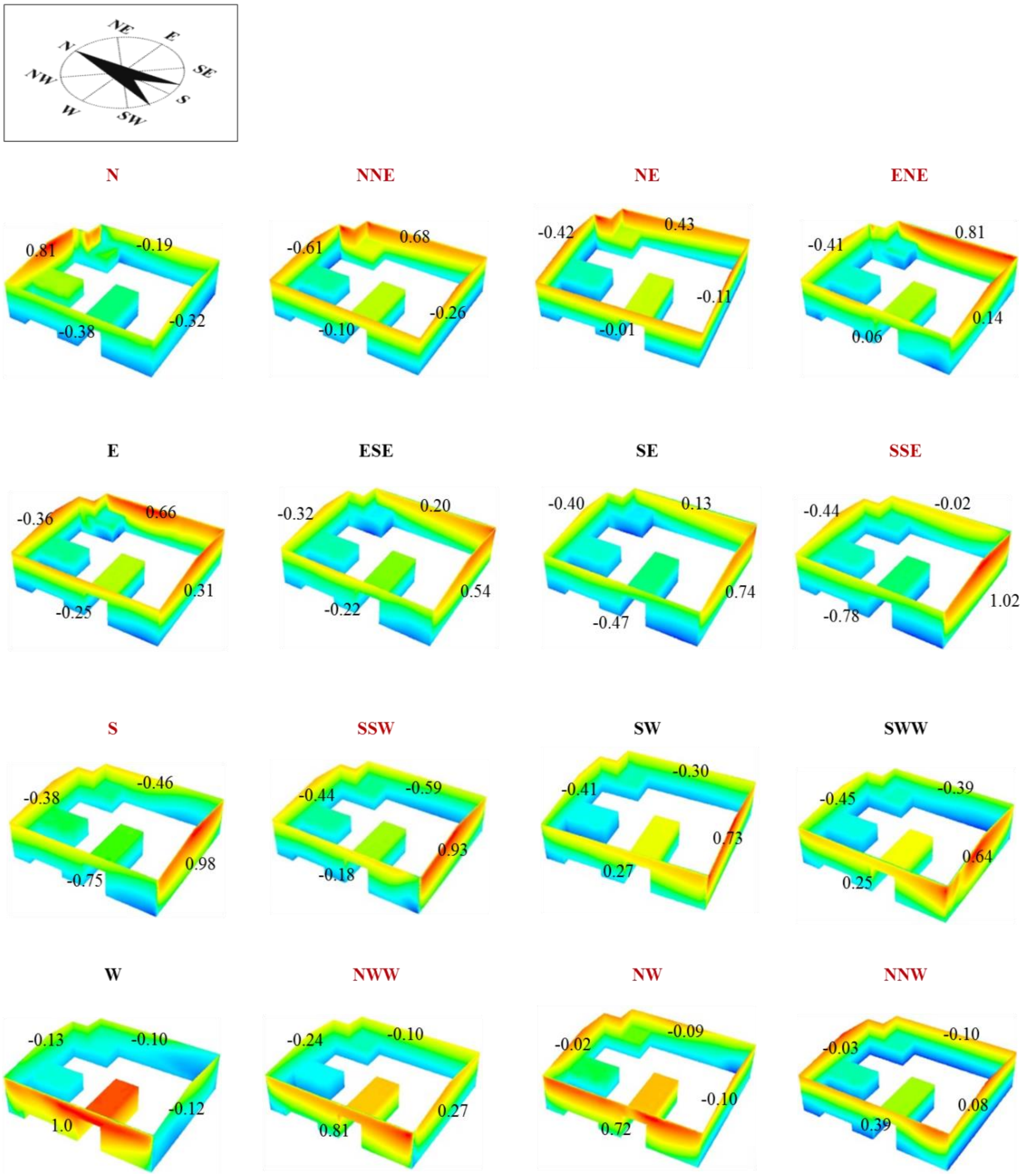

Figure 5-10 C_p steady-state results at the walls of the building envelope for every prevailing wind direction at each hour (mesoscale v=1 m/s)

5.3.2.2 C_p variability results for real mesoscale representative velocity

Results of average C_p at each window for mesoscale representative velocity are shown (Figure 5-11). Windows information was used to transport flow field to the MNM model.

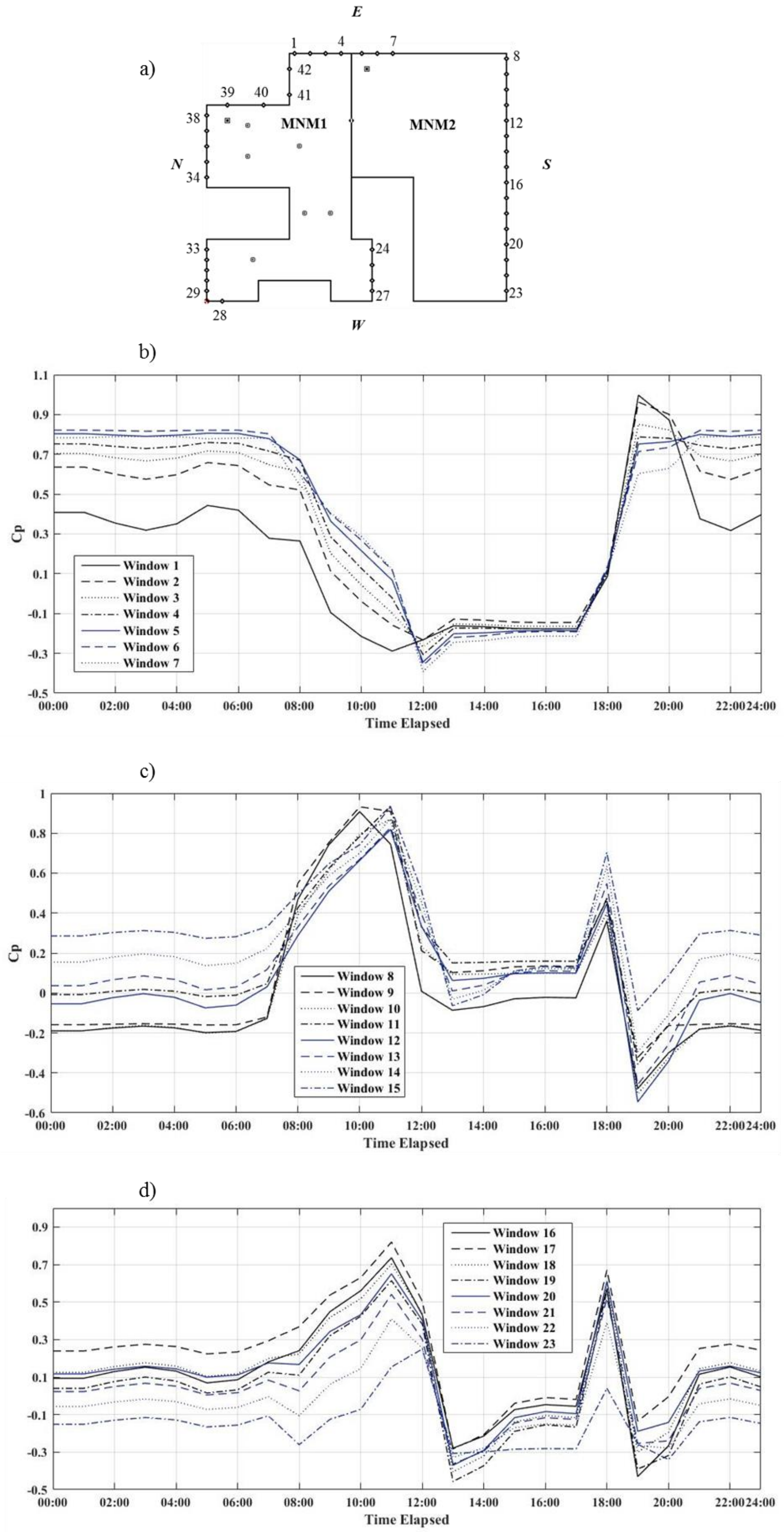

d)

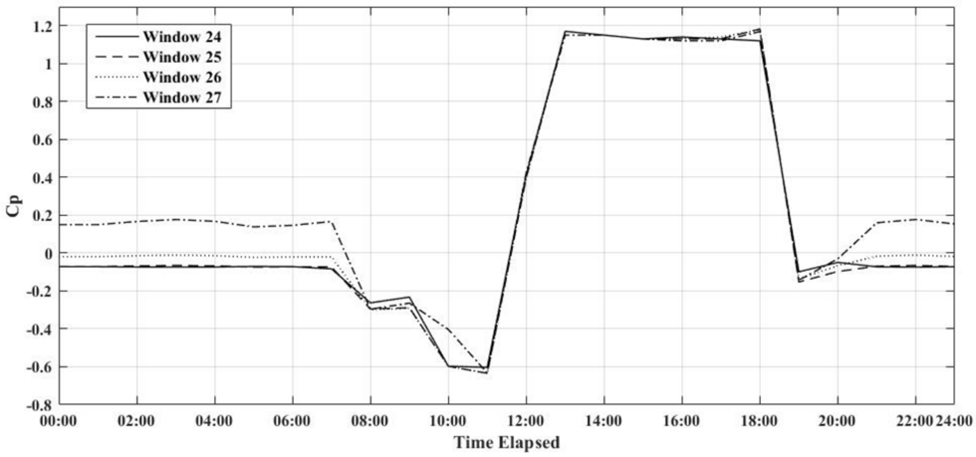
Window 24
Window 25
Window 26
Window 27
Cp
Time Elapsed

e)

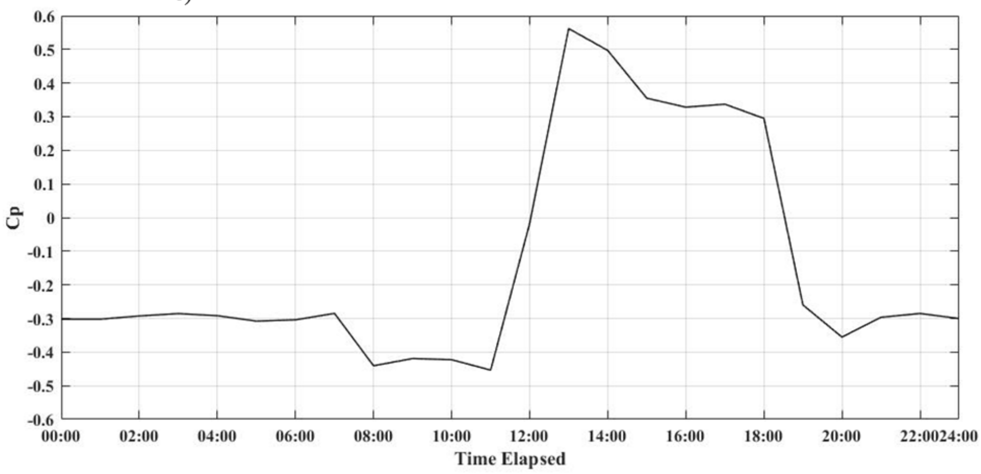
Cp
Time Elapsed

f)

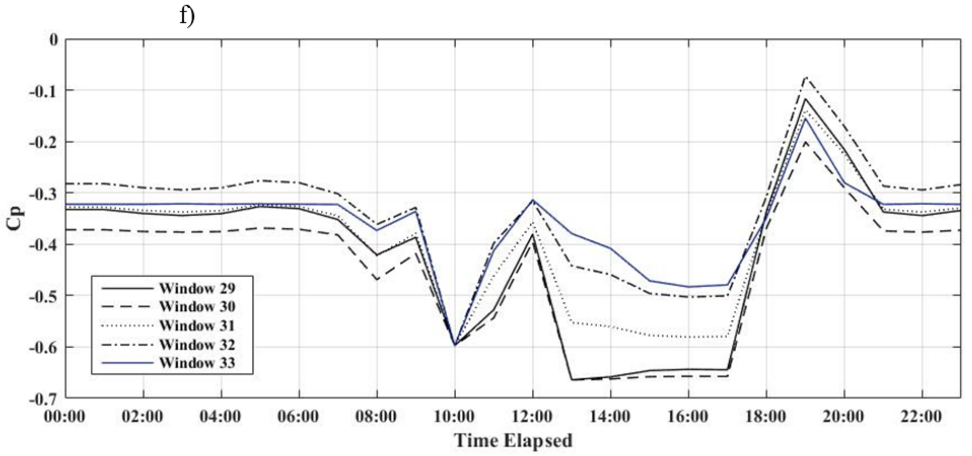
Window 29
Window 30
Window 31
Window 32
Window 33
Cp
Time Elapsed

g)

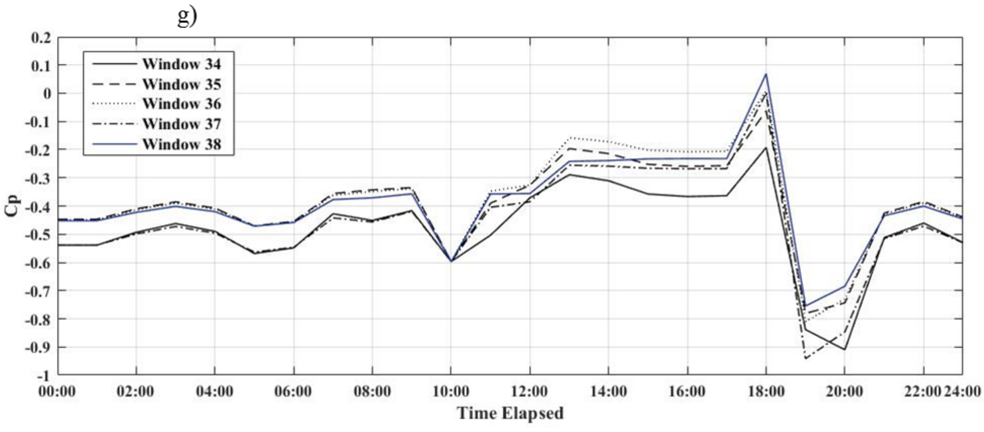
Window 34
Window 35
Window 36
Window 37
Window 38
Cp
Time Elapsed

h)

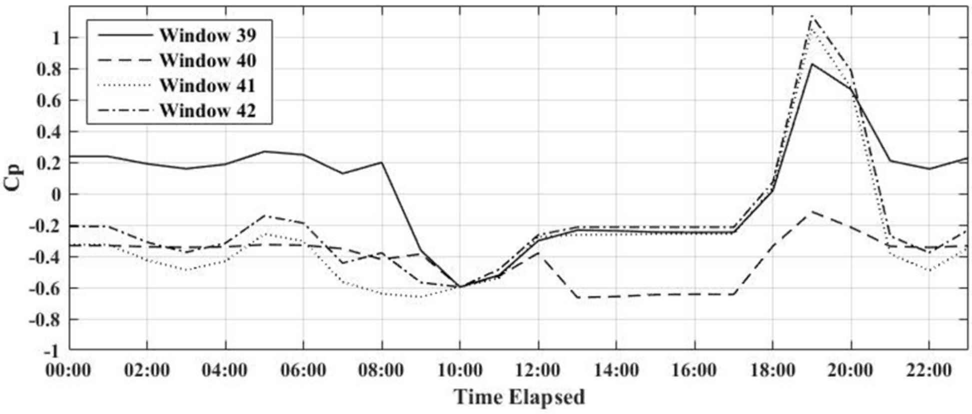

Figure 5-11 C_p at each window during 24 hours, grouped by wall

5.3.3 Transient indoor air quality results through MNM

The above summarized C_p variation during the day was used to transfer urban wind conditions to the inside of the factory building modeled by MNM.

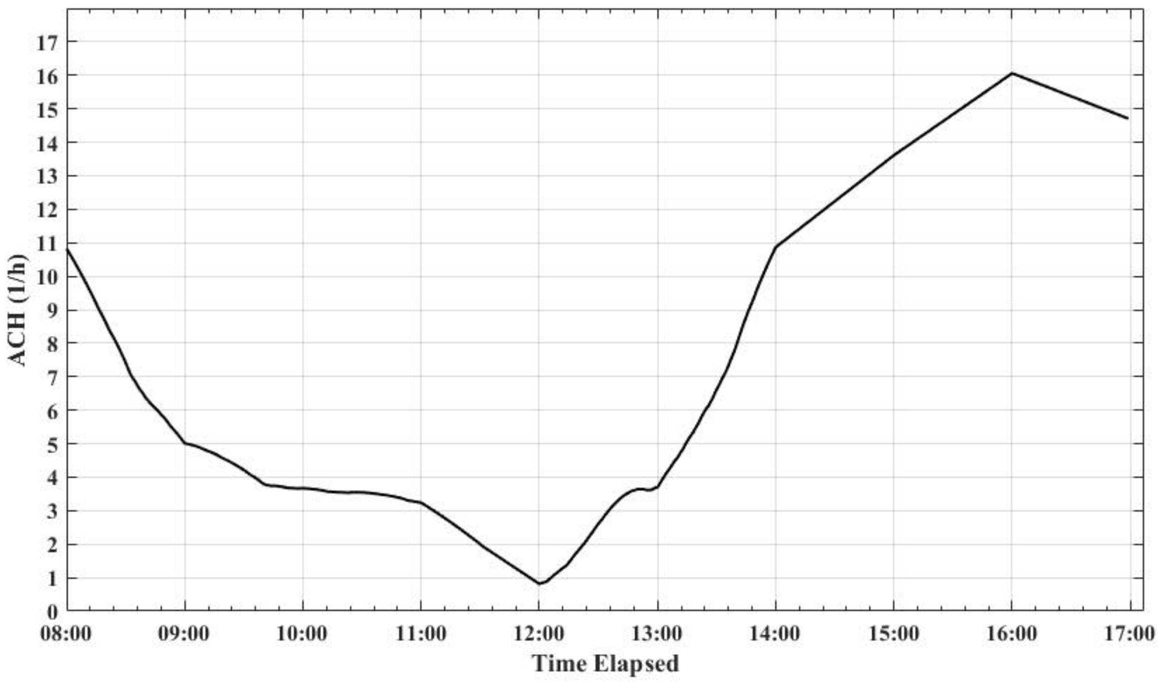

Figure 5-12. Transient factory ACH results by MNM

Figure 5-12 presents ACH results inside the factory based on outdoor transient conditions calculated through pressure at the air flow paths. As can be seen, ventilation rate – represented by ACH – changed greatly during the day, as well as C_p profiles at the windows.

In order to prove the viability of both the full NWP–CFD and hybrid NWP–CFD–MNM approaches, a comparison of ACH between both methods was made. Figure 5-13 shows the comparison of transient ventilation rate in terms of both techniques.

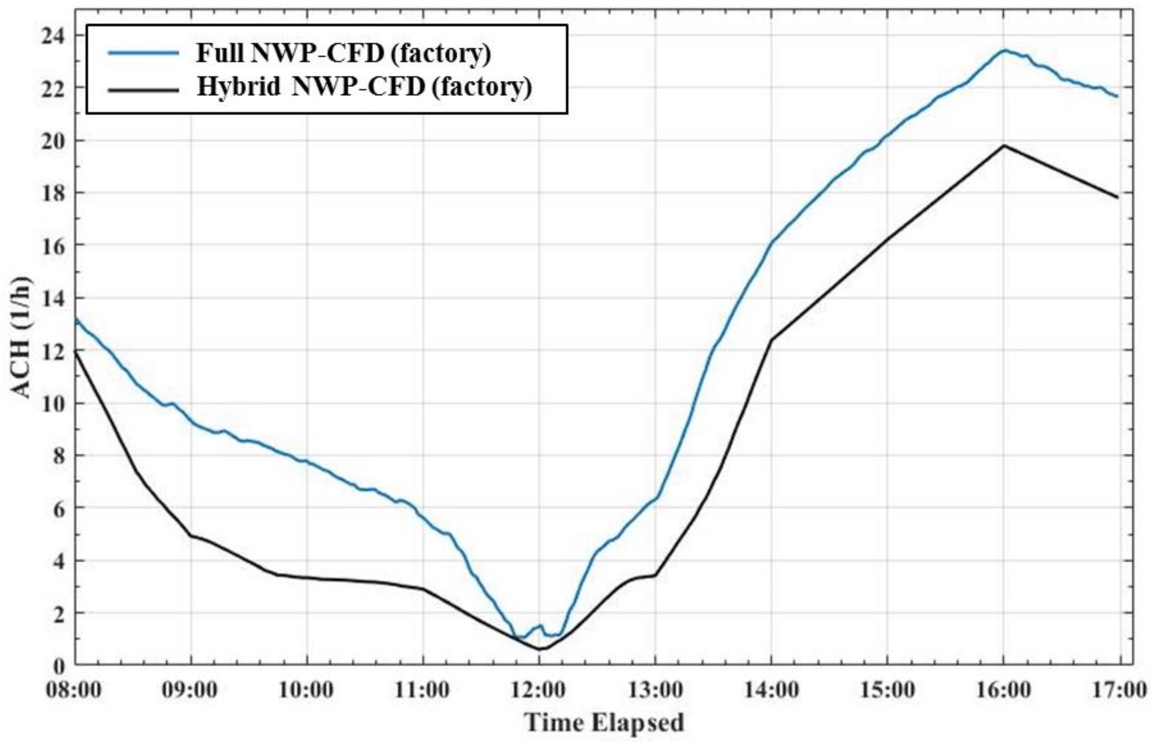

Figure 5-13. Comparison of transient factory ACH results by full NWP–CFD and hybrid NWP–CFD–MNM approaches

As can be seen, although trend is the same during the analyzed time, there is a discrepancy in values between both cases and the hybrid NWP–CFD–MNM approach predicts a lower ventilation rate under the same circumstances and boundary conditions. This difference is especially significant between 09:00 and 11:00 hours and between 15:00 and 17:00 hours. Noon time discrepancy is not as large.

Since three-dimensional analysis at the design stage of buildings is not a viable option, network modeling is widely used to represent the macroscopic behavior of fluid movements. Due to this reason, multizone network modeling is widely preferred (CONTAM, COMIS, etc.) and has been extensively scrutinized[5-18~5-20].

It has been concluded that there are certain limitations to macroscopic modeling (MNM) when applied to cross-ventilation conditions due to fundamental differences between infiltration (MNM) and cross-ventilation analysis with wide open windows (CFD).

These differences become wider when analyzing large buildings with multiple windows, which differ from infiltration cracks. Essentially, energy dissipation of the jet discharge (of air) between one approach and the other becomes different. In case of infiltration, dynamic pressure is dissipated into heat and the recovery of static pressure due to dynamic pressure does not occur. Therefore, total pressure loss is the same as static pressure loss[5-21].

However, in case of deep cross-ventilation analysis through CFD, a major part of dynamic pressure does not dissipate into heat and the total pressure loss is not the same as the static pressure difference. This becomes stronger if the openings of the building (windows) are bigger.

This study has tried to adjust to this phenomenon by correcting the pressure loss coefficient – i.e. discharge coefficient – to a value of 1.0. Although the situation has improved, it is clear that some adjustments still need to be done for a closer approximation of both approaches.

Finally, contaminant concentration inside MNM1 of the factory has been calculated. Figure 5-14 shows results of contaminant concentration at MNM1 in terms of time elapsed and wind direction. Zonal contaminant concentration results (MNM1) are higher than those presented in Chapter 4 for the full NWP–CFD transient approach. This might be a direct influence of the lower ACH explained above.

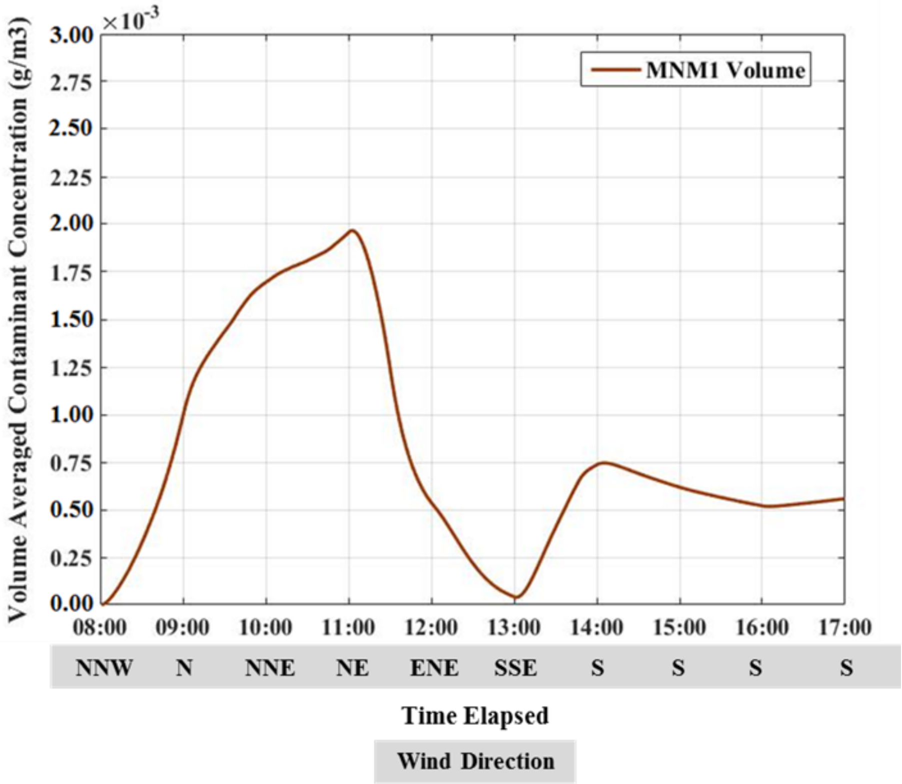

Figure 5-14. Contaminant concentration inside MNM1 volume

5.4 CONCLUSION

In this transient indoor quality study, diurnal variation of wind pressure coefficient distributions along the outside walls of a target building were used to build C_p profiles at the windows of the building. A transient analysis has been thereby performed and local flow field and contaminant concentration have been predicted below the building scale.

In this case, NWP representative conditions were used to calculate variation of C_p during the day according to prevailing wind direction by CFD. Thereafter, these C_p profiles were set as boundary conditions for the transient indoor air quality analysis in MNM.

C_p results showed that variability in wind direction and urban flow field has a direct impact in the change of pressure distribution along the walls of a building envelope. This variation directly affected ACH during the day, impacting zonal contaminant concentration in *MNM1*. A comparison was made between both approaches to measure their suitability and it was found that ACH was somewhat under predicted in the hybrid approach. The reason of this is because of the differences in calculating pressure loss in terms of infiltration rate and full cross-ventilation analysis. Discharge coefficient has been adjusted to overcome this problem but further corrections need to be made for a completely correlated analysis.

Contaminant concentration in *MNM1* calculated through the hybrid analysis was found to be higher than in the case of the full approach. This might be due to the slight under prediction of ventilation rate inside the factory analyzed by network modelling.

This approach has demonstrated the use of less resources and time, being the tool of choice of many designers and researchers at the first stage of building design but there are some limitations that need to be overcome. Nevertheless, contaminant concentration at the working zone was predicted for further analysis.

References

5-1) Carpenter SC. "Energy and IAQ impact of CO2-based demand-controlled ventilation". *ASHRAE Tran*, vol. 102 (2), pp. 80–88, 1996.

5-2) Persily AK, Musser A, Emmerich SJ, and Taylor AW. "Simulations of indoor air quality and ventilation impacts of demand controlled ventilation in commercial and institutional buildings". *NISTIR 7042*. Gaithersburg: National Institute of Standards and Technology.

5-3) Ng L, Musser A, Persily A, and Emmerich S. "Indoor air quality analyses of commercial reference buildings". *Build. Environ,* vol. 58, pp. 179-187, 2012.

5-4) Murga A, and Ito K. "Dynamic downscaling and hybrid CFD – transient network modelling analysis for estimating inhaled air quality", *In: Proceedings of Building Energy and Environment, COBEE, 2018,* Paper ID: 160, pp. 481-486, 2018.

5-5) Thompson G, Field PR, Rasmussen RM, Hall WD. "Explicit forecasts of winter precipitation using an improved bulk microphysics scheme. Part II: implementation of a new snow parameterization". *Mon. Weather Rev.,* vol. 136, pp. 5095–5115, 2008.

5-6) Mlawer EJ, Taubman SJ, Brown PD, Iacono MJ, Clough SA. "Radiative transfer for inhomogeneous atmospheres: RRTM, a validated correlated-k model for the longwave". *J. Geophys. Res. Atmos*., vol. 102, pp. 16663–16682, 1997.

5-7) Chou MD, Suarez MJ, Liang XZ, Yan MMH. "A thermal infrared radiation parameterization for atmospheric studies". *NASA Tech. Memo*. 104606 (19), 68, 2001.

5-8) Janjic Z. "Nonsingular Implementation of the Mellor-yamada Level 2.5 Scheme in the NCEP Meso Model". National Centers for Environmental Prediction, 2002.

5-9) Tewari M, Chen F, Wang W, Dudhia J, LeMone MA, Mitchell K, Ek M, Gayno G, Wegiel J, Cuenca RH. "Implementation and verification of the unified NOAH land surface model in the WRF model". *In: Proceedings of the 20th Conference on*

Weather Analysis and Forecasting/16th Conference on Numerical Weather Prediction. American Meteorological Society, Seattle, WA, US. January 11–15, 2004.

5-10) Grell GA, and Dévényi D. "A generalized approach to parameterizing convection combining ensemble and data assimilation techniques," *Geophys. Res. Lett.*, vol. 29, no. 14, pp. 38-1-38–4, Jul., 2002.

5-11) Tominaga Y, Mochida A, Yoshie R, Kataoka H, Nozu T, Yoshikawa M, and Shirasawa T. "AIJ guidelines for practical applications of CFD to pedestrian wind environment around buildings", *J. of Wind Eng. and Ind. Aero.*, vol 96, pp. 1749–1761, 2008.

5-12) Mochida A, Tominaga Y, Murakami S, Yoshie R, Ishihara T, Ooka R. "Comparison of various k-εmodel and DSM applied to flow around a high-rise building - report on AIJ cooperative project for CFD prediction of wind environment", *Wind & Structures 5*, No.2–4, pp. 227–244, 2002.

5-13) Shirasawa T, Tominaga T, Yoshie R, Mochida A, Yoshino H, Kataoka H, and Nozu T, "Development of CFD method for predicting wind environment around a high-rise building Part2: The cross comparison of CFD results using various k- models for the flowfield around a building model with 4:4:1 shape", *AIJ Journal of Technology and Design*, No.18, pp. 169–174, 2003. (In Japanese)

5-14) Schaelin A, Dorer V, van der Maas J, and Moser A. "Improvement of multizone model predictions by detailed flow path values from CFD calculations". *ASHRAE Transactions*, vol 100 (Part 2), pp 709–720, 1993.

5-15) Haghighat F, Megri AC. "A comprehensive validation of two airflow models—COMIS and CONTAM". *Indoor Air-International Journal of Indoor Air Quality and Climate*, vol. 6 (4), pp. 278–88, 1996.

5-16) Upham R. “A validation study of the airflow and contaminant migration computer model CONTAM as applied to tall buildings”. *University Park, PA*: The Pennsylvania State University, 1997

5-17) Emmerich SJ. “Validation of multizone IAQ modeling of residential-scale buildings: a review”. *ASHRAE Transactions,* vol. 107 (2), pp. 619–28, 2001.

5-18) Vickery BJ, and Karakatsanis C. “Correlations for pressure distribution on buildings and calculation of natural ventilation air flow”. *ASHRAE Transactions*, vol. 94, Part 1, pp. 243–266, 1987.

5-19) Walton GN. “Airflow network models for element-based building airflow modeling” *ASHRAE Transactions*, vol. 95, Part 2, pp. 611–620, 1989.

5-20) Liddament M, and Allen C. “The validation and comparison of mathematical models of air infiltration”, *Technical Note AIC No. 11–83*. Bracknell, England: Air Infiltration Center, 1983.

5-21) Kato S. “Flow Network Model based on Power Balance as Applied to Cross-Ventilation,” *Int. J. Vent.*, vol. 2, no. 4, pp. 395–408, 2004.

[Previously published documents related to this chapter]

[1] Murga A, and Ito K. “Dynamic downscaling and hybrid CFD – transient network modelling analysis for estimating inhaled air quality”, *In: Proceedings of Building Energy and Environment, COBEE, 2018,* Paper ID: 160, pp. 481-486, 2018.

Award winning paper: Best Paper, Women In STEM

SUMMARY AND FUTURE WORK

6.1 SUMMARY

This study developed an integrated method that transfers flow field, turbulence and pollutant from the global climate scale to the human body and mucosal epithelium cell scale. Global-climate has been analyzed by NWP and transferred to the city-urban scale by CFD. Thereafter, building-indoor environment and below-scales have been analyzed based on city scale wind flow field and turbulence using CFD and MNM. By applying this integrated method, indoor contaminant concentration and inhalation exposure risk have been predicted.

Three approaches have been applied during this study:

i) NWP–CFD dynamic downscaling that analyses flow field and pollutant at certain points in time (steady-state);

ii) full NWP–CFD transient approach that uses representative mesoscale results to calculate city-urban flow field and transfer it to a factory with an integrated CSP; and,

iii) hybrid CFD–NWP–MNM transient approach that uses representative mesoscale results to transfer them to the city-urban scale and calculate C_p profiles along the windows of a building for macroscopic network modelling analysis of flow field and pollutant.

Approach i) has been explained in Chapter 3, approach ii) in Chapter 4 and approach iii) in Chapter 5, respectively.

A summary of each chapter is presented:

Chapter 1 summarized the introduction and literature necessary to the better understanding of the present study. Its main focus was the need of including mesoscale climate into the urban environment to analyze IAQ from a contemporary point of view. Furthermore, the innovative method that overcomes the need of great resources and limited physical measurements, resulting in a cost-effective method, has also been discussed.

Chapter 2 described the fundamental mathematical models that describe the physical characteristics of each downscaled environment through numbers and equations. For the global climate scale analysis, the Weather Research and Forecasting (WRF) version 3.6.1 has been explained. For the city urban-built scale, the CFD software, ANSYS Fluent version 16.0 has been described for the application of the Navier-Stokes equations. For the below-building scale MNM approach, CONTAM version 3.2 for has been discussed. Through MNM, average features of flow field and contaminant transport have been predicted. Governing equations of momentum, energy and scalar transport of each mathematical model have been therefore described.

Chapter 3 summarized the NWP–CFD dynamic downscaling procedure under steady-state conditions. Here, wind pressure coefficient distributions along the outside walls of a target building were calculated through transferred global climate scale and urban-city scale wind flow field by way of dynamic downscaling (NWP–CFD). Wind pressure coefficient distributions at the walls of the building envelope were successfully predicted, proving the viability of this technique in regions where wind environmental monitoring data is not sufficiently measured for detailed research.

Indoor air flow field, local contaminant concentration and inhalation exposure (through inhaled volume) for a human worker inside a factory were analyzed. A CSP and respiratory tract model (human scale and mucosal epithelium cell scale) were introduced for this analysis.

Cross-ventilation variability was studied at four times of the day to confirm global-urban effects on building-indoor and below-building scale contaminant concentration and inhalation exposure risk. It was found that indoor contaminant concentration depended also on the worker's location in the building.

Chapter 4 compiled the full NWP–CFD integrated analysis from a transient point of view. Diurnal variation of wind pressure coefficient distributions at the walls of a building was predicted to transfer city-urban flow field to the building-indoor environment. Prevailing hourly wind direction under steady-state was used to predict wind pressure coefficient.

In this transient analysis, indoor air flow and contaminant concentration were analyzed from 08:00 to 17:00 hours based on variable wind direction and contaminant schedule. Urban flow field influenced ACH variation, which had a direct impact in diurnal contaminant concentration. Furthermore, a CSP was integrated to the building to analyze inhalation exposure risk at the nares of the human body. Although the viability of this approach was confirmed in terms of full analysis that includes all variables and boundary conditions, one of the disadvantages is the great amount of computational resources and time needed, as confirmed by this study. Simulation time was of eight days (real-time) for the analysis between 08:00 to 17:00 hours. Due to this reason, a hybrid NWP–CFD–MNM approached that consumes fewer resources was suggested.

Chapter 5 defined the hybrid NWP–CFD–MNM integrated analysis from a transient point of view. In this second alternative for a transient approach, variation of wind pressure coefficient distributions along the outside walls of a target building were used to build C_p profiles at the windows of a building to join outdoor and indoor environment.

In this case, NWP representative results were used to calculate variation of C_p during the day according to prevailing wind direction by CFD. C_p results showed that variability in wind direction directly impact urban pressure distribution and their transport for indoor air flow analysis. This information was used to create C_p profiles at the air flow paths (windows) of the building, which had been modeled through MNM for the transient indoor air quality analysis.

Although ACH was also found to vary considerably during the day, the comparison made between both transient approaches showed that MNM-calculated ACH was slightly under predicted. It has been concluded that pressure calculation through infiltration (MNM) and detailed cross-ventilation (CFD) was the reason for this difference. Although discharge coefficient has been adjusted to compensate for this, further corrections need to be made for a completely corroborated analysis. Due to this, contaminant concentration in *MNM1* (the occupied working zone) was higher than in the case of the full approach. While this approach uses fewer resources, certain limitations that need to be considered are present.

6.2 FUTURE WORK

The study here presented showed an innovative technique to transfer flow field and pollutant from the global climate scale to the human body and mucosal epithelium cell scale by way of numerical modeling.

The final aim of this study was to predict occupational indoor contaminant concentration and inhalation exposure risk. Three approaches have been proposed and further future work has been planned for two of them, as described below.

i) NWP–CFD dynamic downscaling (steady-state)

Although steady-state results calculated at four different times of the day have been presented (06:00, 09:00, 13:00 and 17:00 hours), the final aim of the dynamic downscaling method is a transient approach. In this situation, steady-state calculated results will be set as boundary conditions for a transient MNM analysis through absolute wind pressure (Pa) at the air flow paths of the building instead of using C_p profiles to increase accuracy (using a .WPC file instead of .WTH). As this type of method needs more than four data points – considered too rough to set as boundary conditions – further dynamic downscaling, steady-state analyses need to be conducted. Although no time spacing has been decided, a gap of 3 hours is considered acceptable and an hourly steady-state analysis is not necessarily needed.

iii) Hybrid CFD–NWP–MNM transient approach

At this time, zonal contaminant concentration at the working zone (*MNM1*) has been calculated. Further steps include inhalation risk calculation based on *MNM1* transient results. However, it has been considered prudent to further correct ACH results and, therefore, zonal concentration, before this step is taken.

SUPPLEMENTAL INFORMATION

******** Pressure Macro for Window 1 (Figure 5-8) (w3_7) ********

```
#include "udf.h"        /***     UDF Header File     ***/
DEFINE_PROFILE(w3_7_pre, thread, position)
{
 face_t f;
 real t = CURRENT_TIME;

begin_f_loop(f, thread)
{
 if(t<=0)
{F_PROFILE(f, thread, position) = -220.608564720448;}
else if(t<=3600)
{F_PROFILE(f, thread, position) = -220.608564720448*(3600-t)/3600+(-114.399005299567*(t-0)/3600);}
else if(t<=7200)
{F_PROFILE(f, thread, position) = -114.399005299567*(7200-t)/3600+(-60.151217728*(t-3600)/3600);}
else if(t<=10800)
{F_PROFILE(f, thread, position) = -60.151217728*(10800-t)/3600+(-31.609287878072*(t-7200)/3600);}
else if(t<=14400)
{F_PROFILE(f, thread, position) = -31.609287878072*(14400-t)/3600+(-2.923707573228*(t-10800)/3600);}
else if(t<=18000)
{F_PROFILE(f, thread, position) = -2.923707573228*(18000-t)/3600+(-31.4972559968*(t-14400)/3600);}
else if(t<=21600)
{F_PROFILE(f, thread, position) = -31.4972559968*(21600-t)/3600+(-256.032821599689*(t-18000)/3600);}
else if(t<=25200)
{F_PROFILE(f, thread, position) = -256.032821599689*(25200-t)/3600+(-406.720171693968*(t-21600)/3600);}
else if(t<=28800)
{F_PROFILE(f, thread, position) = -406.720171693968*(28800-t)/3600+(-578.169663473955*(t-25200)/3600);}
else if(t<=32400)
{F_PROFILE(f, thread, position) = -578.169663473955*(32400-t)/3600+(-484.393114185728*(t-28800)/3600);}
}
end_f_loop(f, thread)
}
```

******** Temperature Macro for Window 1 (Figure 5-8) (w3_7) ********

```
DEFINE_PROFILE(w3_7_temp, thread, position)
{
face_t f;
real t = CURRENT_TIME;

begin_f_loop(f, thread)
{
if(t<=0)
{F_PROFILE(f, thread, position) = 290.626391066667;}
else if(t<=3600)
{F_PROFILE(f, thread, position) = 290.626391066667*(3600-t)/3600+(291.891232133333*(t-
0)/3600);}
else if(t<=7200)
{F_PROFILE(f, thread, position) = 291.891232133333*(7200-t)/3600+(292.899941822222*(t-
3600)/3600);}
else if(t<=10800)
{F_PROFILE(f, thread, position) = 292.899941822222*(10800-t)/3600+(294.18425*(t-7200)/3600);}
else if(t<=14400)
{F_PROFILE(f, thread, position) = 294.18425*(14400-t)/3600+(295.631511866667*(t-
10800)/3600);}
else if(t<=18000)
{F_PROFILE(f, thread, position) = 295.631511866667*(18000-t)/3600+(296.334827644444*(t-
14400)/3600);}
else if(t<=21600)
{F_PROFILE(f, thread, position) = 296.334827644444*(21600-t)/3600+(294.973427333333*(t-
18000)/3600);}
else if(t<=25200)
{F_PROFILE(f, thread, position) = 294.973427333333*(25200-t)/3600+(294.784114666667*(t-
21600)/3600);}
else if(t<=28800)
{F_PROFILE(f, thread, position) = 294.784114666667*(28800-t)/3600+(294.360414888889*(t-
25200)/3600);}
else if(t<=32400)
{F_PROFILE(f, thread, position) = 294.360414888889*(32400-t)/3600+(294.279280888889*(t-
28800)/3600);}
}
end_f_loop(f, thread)
}
```

******** TKE Macro for Window 1 (Figure 5-8) (w3_7) ********

```
DEFINE_PROFILE(w3_7_tke, thread, position)
{
 face_t f;
 real t = CURRENT_TIME;

begin_f_loop(f, thread)
{
if(t<=0)
{F_PROFILE(f, thread, position) = 0.521914027936576;}
else if(t<=3600)
{F_PROFILE(f, thread, position) = 0.521914027936576*(3600-t)/3600+(0.207135605891217*(t-
0)/3600);}
else if(t<=7200)
{F_PROFILE(f, thread, position) = 0.207135605891217*(7200-t)/3600+(0.065642408959232*(t-
3600)/3600);}else if(t<=10800)
   {F_PROFILE(f, thread, position) = 0.065642408959232*(10800-t)/3600+(0.0262018307431871*(t-
7200)/3600);}
else if(t<=14400)
{F_PROFILE(f, thread, position) = 0.0262018307431871*(14400-t)/3600+(0.00210152059728*(t-
10800)/3600);}
else if(t<=18000)
{F_PROFILE(f, thread, position) = 0.00210152059728*(18000-t)/3600+(0.033724585543*(t-
14400)/3600);}
else if(t<=21600)
{F_PROFILE(f, thread, position) = 0.033724585543*(21600-t)/3600+(0.321953372673487*(t-
18000)/3600);}
else if(t<=25200)
{F_PROFILE(f, thread, position) = 0.321953372673487*(25200-t)/3600+(0.46929468551916*(t-
21600)/3600);}
else if(t<=28800)
{F_PROFILE(f, thread, position) = 0.46929468551916*(28800-t)/3600+(0.544136485732444*(t-
25200)/3600);}
else if(t<=32400)
{F_PROFILE(f, thread, position) = 0.544136485732444*(32400-t)/3600+(0.43747939941376*(t-
28800)/3600);}
}
end_f_loop(f, thread)
}
```

******** ω Macro for Window 1 (Figure 5-8) (w3_7) ********

```
DEFINE_PROFILE(w3_7_omg, thread, position)
{
face_t f;
real t = CURRENT_TIME;

begin_f_loop(f, thread)
{
if(t<=0)
{F_PROFILE(f, thread, position) = 0.511392939767251;}
else if(t<=3600)
{F_PROFILE(f, thread, position) = 0.511392939767251*(3600-t)/3600+(0.941973552357013*(t-
0)/3600);}
else if(t<=7200)
{F_PROFILE(f, thread, position) = 0.941973552357013*(7200-t)/3600+(1.30811602568717*(t-
3600)/3600);}
else if(t<=10800)
{F_PROFILE(f, thread, position) = 1.30811602568717*(10800-t)/3600+(2.62863009765915*(t-
7200)/3600);}
else if(t<=14400)
{F_PROFILE(f, thread, position) = 2.62863009765915*(14400-t)/3600+(83.235786487747*(t-
10800)/3600);}
else if(t<=18000)
{F_PROFILE(f, thread, position) = 83.235786487747*(18000-t)/3600+(1.00124926394029*(t-
14400)/3600);}
else if(t<=21600)
{F_PROFILE(f, thread, position) = 1.00124926394029*(21600-t)/3600+(0.0885479024021092*(t-
18000)/3600);}
else if(t<=25200)
{F_PROFILE(f, thread, position) = 0.0885479024021092*(25200-t)/3600+(0.0444872565192416*(t-
21600)/3600);}
else if(t<=28800)
{F_PROFILE(f, thread, position) = 0.0444872565192416*(28800-t)/3600+(0.0263645885144031*(t-
25200)/3600);}
else if(t<=32400)
{F_PROFILE(f, thread, position) = 0.0263645885144031*(32400-t)/3600+(0.0343606786473648*(t-
28800)/3600);}
}
end_f_loop(f, thread)
}
```

******** Contaminant Macro for Kinzel 1 ********

```
DEFINE_PROFILE(kinzel1c1, t, i)
{
real x[ND_ND];
face_t f;

real c_wall;
real time;

begin_f_loop(f, t)
{
time = CURRENT_TIME;                    /* load current time[s] in calculation    */
if (time>=14400 && time<=18000)         /* if current time is in 12:00 - 13:00  */
{
c_wall = 0;
}
else
{
c_wall = 0.001473;
}
F_CENTROID(x, f, t);
F_PROFILE(f, t, i)= c_wall;         /***     input c_wall (value type concentration or flux)   ***/
}
end_f_loop(f, t)
}
```

******** Solar Intensity (for transient S2S) Macro ********

```
DEFINE_SOLAR_INTENSITY(sol_direct_intensity, sun_x, sun_y, sun_z, hour, minute)
{
	real intensity;
	intensity = 1423;
	printf("solar-time=%f intensity=%e\n", minute, intensity);
	return intensity;
}

DEFINE_SOLAR_INTENSITY(sol_diffuse_intensity, sun_x, sun_y, sun_z, hour, minute)
{
	real intensity;
	intensity = 200;
	printf("solar-time=%f intensity-diff=%e\n", minute, intensity);
	return intensity;
}
```